Computational Modeling of Blast-Induced Traumatic Brain Injury

by

Michelle K. Nyein

S.B., Chemistry, Massachusetts Institute of Technology (2004)
J.D., Harvard University (2007)

Submitted to the Department of Aeronautics and Astronautics
in partial fulfillment of the requirements for the degree of

Master of Science

at the

MASSACHUSETTS INSTITUTE OF TECHNOLOGY

June 2010

Author .....
Department of Aeronautics and Astronautics
May 21, 2010

Certified by .....
Raúl A. Radovitzky
Associate Professor of Aeronautics and Astronautics
Thesis Supervisor

Accepted by .....
Eytan H. Modiano
Associate Professor of Aeronautics and Astronautics
Chair, Committee on Graduate Students

Computational Modeling of Blast-Induced Traumatic Brain Injury

by

Michelle K. Nyein

Submitted to the Department of Aeronautics and Astronautics
on May 21, 2010, in partial fulfillment of the
requirements for the degree of
Master of Science

Abstract

Blast-induced TBI has gained prominence in recent years due to the conflicts in Iraq and Afghanistan, yet little is known about the mechanical effects of blasts on the human head; no injury thresholds have been established for blast effects on the head, and even direct transmission of the shock wave to the intracranial cavity is disputed. Still less is known about how personal protective equipment such as the Advanced Combat Helmet (ACH) affect the brain's response to blasts. The goal of this thesis is to investigate the mechanical response of the human brain to blasts and to study the effect of the ACH on the blast response of the head. To that end, a biofidelic computational model of the human head consisting of 11 distinct structures was developed from high-resolution medical imaging data. The model, known as the DVBIC/MIT Full Head Model (FHM), was subjected to blasts with incident overpressures of 6 atm and 30 atm and to a 5 m/s lateral impact. Results from the simulations demonstrate that blasts can penetrate the intracranial cavity and generate intracranial pressures that exceed the pressures produced during impact; the results suggest that blasts can plausibly directly cause traumatic brain injury. Subsequent investigation of the effect of the ACH on the blast response of the head found that the ACH provided minimal mitigation of blast effects. Results from the simulations conducted with the FHM extended to include the ACH suggest that the ACH can slightly reduce peak pressure magnitudes and delay peak pressure arrival times, but the benefits are minimal because the ACH does not protect the main pathways of load transmission from the blast to brain tissue. A more effective blast mitigation strategy might involve altering the helmet design to more completely surround the head in order to protect it from direct exposure to blast waves.

Thesis Supervisor: Raúl A. Radovitzky
Title: Associate Professor of Aeronautics and Astronautics

Acknowledgments

I would like to thank my advisor, Prof. Radovitzky, for providing invaluable guidance and support throughout the years and for continually encouraging me to grow as a graduate student.

I am thankful for the financial support of the Joint Improvised Explosive Device Defeat Organization (JIEDDO) through the Army Research Office.

I would also like to thank Dr. David Moore for providing the geometry for the DVBIC/MIT Full Head Model, supplying material properties for the head structures, and generally serving as a font of medical knowledge.

I would like to express my deep appreciation for the members, past and present, of the RR Group. Dr. Antoine Jerusalem, in particular, patiently answered questions and provided much needed guidance when I first started working on this project. Other postdoctoral researchers in the group, including Dr. Ludovic Noels, Dr. Tan Bui, Dr. Claudio Pita, and Dr. Julian Rimoli, have been more than generous with their time, knowledge, and advice. And I am truly grateful to the other students in the RR Group, including Michael Tupek, Lei Qiao, Andrew Seagraves, Srikanti Rupa Avasarala, Brandon Talamini, Li Yu, Amanda Jason, Piotr Fidkowski, Riley Schutt, and Ganesh Gurumurthy, for their friendship, support, and encouragement.

Last, but certainly not least, I would like to extend my deepest, most heartfelt gratitude to David Carpenter, who has been by my side through every step of my journey through grad school. During even the most difficult times, he provided unwavering love and support; I could not have done this without him.

Contents

List of Figures

List of Tables

Chapter 1

Introduction

Traumatic brain injury (TBI) has been a major public health concern in the United States for decades; from 1995 to 2001, an average of 1.4 million Americans a year sustained a TBI, leading to 50,000 deaths, 235,000 hospitalizations, and 1.1 million emergency department visits [45]. Of these, an estimated 80-90,000 experienced the onset of long-term disability [45, 88]. These TBIs were largely caused by falls, motor vehicle crashes, sports collisions, and firearm assaults [45]. Even with an average of 1.4 million Americans sustaining a TBI each year, though, the average annual incidence of TBI was only 0.5% [45]. Since Operation Enduring Freedom (OEF) began in Afghanistan in October 2001 and Operation Iraqi Freedom (OIF) began in Iraq in May 2003, the incidence of TBI among U.S. service members has been significantly higher. Indeed, TBI has been labeled as the signature injury of OEF and OIF [34].

The U.S. Department of Defense has estimated that 10-20% of OEF/OIF Army and Marine Corps service members have sustained a mild TBI, based on data from 2004 to 2006 at selected military installations [65]. Other studies have found that anywhere from 12 to 22.8% of OEF/OIF veterans have experienced TBIs. For example, a recent study found that 22.8% of soldiers in an Army Brigade Combat Team returning from Iraq had clinician-confirmed TBI [86]. A 2008 RAND survey of OEF/OIF veterans found that 19.5% had experienced a probable TBI during deployment; given that prevalence of TBI, it was estimated that approximately 320,000 OEF/OIF veterans could have experienced a TBI [84]. A 2006 study of U.S. Army infantry soldiers

3-4 months after their return from a year-long deployment to Iraq found that 15% reported an injury during deployment that involved loss of consciousness or altered mental status [34], and a 2005 survey of OEF/OIF veterans who had left combat theaters by September 2004 found that about 12% of the 2,235 respondents reported a history consistent with mild TBI [77]. Among those who have been medically evacuated from theater, the proportion who have suffered a TBI is predictably higher; screening at Walter Reed Army Medical Center (WRAMC), for example, found that 30% of service members medically evacuated there from the OEF/OIF combat theaters from January 2003 to June 2007 had sustained a TBI [65]. And of 50 OEF/OIF veterans treated at the Tampa Veterans Affairs Polytrauma Rehabilitation Center, 80% had incurred combat-related TBI, with 70% of the injuries caused by improvised explosive devices (IEDs) [14]. Given the high prevalence of TBI among U.S. service members, the costs of military-related TBI are enormous. The 2008 RAND study conservatively estimated the total cost for deployment-related TBI from 2001 to 2007 to be $554-854 million [84]. It was noted that the estimate likely understates the costs of deployment-related TBI, because while it includes the cost of treatment and reduction in productivity in the first year following injury and costs associated with mortality and suicide, it does not include cost of treatment or reduction in productivity beyond the first year, caregiver burden, TBI-related health problems, or downstream costs stemming from substance abuse, domestic violence, homelessness, and other factors [84]. While the precise cost of military-related TBI over the last decade remains unclear, it is apparent that a significant fraction of U.S. service members have sustained a TBI during OEF/OIF, and the costs associated with those deployment-related TBIs have been massive.

For active duty military personnel in war zones, blasts are the primary cause of TBI [84]. 68% of the OEF/OIF soldiers at WRAMC who screened positive for TBI had been injured by a blast [95], and data collected from March to September 2004 from Navy-Marine Corps medical facilities in Iraq found that IEDs were responsible for 62% of combat-related TBIs, even though 69% of the TBI patients had worn a helmet [27]. One reason blasts have become such a large cause of military-related TBI

is because the current conflicts in Iraq and Afghanistan involve battling insurgents who favor cheap, easily concealed explosive weapons capable of killing large numbers of people. As a result, approximately 60% of total combat casualties [49] and 67% of Army war zone evacuations [94] have been attributed to explosive blasts. The IED in particular has become the most common explosive weapon [49], accounting for about 40% of all casualties [84]. IEDs can be manufactured from materials ranging from 155 mm artillery shells to plastic explosives to barrels of gasoline [3]; they have evolved from relatively crude devices detonated by simple mechanisms to sophisticated devices capable of penetrating the armor of an M-1 Abrams tank [84]. Exposure to these blasts often leads to head and neck injuries. For example, 97% of the injuries in one Marine unit in Iraq were due to explosions (65% to IEDs), with 53% involving the head and neck [82], and a study of 4,831 patients at a U.S. Army echelon II medical facility in Iraq between October 1, 2003, and June 30, 2004, found that 88% of U.S military personnel treated had been injured by IEDs or mortars, with up to 47% of those injuries involving the head [60]. According to the Joint Theater Trauma Registry compiled by the U.S. Army Institute of Surgical Research, 22% of wounded OEF/OIF service members who passed through Landstuhl Regional Medical Center in Germany had injuries to the head, face, or neck [67]. It is likely that a significant number of these head injuries caused by explosions included blast-related TBIs (bTBIs).

Blast-related TBI has also gained visibility due to advances in military medicine and personal protective equipment (PPE) that allow U.S. service members to survive blasts that previously would have been fatal. In the current conflicts, the survival rates are dramatically higher than in previous conflicts. While 30% of wounded U.S. soldiers died in World War II and 24% of wounded U.S. soldiers died in the Vietnam conflict, only about 10% of wounded U.S. soldiers have died in Afghanistan and Iraq [28]. The high survival rate can be attributed in part to significant advances in military medicine, including deployment of leaner, more mobile surgical teams far forward on the battlefield and rapid medical evacuation from combat zones — the average time from battlefield to arrival in the United States is now less than 4 days, compared to 45 days during the Vietnam conflict [28]. In addition, important ad-

vances in TBI treatment have been made, including early decompressive craniectomy, neurocritical care, cerebral angiography, transcranial Doppler, hypertonic saline, and TBI clinical management guidelines [49]. The high survival rate can also be attributed in part to advances in PPE, with improvements in body armor allowing soldiers to survive injuries that previously would have been fatal [67]. However, the improved protective gear do not necessarily prevent blast-related TBI; PPE have historically been designed to protect against ballistic impact, not blasts. Until recently, blast protection has not been a primary objective in the design of PPE, and any secondary blast protection provided has been fortuitous; the low incidence of blast lung nowadays, for example, suggests that Kevlar vests are effective in preventing those types of injuries. The influence of other PPE, such as the Advanced Combat Helmet (ACH), on the brain's response to blast waves remains largely unknown.

TBI, and blast-related TBI in particular, has thus emerged as the leading injury among OEF/OIF service members [65]. Despite the importance of understanding blast-related TBI, however, little is known about the mechanical effect of blasts on the human head; no injury thresholds have been established for blast effects on the head, and even direct transmission of the shock wave to the intracranial cavity is disputed. Alternative mechanisms have been proposed, including acceleration of the head and transmission of the blast wave to the brain through a thoracic mechanism [17, 12]. Some have questioned the link between mild TBI and adverse physical health outcomes at all [34]. Additionally, it is not understood how the ACH affects the brain's response to blasts.

This thesis aims to investigate the mechanical response of the human brain to blast waves and to examine the effect of the ACH on that response through numerical simulation. The remainder of Chapter 1 will provide background on blast-related TBI, and Chapter 2 will discuss existing computational TBI models. Chapter 3 will present the modeling framework used in the blast-related TBI simulations; the computational code, full head model, material models, and material properties will be detailed. In Chapter 4, the results from the simulations will be presented and discussed, and it will be demonstrated that a blast wave can propagate through the cranial cavity

and result in stresses that match or exceed those observed in impact-related TBI. In Chapter 5, the results from simulations conducted with the full head model extended to include the ACH will be presented; it will be shown that the addition of the ACH minimally delays and reduces the magnitudes of stresses transmitted to the head by the blast wave. Chapter 6 will contain conclusions and comments on future work.

1.1 Blast-Induced TBI

1.1.1 Blast Injury Mechanisms

When an explosive device detonates, a chemical reaction occurs that rapidly releases gas and heat. The gas radially expands as a supersonic, high-pressure blast wave, and the leading edge of the blast wave compresses the host medium to create a shock front. For an ideal free-field explosion in air, the blast wave can be modeled as a Friedlander waveform, which is characterized by a rapid rise to peak pressure immediately followed by an exponential decay of the overpressure and a relatively prolonged underpressure [6]. If the blast wave encounters a solid object, such as a wall or other structure, it is significantly modified as it reflects from the object and diffracts around it; assuming that air behaves as an ideal gas, the overpressure of the reflected wave can be up to 8 times greater than the overpressure of the incident wave, and taking real gas effects into account, the reflected overpressure can be even larger, perhaps 20 or more times greater than the incident overpressure [6]. The three-dimensional fluid flow field characterizing an explosion can thus be very complex, and there is considerable room for variability in military-associated blast exposure.

Blasts can result in four types of injury: 1) primary blast injury, which results from the impact of the blast wave with body tissue; 2) secondary blast injury, which results from debris and shrapnel; 3) tertiary injury, which results from individuals being thrown by blast wind and impacting stationary objects; and 4) quaternary blast injury, which encompasses all other explosion-related injuries, including burns, inhalation injuries, crush injuries, and asthma [11]. While secondary, tertiary, and

quaternary blast injuries are not unique to blasts and have been studied extensively for decades, primary blast injury is not as well understood, particularly as it relates to TBI. The organs most susceptible to primary blast injury are the air-filled organs such as the ears, lungs, and gastrointestinal (GI) tract [25], with the most common injury being rupture of the tympanic membranes [63]. Although research efforts in prior decades focused on blast lung injuries, such injuries have occurred only infrequently during OEF/OIF thanks to advances in body armor, and blast-related GI tract injuries have been even rarer [49]. Now, with soldiers surviving higher intensity blasts that previously would have been fatal due to lung or GI tract injury, focus has shifted to blast-related brain injury. The brain, residing in a fluid-filled cavity, is vulnerable to blasts [25], but little is known about how blasts affect the brain; no injury thresholds have been established, and direct transmission of the non-linear shock wave into the intracranial cavity has been disputed. Here, focusing solely on primary blast injury, we investigate the effects of blast waves on the human brain.

There is little question that exposure to blasts can harm the brain, as numerous animal studies have linked blasts to various manifestations of brain damage. One study of rats, for example, found that application of 12.5 MPa shock waves resulted in cerebral contusional hemorrhage associated with neuronal apoptosis, while application of 1.0 MPa shock waves resulted in mild morphological changes in neurons [39]. Another study found that rats subjected to 147 kPa air blasts suffered from prominent areas of cortical loss, gliosis, and infiltration, as well as hemorrhage and extensive necrosis [50], and a different study found that subjecting rats to 20 kPa blasts resulted in cortical neuron degeneration and significant impairment of performance on tests of coordination, strength, and startle response [57]. A study of pigs found that exposure to free air explosions with peak overpressure of 237 kPa resulted in transient flattening of the electroencephalogram (EEG) and short-lasting apnea, indicating a blast wave-induced effect on the brainstem or higher controlling center [80]. From these studies, it is evident that blasts can have a detrimental effect on the brain.

The mechanism by which blasts result in brain damage, however, remains in dis-

pute. One proposed mechanism suggests that shock waves could directly propagate through the cranial cavity as stress waves, which travel around the speed of sound with high amplitude and can injure tissue through spalling, implosion, and pressure differentials [47]. A 1961 study exposing rhesus monkeys to air blasts found a large fraction of the pressure was transmitted into the brain through the skull, while little was transmitted from the torso to the brain [47]. Studies of rats and rabbits exposed to blasts also demonstrated that pressure waves could be transmitted directly to the brain with only slight change in amplitude [47]. Alternatively, it has been suggested that the central nervous system (CNS) could be injured by blasts through the cerebral vasculature via a thoracic mechanism [17]. Studies have shown that ballistic pressure waves, which are generated when a projectile enters a viscous medium, can cause remote injuries; for example, studies have found that shooting pigs in the thigh can result in apnea, EEG suppression, microscopic neuronal damage, and elevated pressures within the brain [17]. Similarly, studies have shown that behind armor trauma, which results when impacts to body armor transmit sufficient force to tissue behind the armor, can result in EEG suppression and death [17]. These studies demonstrate that localized trauma can lead to remote injuries, and they provide some support for the hypothesis that blast waves can be transmitted from the torso to the brain through the vasculature. Finally, it has been suggested that acceleration of the head can lead to coup-contrecoup injury akin to that observed in impact-related TBI [21]. Peak intracranial pressures due to acceleration have been found to be in the same range as pressure magnitudes that result in mTBI in lateral fluid percussion (LFP) models [17]. Still, it remains unknown which mechanism, or combination of mechanisms, accounts for blast-related TBI. To develop a more complete understanding of TBI, we now examine its medical and biological aspects, considering its clinical definition, symptoms, and pathophysiology.

1.1.2 Definition

In 1995, the Centers for Disease Control and Prevention (CDC) published Guidelines for Surveillance of Central Nervous System Injury, which defined TBI in terms of ICD-

9-CM (International Classification of Diseases, Ninth Revision, Clinical Modification) diagnostic codes [89]. To summarize, TBI was defined as an occurrence of head injury that is associated with decreased level of consciousness, amnesia, other neurological or neuropsychological abnormalities, skull fracture, diagnosed intracranial lesions, or death [88]. TBIs may be classified by severity as mild, moderate, or severe. The American Congress of Rehabilitation Medicine has defined mild TBI (mTBI) as a head injury resulting in at least one of the following: (1) loss of consciousness (LOC) for approximately 30 minutes or less; (2) post-traumatic amnesia (PTA) for less than 24 hours; (3) any alteration in mental state at the time of the accident; and (4) focal neurological deficit(s) that may or may not be transient, with a Glasgow Coma Scale (GCS) score of 13 or greater 30 minutes after injury [53, 62]. Moderate TBI is typically associated with a presenting GCS score of 9-13, and severe TBI with a GCS score of 8 or lower [49]. A new classification specific to blast-related TBI has been proposed, in which a mild bTBI would be characterized by LOC for less than 1 hour and PTA for less than 24 hours following exposure to an explosive blast, a moderate bTBI would be characterized by LOC for 1-24 hours and PTA for 1-7 days, and severe bTBI would be characterized by LOC for more than 24 hours and PTA for more than 7 days [49].

The vast majority of TBIs in the civilian population are mild; the CDC has reported that up to 75% of TBIs that occur each year are mild [11], and a World Health Organization task force reported that 70-90% of all treated TBI were mild [44]. Mild TBI is typically not associated with abnormalities in brain imaging [67], and most patients with mild TBI recover fully in 4-12 weeks [40, 2]. However, mTBI patients with more severe injuries, such as those who experienced LOC lasting more than 10 minutes or PTA lasting more than 4-6 hours, may require months to years to recuperate [2]. In addition, some mTBI patients develop postconcussive syndrome (PCS), experiencing persistent cognitive, behavioral, and/or somatic symptoms [77, 2, 32]. Studies have shown that 15-35% of patients with mild TBI experience this onset of long-term disability [2, 32, 88]. It is not known why some patients develop PCS, although some explanations have included high level of preexisting emotional

stress, severe pain, and genetic predisposition to poor TBI outcome [2, 40]. Repeated exposure to blasts has also been found to lead to PCS and generally worsen TBI symptoms [1, 82]. One study of 126 veterans with a history of mild blast-related TBI found that of the 63% of veterans who had residual impairments on neurological or neuropsychological examinations, 91% had reported multiple episodes of loss of consciousness [75].

In the military context, a significant proportion of TBIs sustained in combat are moderate or severe. One study of patients at Navy-Marine Corps medical facilities in Iraq found that 54% of TBI patients who had been wounded in action were medically evacuated [27]. Many TBI patients who are medically evacuated from combat zones have moderate or severe TBIs; 56% of TBI patients seen at Walter Reed Army Medical Center from January 2003 to February 2005, for example, suffered a moderate or severe TBI [94]. Combat-injured patients with moderate bTBI generally require prompt medical evacuation, while combat-injured patients with severe TBI generally require advanced medical care on the battlefield, then evacuation to the nearest combat hospital with neurosurgical capability [49]. Fortunately, a number of neurosurgical techniques have been developed to mitigate the effects of severe TBI, such as intravenous infusions of hypertonic saline, mild hypothermia, and early decompressive craniectomy [49]. Nevertheless, 30-50% of severe TBI patients die, with 90% of the deaths occurring within 48 hours of injury [69]. The deaths are typically caused by uncontrolled raised intracranial pressure, which results in brainstem herniation [69].

1.1.3 Symptoms

Common symptoms of TBI include a variety of cognitive, behavioral, and physical/somatic changes. Cognitive changes may include disturbances in attention, memory, language, or executive functioning, such as poor planning, organizing, or sequencing, and/or impaired judgment and impulse control [67, 44, 72]. Behavioral changes may include mood changes, depression, anxiety, impulsiveness, emotional outbursts, irritability, or inappropriate laughter [67, 40]. Physical or somatic symptoms may include headaches, fatigue, sleep disturbances, dizziness, problems with motor skills,

and sensitivity to light and noise [67, 40]. In addition, following TBI, some patients experience neuropsychiatric problems such as major depression, anxiety disorders, and psychosis [72], and up to 50% of patients with TBI suffer from impaired neuroendocrine function, particularly growth hormone deficiency [40]. TBI may also cause patients to be more sensitive to many medications [40]. For blast-injured patients in particular, common symptoms include subdural hematoma, headache, blurring of vision, transient deafness, and psychoneuroses [47]. Blast-related TBI patients are also more likely than other TBI patients to report neurological disorders such as insomnia, impaired concentration, memory loss, and hypervigilance [47, 94].

Many mild TBI symptoms overlap with post-traumatic stress disorder (PTSD) symptoms, and a number of patients suffer from both disorders [67]. Overlapping symptoms include cognitive problems such as impaired learning, forgetfulness, attention and concentration difficulties, slower processing speed, and a sense of being overwhelmed with once simple tasks, and changes in personality such as impulsiveness, reduced insight, rigid thinking, and reduced motivation [40]. Studies have shown that PTSD is strongly associated with mild TBI; one survey of soldiers from two U.S. Army combat infantry brigades 3-4 months after returning from a yearlong deployment in Iraq found that 32.6% of soldiers with mild TBI met the criteria for PTSD [34], and another survey of OIF/OEF veterans from all branches of the military found that 39.6% of respondents with mild TBI had PTSD [77]. It has been suggested that the strong association between mild TBI and PTSD can be explained by the fact that the life-threatening, traumatic events that lead to combat-related mTBI are also likely to result in PTSD, or by the possibility that symptoms associated with PTSD may be a manifestation of brain injury [34, 77]. In addition, it has been suggested that PTSD can modify the effects of mTBI [34, 77], and in particular, exacerbate cognitive symptoms of mTBI [40]. Studies have also found that PTSD is strongly associated with persistent postconcussive symptoms following mTBI. In the Hoge et al. study, it was found that while soldiers with mild TBI were significantly more likely to report poor general health, missed workdays, medical visits, and a high number of somatic and postconcussive symptoms, after adjustment for PTSD and depression,

the association between mTBI and poor physical health outcomes disappeared, except for headache; the poor physical health outcomes occurred almost exclusively in soldiers with PTSD, and among those soldiers with PTSD, the proportion with poor physical health symptoms did not significantly differ according to type of injury [34]. In the Schneiderman et al. study, it was found that 35% of respondents with mild TBI reported persistent postconcussive symptoms, but 66% of respondents with both mild TBI and PTSD reported persistent postconcussive symptoms [77]. The association between mTBI, PTSD, and physical health problems remains under investigation, but one thing is clear — soldiers who reported mTBI events were at very high risk for physical and mental health problems [34, 77].

Many of the symptoms of TBI can be treated by pharmaceuticals. For example, stimulants such as methylphenidate or dextroamphetamine are commonly used to treat problems with attention or information processing, selective serotonin-reuptake inhibitor antidepressants are sometimes prescribed for irritability or angry outbursts, and valproate is often prescribed for migraines and behavioral symptoms [67]. However, there is still no broad-based cure for TBI, in large part due to the heterogeneous nature of TBI. While a number of pharmacological agents, including calcium channel blockers, corticosteroids, magnesium, N-methyl-D-aspartate (NMDA) receptor antagonists, and progesterone, have shown promise in preclinical studies, and some have even had encouraging results in phase II clinical trials, none have demonstrated efficacy in phase III clinical trials thus far [101, 7]. Similarly, no single biomarker of TBI has yet been identified, although it has been suggested that a combination of markers, such as S-100β, neuron specific enolase, glial fibrillary acid protein, myelin basic protein, αII-spectrin breakdown products, NMDA-R fragments, and anti-inflammatory cytokines could effectively detect TBI and predict outcomes [81].

1.1.4 Pathophysiology

TBI comprises two phases of injury: primary and secondary. Primary injury encompasses direct, unavoidable injury that occurs during the initial insult, including contusions, lacerations, hemorrhages, and axonal shearing. Secondary injury follows

from the primary injury and occurs through biochemical processes in the hours and days following the initial insult.

Primary Injury

A mechanical insult to the head may cause blood vessels to rupture, leading to contusions, hemorrhages, and hematomas. Cerebral contusions, or bruises, are caused when capillaries bleed into the brain tissue. They are commonly located within the gray matter or at the gray-white matter interface, particularly in the frontal and temporal lobes due to their proximity to bony protuberances on the inside surface of the skull [44, 82, 70, 40]. The contusions can directly disrupt function in cortical and subcortical regions [44], contributing to local necrotic and apoptotic neuronal deaths [70]. Some studies have linked focal cortical contusions in the anterior frontal and temporal lobes to impairments in executive functioning, working memory, memory encoding and retrieval, higher order attenuation, and behavior modulation, and contusions in the posterior temporal lobe to language disorders [70]. Rupture of blood vessels can also lead to hemorrhages, such as subarachnoid hemorrhage, which involves bleeding in the space between the arachnoid membrane and the pia mater. Presence of subarachnoid hemorrhage typically indicates a more severe injury and often heralds acute severe cerebral edema and hyperemia, as well as delayed vasospasm [49]. In addition, contusions and hemorrhages can lead to hematomas, or collections of blood outside blood vessels. Subdural hematoma, for example, is caused by bleeding from the veins that run between the dura mater and the brain, and epidural hematoma is caused by bleeding between the dura mater and the skull. Hematomas can be dangerous because they can compress the brain and raise intracranial pressure, leading to cerebral ischemia, which contributes to about 90% of deaths after closed head injuries [91].

A mechanical insult to the head can also cause diffuse axonal injury (DAI), in which axons are damaged by shearing forces, leading to degeneration of some axons' distal projections and diffuse loss of synaptic terminals [69, 67]. Occurring in all severities of TBI, it has been increasingly recognized as central to a patient's outcome, causing at least one-third of the poor outcomes of TBI [69]. It can commonly be

found in the gray-white matter junction, internal capsule, deep gray matter, rostral brainstem, and corpus callosum [82, 64, 44]. Damage to these regions is associated with high mortality because the sites serve as neural relay stations and as centers for vital functions; for example, trauma to the brainstem occurs in 70% of head injuries with survival times of less than 48 hours [4]. Loss of neural connections may lead to many of the symptoms associated with brain injuries [67]. Deeper lesions correspond to more severe injuries and greater disability, and involvement of the corpus callosum or upper brainstem corresponds to more severe levels of DAI [70]. One study demonstrated that moderate and severe TBI subjects had reduced white matter integrity in 13 distinct regions, including the corpus callosum and corona radiata, and mild TBI subjects had reduced white matter integrity in 3 regions — the superior longitudinal fasciculus, sagittal stratum, and corticospinal tract [44].

Secondary Injury

Secondary injury mechanisms are the physiological responses to primary injury [49]. Following the initial insult, primary injuries can trigger secondary injury through a number of mechanisms, including excitotoxicity, oxidative stress, and inflammation.

Excitotoxicity, for example, can lead to neuronal and axonal death. Primary injury typically leads to excessive extracellular concentrations of the excitatory neurotransmitters (and excitotoxins) glutamate and aspartate [69, 91, 40]. Animal studies have demonstrated significant increases in extracellular glutamate and aspartate adjacent to the trauma site, with the increases being proportional to the severity of the injury [26]. The glutamate and aspartate act on NMDA receptors to alter cell wall permeability, allowing increases in intracellular calcium and sodium [91, 69]. The excess calcium and sodium activate cysteine proteases such as calpains and caspases that can degrade a variety of proteins, including cytoskeletal proteins, membrane receptors, and signal transduction enzymes [93]; this leads to necrotic and apoptotic cell death [69, 70]. In axons, for example, where mechanical forces associated with injury can also trigger focal alterations in axolemmal permeability that allow influx of calcium [70], the calpains and caspases degrade proteins responsible for shape and

transport, ultimately leading to axonal disconnection [69, 91]. In humans, this process can take several hours or days postinjury [70]. Following axonal damage and disconnection, the axon undergoes Wallerian degeneration, a several month process in which the portion of the axon separated from the neuron's nucleus disintegrates [70]. Some data suggest that this sets the stage for intact nerve fibers to sprout, leading to recovery of synaptic input [70], while other data suggest that glial scars may form in the spaces left by degenerating axons, obliterating pathways for axonal growth or actively inhibiting axonal growth. Preliminary studies have shown that the neuronal cell bodies linked to traumatically damaged axons do not progress to rapid cell death, but rather undergo perturbation of neuronal protein translation that persists for several days and is followed by cellular recovery [70].

Excitotoxicity can also lead to oxidative stress, a secondary injury mechanism that involves reactive oxygen species inducing oxidative damage [69, 21]. For example, excessive NMDA receptor activity can increase production of nitric oxide, while excess intracellular calcium can increase production of superoxide; the nitric oxide and superoxide react to produce peroxynitrite, a highly reactive oxidant that can produce nitration of amino acid aromatic rings, lipid peroxidation, and DNA fragmentation, all of which rapidly lead to cell death [69]. In general, reactive oxygen species can cause considerable damage to proteins, lipids, and DNA through peroxidation of cellular and vascular structures, DNA damage, protein oxidation, lipid/protein nitration, and inhibition of the mitochondrial electron transport chain, leading to initiation of necrotic and apoptotic cell death cascades [21, 96]. One rat study found levels of oxidative stress to be increased within a few hours of insult, with a return to normal levels by 5 days postinjury [21].

Additional secondary responses include neuroinflammation, reduced cerebral metabolic and energetic states, and cholinergic deficits. For example, primary brain injury can trigger cellular and humoral inflammatory responses that can last hours to days [91, 1]. Following primary injury, concentrations of pro-inflammatory cytokines such as interleukin-6 are increased [91, 1], and microglia, the resident immune cells of the central nervous system, are activated, releasing various chemokines and cytokines that

can act as pro-inflammatory factors [1]. These processes act to eliminate injured and adjacent tissue, replacing them with newly synthesized scar tissue [96]. In addition to inflammation, primary insults can lead to a reduction in cerebral metabolic and energetic states. TBI has been found to lead to a sharp reduction in intracellular free magnesium [26]. Since intracellular magnesium regulates many processes responsible for cellular metabolism and bioenergetics, cerebral metabolic and energetic states are frequently reduced after TBI, with degree of metabolic failure related to severity of the primary insult [96]. Some researchers have found a correlation between reduced cerebral metabolic rate in the brainstem, thalamus, and cerebellum and level of consciousness in patients recovering from TBI [70]. Primary insults can also lead to a decrease in acetylcholine, a neurotransmitter considered critical for arousal and attention, declarative memory, and executive function; cholinergic deficit is thought to be the neurochemical basis for cognitive deficits following TBI [40].

A number of secondary outcomes are particularly common sequelae of blast-related TBI. For example, blast-related TBI frequently results in vasogenic or cytotoxic cerebral edema [1]. Cerebral edema, or swelling of the brain due to water imbalance, is dangerous because it can rapidly develop and lead to intracranial hypertension, hypoxia, ischemia, and necrotic and apoptotic neuronal cell death [1, 50, 3]. Vasogenic edema, which is seen primarily in cerebral white matter, occurs rapidly as the inflammatory response breaks down the blood-brain barrier and allows for transfer of ions and proteins from the intravascular to the extracellular brain compartments [3, 1, 96]. In contrast, cytotoxic edema is seen primarily in gray matter and develops slowly as excitotoxins cause accumulation of intracellular calcium and sodium, leading to an osmotic gradient that draws in water [3, 1]. Military neurosurgeons have noted the common presence of diffuse cerebral edema among severe bTBI patients [49].

Another particularly common secondary outcome of blast-induced TBI is vasospasm, a condition in which blood vessels spasm, leading to vasoconstriction and possible ischemia and necrosis [96]. Vasospasm indicates severe damage to the brain, and it is worse with higher injury severity [96, 49]. Vasospasm can be caused by chronic depolarization of vascular smooth muscle due to reduced potassium channel

activity, release of endothelin along with reduced availability of nitric oxide, cyclic GMP depletion of vascular smooth muscle, potentiation of prostaglandin-induced vasoconstriction, or free radical formation; onset varies from the 2nd to 15th day post-injury, and hypoperfusion occurs in 50% of patients developing vasospasm [96, 49]. Often it is the cause of delayed neurological deterioration [49]. It has been reported that vasospasm occurs in more than 1/3 of patients with TBI [96], and one study found that 47% of blast-related TBI patients developed cerebral vasospasm [49]. Vasospasm is more prevalent when traumatic subarachnoid hemorrhage is also present acutely [49, 76].

Cerebral edema and vasospasm can both lead to cerebral ischemia, or restriction in blood supply, which is associated with poor neurological outcome — death or vegetative state [96]. Cerebral ischemia may occur through morphological injury as a result of mechanical displacement, hypotension in the presence of autoregulatory failure, inadequate availability of nitric oxide or cholinergic neurotransmitters, or vasoconstriction [96]. Ischemia can lead to brain tissue hypoxia, or deprivation of oxygen supply, which can cause infarction of neuronal tissue and thus poor outcome [96, 21, 91]. Additionally, hyperemia, or increase in blood flow, may follow post-traumatic ischemia, leading to increases in cerebral blood volume and intracranial pressure [96]. Severe bTBI patients have been known to develop delayed increased intracranial pressure 14-21 days after the initial insult [49]. Both ischemia and hyperemia refer to mismatch between cerebral blood flow and cerebral metabolism; following TBI, cerebral blood flow autoregulation is impaired in most patients [96]. It has been claimed that the presence of hypotension is the single most important predictor of mortality [21].

1.2 Summary

Blast-related TBI is a complex, heterogeneous, multiphasic injury, and in the military context, all levels of severity are well-represented. Although studies have demonstrated that exposure to blasts can lead to brain damage, the mechanism through

which that damage occurs is not yet known. What is known is that mechanical forces are imparted from the blast wave to the brain, leading to primary injuries such as contusions, hemorrhages, hematomas, and diffuse axonal injury. The primary injuries then trigger secondary injuries through a series of diverse biochemical and physiological mechanisms, including excitotoxicity, oxidative stress, and inflammation. The heterogeneity of the mechanisms leads to a wide range of cognitive, behavioral, and physical/somatic symptoms, and results in difficulty developing a broad-based bTBI cure. Although many of the symptoms can be treated by pharmacological agents, no cure yet exists for blast-related TBI.

Chapter 2

Existing TBI Models

For decades, researchers have studied impact-related TBI, seeking to understand trauma arising from automobile accidents and sports collisions; through animal and cadaver experiments and computational models of varying complexity, researchers have identified injury mechanisms and developed injury tolerance criteria. Much more recently, researchers have also begun investigating blast-related TBI. In the following sections, we describe examples of the previous work done on impact-related and blast-related TBI.

2.1 Impact-Related TBI

2.1.1 Cadaver Experiments

Over the years, a number of researchers have conducted impact-related TBI experiments. Two sets of experimental cadaver data in particular have been widely used to validate computational impact-related TBI models. The first set is from Nahum, who in 1977 conducted two series of frontal head impact experiments on cadavers [61]. In the experiments, seated, stationary cadavers were impacted by a rigid mass traveling at a constant velocity; the skull was rotated so that the anatomical plane was inclined 45 degrees to the horizontal, and the blow was delivered to the frontal bone in the mid-sagittal plane in an anteroposterior direction. The cadavers were repressurized

to *in vivo* pressure levels and were instrumented with pressure transducers at five locations: in the frontal region adjacent to the impact site, immediately posterior and superior to the coronal and squamosal sutures respectively in the parietal bone, inferior to the lambdoidal suture in the occipital bone, and at the posterior fossa in the occipital bone. The first series consisted of 8 single impact experiments in which impactors with masses ranging from 5.23 to 23.09 kg were launched with velocities ranging from 8.41 to 12.95 m/s. The experiments found high positive peak pressures at the impact site, or coup site, decreasing pressure magnitudes that eventually became negative as the contrecoup site, opposite the impact site, was approached, and high negative pressures at the contrecoup site. Data from experiment 37, which involved a 5.59 kg impactor traveling at 9.94 m/s with a peak input force of 7.9 kN, are often used for validation of finite element (FE) models, since intracranial pressure histories were published for that experiment only. In experiment 37, peak positive pressure was reported to be 141.2 kPa in the frontal region, and peak negative pressure was reported to be -60.3 kPa in the posterior fossa region; no discernible hemorrhage was reported. The second series of experiments focused on repeated impacts on a single specimen, varying the impact velocity and impact interface material. A linear relationship was found between pressure and head acceleration. These cadaver experiments conducted by Nahum demonstrated the coup-contrecoup intracranial pressure response to direct head impacts and provided useful data against which simulation data can be compared.

More recently, in 1992, Trosseille conducted a series of head impact experiments in which repressurized cadavers were hung in a sitting position with a harness and impacted in the anteroposterior direction [90]. In the tests, the impactor had a mass of 23.4 kg, the initial velocity ranged from 5 to 7 m/s, and the point of impact varied. The cadavers were instrumented to measure intracranial pressures in the frontal, parietal, and occipital lobes, and in certain tests, to measure ventricular pressures. Data from three of the tests indicated that the occipital region pulled away from the skull, while data from two of the tests indicated that the brain and skull remained well attached. Data from these cadaver tests have also been used for validation of

computational head models.

2.1.2 Finite Element Head Models

Given the difficulties associated with conducting TBI experiments on cadavers or live humans, many researchers have turned to increasingly sophisticated computational head models. The following are examples of finite element models that have been developed for use in simulations of impact-related TBI.

Wayne State University Brain Injury Model

One three-dimensional (3D) computational head model that has been developed is the Wayne State University Brain Injury Model (WSUBIM). One of the earliest versions of the WSUBIM had 1,110 elements and consisted of a 3-layer skull (outer table, diploe, inner table), CSF, and brain; all the materials were assumed to be homogeneous, isotropic, and linearly elastic [74]. The model was validated using data from Nahum's frontal impact experiments and was then used in simulations of side and rear impacts. Under all impact conditions, positive pressure was observed at the coup site and negative pressure was observed at the contrecoup site, with localized skull deformation at the impact site. In both the frontal and rear impact simulations, coup pressure was larger than contrecoup pressure, with coup pressure higher in the frontal simulation and contrecoup pressure higher in the rear simulation. In the side impact simulation, there was a more symmetric pressure response, with almost identical values for the coup and contrecoup pressure. It was also found that variations in the Young's modulus of the skull and bulk modulus of the brain and CSF affected intracranial pressure response.

A number of other versions of the WSUBIM were subsequently developed. Comparison of frontal and lateral impacts using one 22,995-element version found that lateral impacts result in larger skull deformation, higher intracranial pressure, and larger shear deformation than frontal impacts [104]. A 41,354-element version, which differentiated gray matter from white matter, was used to predict the location of DAI

in the brain and to predict the directional sensitivity of the brain to impacts from varying directions; that version was later revised and upgraded to include a sliding interface between the skull and brain surface [103].

In 2001, an entirely new version of the WSUBIM was developed in order to better model direct and indirect impacts over a wide range of impact severities [103]. The geometry of the head was taken from a previous model, and boundaries between anatomical structures were refined and improved based on published anatomical drawings. The revised model, consisting of over 314,500 elements with an average characteristic length of around 2 mm, simulated all essential anatomical features of a 50th percentile male head, including the scalp, 3-layer skull, dura, falx and tentorium, pia, sagittal and transverse sinuses, CSF, white and gray matter, cerebellum, brainstem, lateral ventricles, third ventricles, and bridging veins. The model also included an anatomically detailed facial model based on Magnetic Resonance Imaging (MRI) and Computed Tomography (CT) scans from the Visible Human Project (VHP) database. The CSF was modeled using solid elements with the same bulk modulus as water and a very low shear modulus. The brain, consisting of gray matter, white matter, brainstem, and cerebellum, was modeled as an isotropic material with a shear viscoelastic and volumetric elastic response. To account for the fibrous nature of white matter, the shear modulus of the white matter was assigned to be 25% higher than that of the gray matter, and to capture regional differences, the short-term shear modulus used for the brainstem was 80% higher than that for the cerebral white matter. An elastic-plastic model was used for the facial bones, and an elastic model was used for the facial skin and muscle. This new version of the WSUBIM was then validated using data from Nahum and Trosseille. Coup and contrecoup pressures predicted using the model correlated reasonably well with peak pressure data from six of Nahum's tests, and intracranial and ventricular pressures predicted using the model matched data from one of Trosseille's experiments well up to 14 ms, after which there was some discrepancy, possibly due to the CSF not being represented by fluid elements. In addition, the model was found to be stable up to a peak translational acceleration of 200 g with a duration of 20 ms and a peak rotational acceleration of 12,000 rad/s^2

with a duration of 30 ms.

The new WSUBIM was later modified to improve mesh quality and material definitions, and it was used in simulations of 24 head-to-head collisions that occurred during National Football League (NFL) games [105]. The simulations, which were conducted using PAM-CRASH, an explicit finite element analysis code, predicted pressure gradients stretching uniformly across the brain. Peak positive pressures were found to occur at the coup site, in the front temporal lobe, and peak negative pressures were found to occur at the contrecoup site, in the right occipital lobe near the posterior cerebellum. The mean values of coup and contrecoup pressure were found to be 90 ± 24 kPa and 76 ± 26 kPa respectively in injury cases. The simulations predicted a different pattern of response for the shear stresses in the brain; while high shear stresses appeared on the cortical surface of the brain initially, they gradually concentrated on the central core region of the brain, particularly the midbrain and thalamus. The mean values of shear stress in the injury cases were found to be 4.5 $\pm$ 1.2 kPa in the thalamus and 8.4 $\pm$ 2.2 kPa in the midbrain. It was found that the maximum shear stress response at the brainstem provided the strongest correlation with occurrence of mTBI, and a shear stress of 7.8 kPa was proposed as the tolerance level for a 50% probability of sustaining an mTBI.

Université Louis Pasteur Model

Another 3D human head FE model that was developed was the Université Louis Pasteur (ULP) finite element head model [38]. The skull geometry was obtained by digitizing the internal and external surfaces of an adult human skull, and the remaining head geometry was obtained using data from an anatomical atlas. The model included a skull, falx and tentorium, subarachnoid space, scalp, cerebrum, cerebellum, and brainstem. A 13,208-element mesh was generated using HyperMesh; the falx and tentorium were modeled by a layer of shell elements, the skull was modeled by a 3-layered composite shell, and the remaining features, including the CSF, were modeled with brick elements. The CSF, scalp, facial bones, and falx and tentorium were modeled as elastic materials, the skull was modeled as an elastic brittle

material capable of fracture, and the brain was modeled as a viscoelastic material.

Using the RADIOSS finite element code, the ULP model was validated using data from Nahum's experiment 37; good agreement was found between simulation results and experimental data, with a maximum difference in the main pressure peaks of less than 7%. The validated ULP model was then used to replicate a head impact caused by a motorcycle accident; high shear stress regions predicted by the model appeared in good correspondence with actual observed sites of contusion in the right temporal lobe. Later, the ULP model was coupled to a helmet FE model consisting of a linear elastic helmet shell and elastic-plastic padding [99]. The helmeted ULP model was subjected to a frontal impact with an initial velocity of 7.5 m/s, resulting in a maximum compressive stress of 169 kPa in the frontal region and a maximum tensile stress of -90 kPa in the occipital region. The highest Von Mises stresses occurred in the occipital region, in the base of the brain and the brainstem. The pressures experienced by the helmeted ULP model were largely similar to the pressures experienced by the unhelmeted ULP model during validation, although the helmeted model experienced compressive pressures that were slightly lower and tensile pressures that were slightly higher than those experienced by the unhelmeted model.

The ULP model was subsequently further validated using data from Trosseille [97]. To improve the simulation of the CSF during long duration impacts, the model was altered to represent the CSF with 3 layers of brick elements in Arbitrary Lagrangian Euler (ALE) formulation. It was found that the ALE formulation led to pressure-time histories that better matched experimental results; remaining discrepancies were attributed to lack of accurate material properties. It was noted that pressure predictions became less accurate as the distance from site of impact increased, especially for long duration impacts. The ULP model was then used to simulate 64 real world accidents — 35 helmeted and 29 unhelmeted direct head impacts. The helmeted impacts were from accidents involving motorcyclists and football players, and the unhelmeted impacts were from pedestrians impacting a car's windshield. Intracranial responses were computed using the RADIOSS code, and histograms of several mechanical parameters were correlated with injury types to derive tolerance limits for

specific injury mechanisms. It was found that intracranial pressure did not correlate with neurological injury, but that brain Von Mises stresses of 18 kPa and 38 kPa led to a 50% risk of moderate and severe neurological lesions respectively and a global CSF strain energy of 5.4 J led to a 50% risk of subdural hematoma.

University College Dublin Brain Trauma Model

A 3D FE head model was also developed by Horgan and Gilchrist at University College Dublin. The model began as a 2D plane strain FE representation of the head that included a single-layer skull, CSF, and brain [30]. The 2D slice, which was taken in an off-center mid-sagittal plane in an anteroposterior direction, consisted of 12,081 4-node quadrilateral elements [30]. The nodes were constrained in all three degrees of freedom at the base of the cranium, and the materials were modeled as homogeneous, isotropic, and linear elastic, except for the brain, which was modeled as viscoelastic. The 2D model was used in impact simulations in which the impact was represented by an approximate half sine wave pulse of magnitude 8000 N and duration 4 ms; compressive strains were found at the impact region, and tensile strains were found in the contrecoup region. It was also found that more severe levels of strain were obtained when viscoelastic properties were used for brain tissue rather than elastic properties, and occipital impacts resulted in higher magnitude coup and contrecoup strains than frontal impacts.

A 3D FE human head model known as the University College Dublin Brain Trauma Model (UCDBTM) was then developed [36]. Interpolation and thresholding schemes were used to segment CT data from a male cadaver available through the VHP and generate a polygonal model of the skull, which was then decimated and smoothed. A uniformly thick CSF layer was created along the interior surface of the skull. The resulting 3D model consisted of a scalp, 3-layer skull, dura, CSF, pia, falx, tentorium, cerebral hemispheres, cerebellum, and brainstem. The model was divided into sufficiently well-behaved meshable sections, and a number of different meshes with 9,000 to 50,000 elements were generated. Brain tissue was characterized as viscoelastic in shear and elastic in compression, and the CSF was modeled using

solid elements with a low shear modulus. Using ABAQUS, the 3D model was validated using data from Nahum; simulation results matched the experimental data well in maximum values, shape of response, and duration of effect. Parametric analyses found that the short-term shear modulus of the brain had large effects on intracranial pressure and Von Mises stress, but the bulk modulus of the brain had little effect on either pressure or Von Mises response. It was also found that careful modeling of the CSF and skull thickness was required to correctly predict intracranial pressure distribution.

Politecnico di Torino

Another FE model of the head was developed by Belingardi et al. at Politecnico di Torino [8]. CT images from a patient with brain trauma were used to construct the surfaces of the cranium and facial bones, and MRI images from a different patient were used to construct the soft tissue surfaces. The model consisted of scalp, cranial bones, facial bones, dura mater, falx and tentorium, CSF, brain tissue, and ventricles. The dura mater was obtained from the interior surface of the skull, while the falx and tentorium were built manually based on anatomical images. A 55,264-element FE mesh was generated using HyperMesh; the brain tissues and ventricles were modeled as tetrahedral elements, the scalp, CSF, and cranial bones were modeled as brick elements, and the facial bones and membranes were modeled as shell elements. A 2 mm layer of CSF, which was modeled as a linear-elastic material with a 'fluid' option that only supported hydrostatic stress states, surrounded all membranes and the brain. All tissues were modeled as linear elastic except the brain, which was modeled as a viscoelastic material with shear relaxation behavior. Using LS-DYNA, an explicit nonlinear FE code, the model was validated against Nahum's experiment 37. In order to obtain the correct peak forces in the simulation, the impactor speed was reduced from 9.6 m/s to 7 m/s, and still some discrepancies remained, possibly due to the way the CSF was modeled. Simulations using the model found high shear stresses in the brainstem and corpus callosum, which are the two tissues most affected by DAI. Additionally, results suggested that ventricles protect the brain's central area

and membranes such as the dura mater, falx, and tentorium may reduce pressure.

Additional Impact-Related TBI Studies

In addition to the studies already described, a number of other studies related to impact-related TBI have been conducted. El Sayed et al., for example, conducted finite element simulations of frontal and oblique impacts using a finite element human head model developed at the University of Salerno from MRI images available in Harvard Medical School's whole brain atlas [24]. The mesh, which consisted of 39,047 tetrahedral elements, comprised a skull, CSF, gray matter, white matter, cerebellum, corpus callosum, telencephalic nuclei, brainstem, and ventricles. The focus of their study was implementation of a variational constitutive model for soft biological tissues; the material response had elastic-plastic and viscoelastic components and included rate effects, shear and porous plasticity, and finite viscoelasticity. A hyperelastic model was used for the skull and CSF. The model was validated using data from Nahum's experiment 37; good correlation between the model and experiment was obtained. The model was then subjected to an oblique impact, which resulted in significantly higher positive and negative pressures in the coup and contrecoup regions respectively than the frontal impact, inducing focal and diffuse cavitation damage. Shear stress values were also up to 10 times higher than those observed during frontal impact, with DAI evolving from the periphery to the core of the brain and leading to permanent shear damage.

A number of other studies were also conducted with a finite element human head model developed by Kleiven and Hardy [41]. The model, which was constructed using medical imaging data from the VHP, consisted of a scalp, skull, brain, meninges, CSF, parasagittal bridging veins, and a simplified neck. It was experimentally validated against pressure and relative motion magnitude data. Simulations of frontal, occipital, and lateral impacts using a variety of material properties and interface conditions demonstrated that simulation of local brain motion is highly sensitive to the shear properties of brain tissue but relatively insensitive to the type of brain-skull interface. Pressure response, however, is more dependent on the type of brain-skull interface

than on constitutive parameters. The model was also used to investigate the effect of head size on impact-induced head trauma [42]. It was found that intracranial stresses increase with increasing head size, with maximal effective stresses in the brain ranging from 3.6 kPa for a 2.34 kg head to 16.3 kPa for a 5.98 kg head. Later, geometry of vasculature was segmented from two 3D CT angiographies and meshed, and the vasculature model was incorporated into the FE head model [33]. It was thought that since blood vessels are more rigid than cerebral tissue, they would likely stiffen the structural responses of the brain. The brain was modeled as a homogeneous cerebral tissue subject to a Mooney-Rivlin hyperelastic constitutive law, with rate effects taken into account through linear viscoelasticity. For the vasculature, in one model the arteries and veins were modeled as linear elastic, and in another model they were modeled as nonlinear elastic, using a uniaxial exponential model proposed by Fung. In LS-DYNA, short duration translational acceleration impulses were applied to the 3D finite element head models, and maximum principal strain, which can serve as a predictor for CNS injuries such as DAI, cell death, and neuronal dysfunction, was measured. It was found that the influence of the vasculature on the dynamic response of the brain was minimal; for models with nonlinear elastic and linear elastic vasculature compared to a model without vasculature, peak average strain reduction was 2% and 5% respectively. Similar results were obtained in the rotational scenario. In both the rotational and translational scenarios, the greatest influence of the vasculature was found in the central region of the brain due to planar organization of the vasculature there.

Some other studies have investigated the effects of non-contact impact. In one study, a 3D finite element human head model consisting of a skull, brain, CSF, and neck, was integrated with an articulated total body (ATB) model consisting of 17 rigid body segments connected by joints in order to simulate whole body motion [31]. The model was validated using Nahum's cadaver data; coup and contrecoup pressure traces matched well. LS-DYNA was utilized to compute deformation and stress from non-contact impact in a two-phase procedure; in the first phase, the gross motion of the whole body was computed, and in the second phase, the kinematical

components of the rigid head were used as inputs to the 3D head model. To simulate non-contact impact, a sled test system was used, in which the ATB was placed in a system including a seat, floorboard, toeboard, and seat belts (modeled by planes with shell elements), and an acceleration was applied to the whole system. Critical zones of high shear stress were observed at the frontal, rear, and neck junction (connection of the brainstem and spinal cord), implying that DAI occurs in those regions. Linear regression analysis found close correlations between peak intracranial pressure and maximum translational acceleration, and between peak shear stress and maximum rotational acceleration. The results also indicated that the widely-used head injury criterion (HIC) was insufficient to predict brain injuries caused by non-contact impact, and a more comprehensive injury criterion was needed.

Another impact-related TBI study was conducted by Takhounts et al., who developed a simplified FE head model for use with the Simulated Injury Monitor (SIMon) software package, which takes kinematic and kinetic data measured in an instrumented test dummy and applies the measured dummy response to mathematical models [83]. For ease of predicting injury, the finite element model was reduced to only essential components; the 7,852 SIMon finite element head model consisted of a skull, dura-CSF layer, brain, falx cerebri, and bridging veins. The bridging veins were represented by beam elements and the remaining structures were represented by hexagonal elements. The skull was assumed to be rigid, and the other structures were modeled as isotropic, homogeneous, and linear viscoelastic. The model was validated using experimental neural density target data, and three brain injury measures were proposed: cumulative strain damage measure (CSDM), a correlate for DAI, dilatation damage measure (DDM), a correlate for contusions, and relative motion damage measure (RMDM), a correlate for acute subdural hematoma. Experimental animal data were used to establish injury thresholds. The SIMon FEHM was then subjected to frontal and side impacts using test data from the U.S. National Highway Traffic Safety Administration database; simulation results found that the brain experienced greater deformations in side impact tests than frontal impact tests.

Numerous other studies have also been conducted using 2D FE head models.

One study, for example, demonstrated through 2D simulations that translational accelerations could lead to high shear stresses in the corpus callosum and brainstem consistent with DAI [64]. The 7,558-element model of the coronal section included the cranium, falx and tentorium, cerebrum, CSF, lateral ventricle, third ventricle, and interpeduncular cistern, and it was validated using data from Nahum's cadaver experiments [64]. The cranium was modeled as elastic-plastic with damage, while the brain and CSF were characterized as linear viscoelastic. Using the PAM-CRASH finite element code, the head model was subjected to a 2 m/s impact, which resulted in a maximum shear stress of 176 kPa at the rostral brainstem and a shear stress of 94 kPa in the corpus callosum. This was consistent with small hemorrhages in the corpus callosum and brainstem found in CT scans of DAI patients; it thus demonstrated that pure translational direct impacts could reproduce DAI. Subsequent simulations found that the removal of the falx and tentorium significantly reduced the concentration of shear stress. The results suggested that the mechanism of DAI involves concentration of shear stress on the core of the brain, due to the effects of internal membranes.

2.2 Blast-Related TBI

Researchers have only recently begun to investigate TBI induced by blasts rather than impacts, and thus far there have been three models of blast-related TBI. One of the models was developed by Taylor and Ford, who constructed a high-resolution finite element human head model and subjected the head to anterior, posterior, and lateral blasts; the results demonstrated that blast waves can cause focal injury to the head [85]. The model, which had 1 mm cubic resolution and was constructed from high-resolution photographic data of a cryogenically frozen human female available from the VHP, consisted of a skull, white matter, gray matter, and CSF. The skull was represented by a compressible, linear elastic, perfectly plastic constitutive model with a damage model to capture fracture, the white and gray matter were represented by an elastic compressible equation-of-state model for the volumetric response and a three-term Maxwell viscoelastic model for the deviatoric response, and the CSF

was modeled using a nonlinear tabular equation of state for water. Dry air occupied the sinuses, with air modeled using a nonlinear tabular equation of state. Using CTH, an Eulerian finite volume code, the head model was subjected to a 1.3 MPa blast wave (equivalent to a 3 kg charge of Octol at 2-3 m) from anterior, posterior, and lateral directions. The blast conditions were selected to investigate blast injury scenarios that were otherwise predicted to be survivable. Transmitting boundary conditions were positioned downstream from the head and at the base of the neck, and simulations were run to 2 ms. It was noted that due to differences in acoustic impedance between the air and skull, the pressure wave was shocked up from 1.3 MPa to over 4 MPa at the air-skull interface. Within the head, it was found for all blast orientations that maximum pressures occurred at the coup site, closest to the blast source, and maximum volumetric tensions occurred primarily at the contrecoup site; pressures reached 3-4 MPa at the coup site and tensions reached 0.8 MPa at the contrecoup site. The highest coup pressures were produced in the lateral blast scenario. For shear stresses, all blast orientations generated high shear stresses in the subfrontal regions and brainstem areas, but the anterior and posterior blasts also resulted in elevated shear stresses in the temporal lobes and the cortical area, while the lateral blast resulted in elevated shear stresses that were diffusely distributed in the right hemisphere and concentrated in focal areas in the left hemisphere. The results of this study thus demonstrated that blasts could lead to the development of significant levels of pressure, volumetric tension, and shear stress in focal areas, possibly contributing to the development of TBI, on a time scale shorter than that associated with intracranial accelerations, which tend to develop over 5-20 ms. They also demonstrated, though, that the stress response patterns are dependent on the orientation of the blast wave and the complex geometry of the skull, brain, and tissue interfaces.

Another model was developed by Moss and King [59]. After conducting blast simulations with an extremely simplified head model, they concluded that blasts could induce sufficient skull flexure to generate potentially damaging loads in the brain. In their model, the skull was represented as a hollow elastic ellipsoid containing a vis-

coelastic brain surrounded by a layer of CSF. A simplified face, neck, and body were also included. The model was first subjected to a 5 m/s impact. In that simulation, the head was fully encased in a steel-shell helmet with an inner layer of crushable foam, and the head-helmet system was impacted against a rigid wall; following impact, large positive pressure was observed at the coup site, and negative pressure was observed at the contrecoup site. Then, using ALE3D, an arbitrary Lagrangian-Eulerian finite element hydrocode, a series of blast simulations were conducted. In one blast simulation, an unprotected head was subjected to a 100 kPa blast wave generated from 2.3 kg of C4 at 4.6 m. It was observed that the blast wave front induced transverse bending displacements of approximately 50 μm in the skull, producing pressures up to 300 kPa and even larger pressure gradients. As a result, the authors asserted that most of the mechanical load in the brain from the blast simulation was produced by skull flexure. Parametric studies found that increasing the stiffness of the skull yielded lower shear strains, peak pressures, and pressure gradients.

Blast simulations were then conducted with helmeted heads, with the helmets modeled as hemi-ellipsoidal Kevlar shells. For a helmet with a webbed suspension, the blast wave washed under the helmet, resulting in geometric focusing of the blast wave that caused pressure under the helmet to exceed pressure outside the helmet. For a helmet with foam padding, the underwash effect was mostly prevented, but motion of the helmet was more strongly coupled to the head. Stiffer foams were found to transfer greater forces from the helmet to the skull and increase mechanical loads in the brain than softer foams, but even soft foams only partially reduced blast-induced pressures, since the helmet did not cover enough of the head at the back and sides to prevent skull deformation.

The simulations thus demonstrated that a blast could cause the skull to dynamically deform, causing localized regions of high and low pressure and large pressure gradients, and that helmets could affect the interaction of the blast with the head. However, the significance of the results is limited, given the grossly unrealistic geometries of the head and helmet and the lack of anatomical structures in the model; the model fails to capture any of the effects of the human head's complex geometry on

blast wave propagation.

Chafi et al. also developed a blast-related TBI model [13]. The 3D FE head model, which had previously been validated against intracranial pressures, shear strains, and principal strains from cadaveric impact experiments, consisted of a brain, falx and tentorium, CSF, dura mater, pia mater, skull, and scalp. In the 27,971-element model, the scalp was represented by two layers of 8-noded solid elements, the skull was represented by 4 layers of solid elements, the brain and CSF were represented by 8-noded solid elements, and the membranes were represented by 4-noded shell elements. Brain tissue was modeled using a hyperelastic Mooney-Rivlin model combined with a linear viscoelastic model, and the skull, scalp, and membranes were modeled as linear elastic materials. The CSF was represented by linear elastic elements with a fluid option, and a tied contact algorithm was used to model brain-membrane interfaces. LS-DYNA was used to conduct blast simulations to 5 ms; the standoff distance was 80 cm, and the amounts of TNT were 0.0838, 0.205, and 0.5 lbs, leading to overpressures in the range of 2.4-8.7 atm. A free boundary condition was used at the neck junction. As expected, larger amounts of explosive led to earlier peak arrival times and higher pressures, shear stresses, and strains. The blasts typically resulted in a major positive peak at the coup site and a major negative peak at the contrecoup site, followed by considerable positive and negative peaks due to translational and rotational movements of the brain at both the coup and contrecoup sites. These results demonstrated that blast waves could generate significant levels of pressure prior to any head movement. Based on proposed concussion thresholds in the literature, it was found that the peak pressures in the 0.5 and 0.205 lb TNT scenarios exceeded the concussion threshold of 235 kPa at the coup and contrecoup sites, but not in the cerebellum, corpus callosum, and brainstem, and peak pressures in the 0.0838 lb TNT scenario exceeded the concussion threshold only at the coup site. The blasts also resulted in high localized shear stresses, particularly in the brainstem, corpus callosum, and white matter. Time histories of the average maximum shear stresses showed that the maximum stresses occurred after the initial peak, when the propagation of the blast wave caused acceleration and translational motion. Based on proposed injury

criteria in the literature, it was found that 0.5 lb TNT could cause axonal injury at the coup and contrecoup sites, cerebellum, corpus callosum, and brainstem, 0.205 lb TNT could cause axonal injury at the coup and contrecoup sites and the brainstem, and 0.0838 lb TNT could cause axonal injury at the coup and contrecoup sites. It was also found that the principal strain in the brain had a similar response pattern to the shear stress response pattern, with high strains initially located on the cortical surface of the brain gradually concentrating at the white matter, corpus callosum, and brainstem. Based on injury criteria based on principal strain, 0.5 lb TNT could cause brain injury in the cerebellum, corpus callosum, and brainstem, and 0.205 lb TNT could cause brain injury at the brainstem. The simulations thus suggested that blasts with overpressures ranging from 2.4 to 8.7 atm could lead to concussion, axonal injury, and other brain injury at various locations in the brain.

2.3 Summary

A number of finite element head models have been developed for use in impact-related TBI simulations, and many of the models have been validated against data from cadaver experiments conducted by Nahum and Trosseille. The computational models have been used to study injury mechanisms, indicators, and thresholds for impact-related TBI. For example, the Wayne State University Brain Injury Model was used in simulations of head-to-head collisions in NFL games, and results from the simulations showed that shear stress at the brainstem provided the strongest correlation with TBI. The Université Louis Pasteur Model was used to simulate 64 real world accidents, and it was found that intracranial pressure did not correlate with neurological injury, but Von Mises stress did. Other studies have also demonstrated that intracranial stresses increase with increasing head size and that vasculature has a minimal effect on brain response to direct impacts. Over the years, many aspects of impact-related TBI have been explored through computational models.

However, research has only recently begun on blast-related TBI. Thus far, very few computational studies of blast-related TBI have been conducted. In one study,

Moss and King subjected a simplified model of the head to blasts and found that skull flexure led to pressure extrema in the brain; the significance of the results, however, is limited, given the crude geometry and lack of anatomical structures. Preliminary blast studies have also been conducted by Taylor and Ford and Chafi et al.; the simulations were conducted with more detailed finite element head models than the one used by Moss and King, and results demonstrated that blasts could lead to focal areas of elevated intracranial pressure, shear stress, and strain that could lead to traumatic brain injury. However, these models also have limitations, as they lack anatomical detail and have not been validated. There still exists a need for a biofidelic head model that can be used in a simulation environment that accurately captures initialization and propagation of blast waves in order to understand the mechanical response of the brain to blasts.

Chapter 3

Modeling Framework

3.1 Computational Framework

The blast simulations were conducted using an extension of the Virtual Test Facility (VTF), a suite of computational fluid dynamics (CFD) and computational solid dynamics (CSD) solvers that are coupled through an integration framework that facilitates simulations of blast-wave loading of solids on high performance massively parallel computing platforms [19, 20]. The CSD solver used in the blast simulations was Adlib, a Lagrangian finite element solid solver, and the CFD solver used was AMROC (Adaptive Mesh Refinement in Object-Oriented C++), an Eulerian fluid solver. Constitutive models describing the mechanical response of various tissues and biological structures have been added to Adlib, and a point source model that accurately describes blast wave initialization has been integrated into AMROC. Both Adlib and AMROC have been implemented in parallel, as described in [20].

3.1.1 Adlib

Adlib is based on a conventional Lagrangian formulation for describing large deformations of solids [20]. Here we briefly outline the continuum framework and numerical formulation.

Continuum Framework

The motion of a reference body B_0 can be described by the deformation mapping $\mathbf{x} = \varphi(\mathbf{X}, t)$, where $\mathbf{X}$ gives the coordinates of points in B_0 and $\mathbf{x}$ gives the positions of material particles $\mathbf{X}$ at time t; velocity and acceleration are given by $\dot{\varphi}(\mathbf{X}, t)$ and $\ddot{\varphi}(\mathbf{X}, t)$ respectively. Local deformation is described by the deformation gradient:

$$\mathbf{F} = \nabla_0 \varphi(\mathbf{X}, t) \tag{3.1}$$

where ∇_0 is the material gradient defined over B_0. The determinant of $\mathbf{F}$, $J = \det(\mathbf{F}(\mathbf{X}, t))$, is the Jacobian of the deformation and a measure of the ratio of the deformed to undeformed volume. The motion of the body is subject to conservation of linear momentum, which is given by:

$$\nabla_0 \cdot \mathbf{P} + \rho_0 \mathbf{B} = \rho_0 \ddot{\varphi} \tag{3.2}$$

where $\mathbf{B}(\mathbf{X}, t)$ is the body force, $\mathbf{P}(\mathbf{X}, t)$ is the first Piola-Kirchhoff stress tensor, and $\rho_0(\mathbf{X})$ is the mass density. The symmetric Cauchy stress tensor σ can be obtained from the first Piola-Kirchhoff stress tensor $\mathbf{P}$ through the relation:

$$\sigma = J^{-1} \mathbf{P} \mathbf{F}^T \tag{3.3}$$

We can additively decompose $\mathbf{P}$ into an equilibrium part $\mathbf{P}^e$ and a viscous part $\mathbf{P}^v$:

$$\mathbf{P} = \mathbf{P}^e + \mathbf{P}^v \tag{3.4}$$

In materials without strength, $\mathbf{P}^e$ reduces to:

$$\mathbf{P}^e = -Jp\mathbf{F}^{-T} \tag{3.5}$$

where p is the hydrostatic pressure obtained from an equation of state. We adopt the fluids convention and regard compressive pressure as positive and tensile pressure as

negative. We also assume Newtonian viscosity, where the viscous Cauchy stress σ^v is given by:

$$\sigma^v = 2\eta_h(\text{sym}\dot{\mathbf{F}}\mathbf{F}^{-1})^{\text{dev}} \tag{3.6}$$

η_h is the Newtonian viscosity coefficient, and sym and dev denote the symmetric and deviatoric components of a tensor respectively. $\mathbf{P}^v$ can then be obtained:

$$\mathbf{P}^v(\dot{\mathbf{F}}, \mathbf{F}) = J\sigma^v\mathbf{F}^{-T} \tag{3.7}$$

The boundary conditions for the problem are formulated by partitioning the boundary ∂B_0 into a Dirichlet boundary ∂B_{01} and a Neumann boundary ∂B_{02}. The boundary conditions are then given by:

$$\varphi = \bar{\varphi} \quad \text{on} \quad \partial B_{01} \tag{3.8}$$

$$\mathbf{P} \cdot \mathbf{N} = \bar{\mathbf{T}} \quad \text{on} \quad \partial B_{02} \tag{3.9}$$

where $\bar{\varphi}$ is the prescribed deformation mapping on ∂B_{01}, $\mathbf{N}$ is the unit outward normal to ∂B_{02}, and $\bar{\mathbf{T}}$ are the prescribed tractions on ∂B_{02}. We can then obtain the weak form of the field equations. Starting from:

$$\nabla_0 \cdot \mathbf{P} + \rho_0\mathbf{B} = \rho_0\ddot{\varphi} \quad \text{in} \quad B_0 \tag{3.10}$$

$$\mathbf{P} \cdot \mathbf{N} = \bar{\mathbf{T}} \quad \text{on} \quad \partial B_{02} \tag{3.11}$$

we enforce the governing equations weakly:

$$\int_{B_0} (\nabla_0 \cdot \mathbf{P} + \rho_0\mathbf{B} - \rho_0\ddot{\varphi})\,\mathbf{v}\,d\Omega + \int_{\partial B_{02}} (\mathbf{P} \cdot \mathbf{N} - \bar{\mathbf{T}})\,\mathbf{v}\,dS = 0 \tag{3.12}$$

for all $\mathbf{v}$ in the space of admissible displacements V. Integrating by parts and applying the boundary conditions, we arrive at the principle of virtual work:

$$\int_{B_0} \rho_0\mathbf{B} \cdot \mathbf{v}\,d\Omega - \int_{B_0} \mathbf{P} : \nabla_0\mathbf{v}\,d\Omega + \int_{\partial B_{02}} \bar{\mathbf{T}} \cdot \mathbf{v}\,dS = \int_{B_0} \rho_0\ddot{\phi} \cdot \mathbf{v}\,d\Omega \tag{3.13}$$

Numerical Formulation

The continuum framework is then implemented using a time discretization of the momentum and constitutive equations and a finite element discretization of the solid. We first consider finite element interpolations of the form:

$$\varphi_h(\mathbf{X}) = \sum_{a=1}^{N} x_a N_a(\mathbf{X}) \tag{3.14}$$

where φ_h is the deformation mapping interpolant, x_a is the current position at node a, N_a are the displacement shape functions, and a ranges over N nodes. In the simulations, we used 10-noded quadratic tetrahedral elements. We can then write the principle of virtual work as:

$$\int_{B_0} \rho_0 \mathbf{B} N_a \, d\Omega + \int_{\partial B_0} \bar{\mathbf{T}} N_a \, dS - \int_{B_0} \mathbf{P} : \nabla_0 N_a \, d\Omega = \int_{B_0} \rho_0 N_a N_b \, d\Omega \, \ddot{x}_b \tag{3.15}$$

This can also be written as $\mathbf{f}_a^{ext} - \mathbf{f}_a^{int} = \mathbf{f}_a^{inert}$, where:

$$\mathbf{f}_a^{ext} = \int_{B_0} \rho_0 \mathbf{B} N_a \, d\Omega + \int_{\partial B_0} \bar{\mathbf{T}} N_a \, dS \tag{3.16}$$

$$\mathbf{f}_a^{int} = \int_{B_0} \mathbf{P} : \nabla_0 N_a \, d\Omega \tag{3.17}$$

$$\mathbf{f}_a^{inert} = \int_{B_0} \rho_0 N_a N_b \, d\Omega \, \ddot{x}_b \simeq \mathbf{M}_{ab} \ddot{x}_b \tag{3.18}$$

$\mathbf{f}_a^{ext}$, $\mathbf{f}_a^{int}$, and $\mathbf{f}_a^{inert}$ are the external, internal, and inertial forces respectively, and $\mathbf{M}$ is the diagonal lumped mass matrix.

For the temporal discretization, we use a Newmark time-stepping algorithm:

$$\mathbf{x}_a^{n+1} = \mathbf{x}_a^n + \Delta t \dot{\mathbf{x}}_a^n + \Delta t^2 \left[\left(\frac{1}{2} - \beta \right) \ddot{x}_a^n + \beta \ddot{x}_a^{n+1} \right] \tag{3.19}$$

$$\dot{\mathbf{x}}_a^{n+1} = \dot{\mathbf{x}}_a^n + \Delta t [(1-\gamma)\ddot{\mathbf{x}}_a^n + \gamma \ddot{\mathbf{x}}_a^{n+1}] \tag{3.20}$$

$$\ddot{\mathbf{x}}_a^{n+1} = \mathbf{M}_{ab}^{-1} [\mathbf{f}^{ext} - \mathbf{f}^{int}]_b^{n+1} \tag{3.21}$$

where β and γ are Newmark parameters. In the simulations, we use $\beta = 0$ and $\gamma = \frac{1}{2}$, which results in an explicit, second-order accurate time integration scheme.

Artificial Viscosity

An artificial viscosity scheme was implemented to enable the simulation of strong three-dimensional shocks in solids [48]. The addition of artificial viscosity spreads the shock front over several grid points without affecting key aspects of shock dynamics such as shock speed and without introducing artifacts such as spurious oscillations in the shock profile [48]. We assume the viscosity coefficient comprises two terms:

$$\eta_h = \eta + \Delta\eta \tag{3.22}$$

where η is the physical viscosity coefficient of the material and $\Delta\eta$ is the added artificial viscosity [48]. At a given Gauss quadrature point, the artificial viscosity coefficient $\Delta\eta$ is given by:

$$\Delta\eta = \begin{cases} \max(0, -\frac{3}{4}h\rho(c_1\Delta u - c_L a) - \eta) & \Delta u < 0 \\ 0 & \Delta u \geq 0 \end{cases} \tag{3.23}$$

where h is a measure of the element size, Δu is a measure of the velocity jump across the element, c_1 and c_L are coefficients, a is the characteristic sound speed, and $\rho = \rho_0/J$ is the mass density per unit deformed volume [48]. To ensure that the artificial viscosity formulation is material frame indifferent, we use the following relation for Δu:

$$\Delta u = h\frac{\partial \log J}{\partial t} \tag{3.24}$$

where $h = (Jd!|K|)^{1/d}$, d is the dimension of space, and $|K|$ is the volume of element K in its reference configuration [48]. The velocity jump is approximated as:

$$\Delta u_{n+1} = h_{n+1}\frac{\log J_{n+1} - \log J_n}{\Delta t} \tag{3.25}$$

This artificial viscosity is deviatoric, and parameter values were obtained through calibrations using simple shock applications. For the skull, the artificial viscosity parameters used were $c_1 = 25.0$ and $c_L = 1.0$, and for all remaining head structures, the parameters used were $c_1 = 25.0$ and $c_L = 0.4$.

3.1.2 AMROC

AMROC, the Eulerian fluid solver used in the blast simulations, is a complex, multi-level simulation code that has the capability to simulate flows with strong shocks, fluid mixing, and highly coupled fluid-structure interaction (FSI) problems [20]. It utilizes a time-explicit finite volume discretization that achieves a proper upwinding in all characteristic fields. In order to efficiently obtain the necessary temporal and spatial resolution, the structured adaptive mesh refinement method is adopted; following a patch-oriented approach, cells flagged by various error indicators are clustered into non-overlapping rectangular grids. Refinement grids are derived recursively from coarser ones, constructing a hierarchy of successively embedded levels. A more detailed description of AMROC is given in [20].

To initialize blasts, a point source blast initialization code developed by Dr. Tan Bui based on calculations in [66] has been incorporated into AMROC. The point source blast initialization is based on the released explosive energy, as determined by the type and mass of the explosive, and the distance between the explosion and the target structure [5]. The model assumes that blast waves are produced by an ideal explosion source — that is, by the instantaneous deposition of a fixed quantity of energy at an infinitesimal point in a uniform atmosphere — and thus that the energy produced depends only on the total source energy. The solver uses a finite difference scheme to solve for the flow parameters and obtain the solution for the fully formed blast wave; excellent agreement has been found between results using the initialization code and results from air blast experiments. A more detailed explanation of the point source model and the validation of the blast initialization code is available in [5].

3.1.3 Fluid-Structure Interaction

In the VTF, a loosely coupled approach to fluid-structure interaction is applied [20]. The fluid and solid domains are assumed to be disjoint, with interaction taking place only at the fluid-solid interface, allowing the use of a Lagrangian solid solver and an Eulerian fluid solver. The information exchange is reduced to communicating the velocities and the geometry of the solid surface to the Eulerian fluid and imposing the hydrostatic pressure onto the Lagrangian solid as a force acting on its exterior. A temporal splitting method is applied to update the position and velocity of the boundary between time steps. To represent the evolving surface geometry on the Eulerian fluid mesh, a "ghost fluid" approach is used in which some interior cells are used to directly enforce the embedded boundary conditions in the vicinity of the solid surface. As the solid deforms, the solid-fluid boundary is represented implicitly in the fluid solver with a level set function that is constructed on-the-fly from the solid surface mesh. Block-structured mesh adaptation with time step refinement in the fluid allows for the efficient consideration of disparate fluid and solid time scales.

3.2 Mesh Generation

The geometry for the full head was provided by Dr. David Moore, a neurologist and TBI Scientific Advisor to the Director of the Defense and Veterans Brain Injury Center (DVBIC). Dr. Moore downloaded high-resolution T1 Magnetic Resonance (MR) images from the Montreal Neurological Institute at an isotropic voxel dimension of 1 x 1 x 1 mm. The MR images were then merged with bone windowed Computed Tomography (CT) images of the head, allowing skull reconstruction using a mutual information algorithm. The volume set of images was semi-automatically segmented into topological closed regions of interest and exported as VRML (Virtual Reality Modeling File) files. The segmentation was performed using Amira, an imaging software analysis suite that allows structured regional labeling of image data as well as filtering and co-registration. The images were segmented into 11 distinct head structures: cerebrospinal fluid (CSF), eyes, glia, ventricles, venous sinus, air sinus, muscle,

skull, skin/fat, white matter, and gray matter.

The VRML files obtained from Dr. Moore were then imported into Ansys ICEM CFD, a meshing software capable of importing CAD models of high topological and geometrical complexity and producing volumetric conformal computational meshes. The software provides mesh decimation, refinement, and smoothing algorithms that can be used to optimize the mesh for computational efficiency. An unstructured finite element mesh was constructed using the Delaunay tetrahedral mesh generation algorithm, and the software's built-in smoothing and decimation functions were used to optimize and coarsen the mesh to obtain a variety of computational meshes with different resolutions. It was determined that meshes with fewer than 700,000 elements were too coarse to describe the intricate topology of some human head anatomical structures relevant for blast injury analysis. Thus, computational meshes ranging from 700,000 to 5,000,000 elements were produced. To balance mesh resolution and computational requirements, a mesh with 743,341 elements was used in the simulations described. The mesh was then further optimized by eliminating bad quality tetrahedra using the HealMesh optimization library. This model is referred to as the DVBIC/MIT Full Head Model (FHM). Figure 3-1 displays views of the skin/fat, gray matter, and white matter meshes from the FHM. Figure 3.2 shows the FHM with cuts in the sagittal, coronal, and axial planes.

(a) Skin/Fat (b) Gray Matter (c) White Matter

Figure 3-1: Detailed views of the skin/fat, gray matter, and white matter structures in the FHM

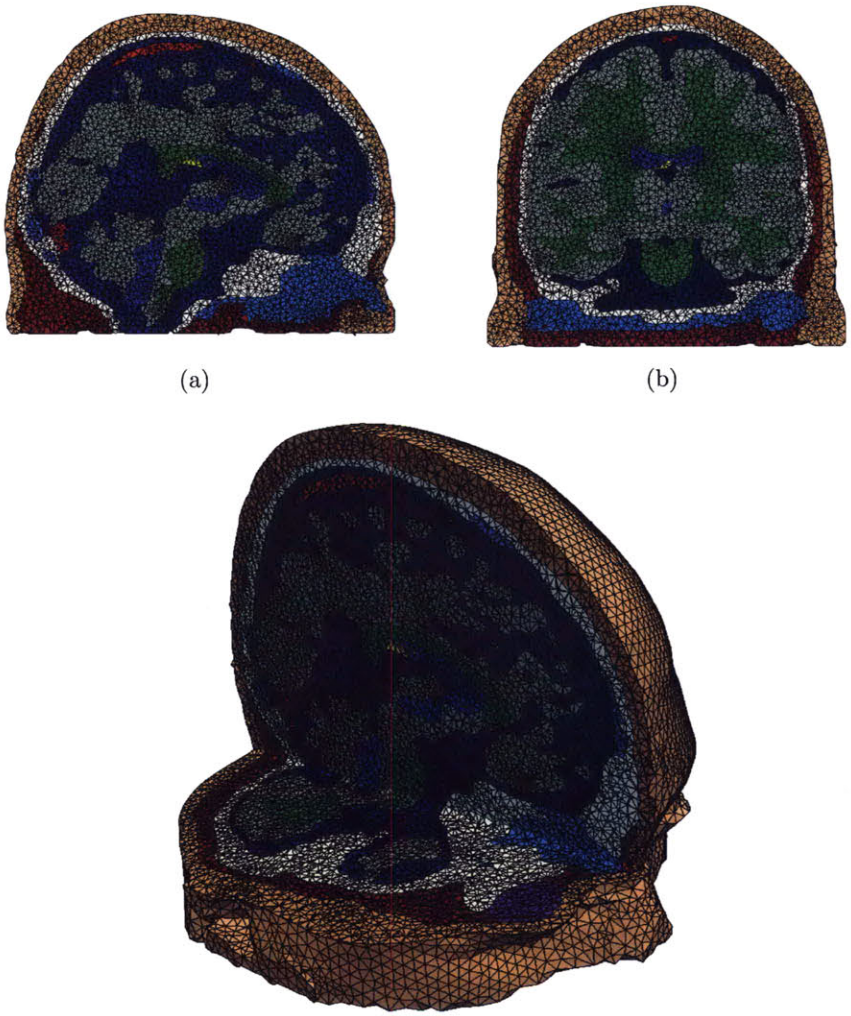

(a) (b)

(c)

Figure 3-2: Full head model: sagittal cut 3-2(a), coronal cut 3-2(b), and combined sagittal and axial cut showing detail of the full mesh 3-2(c)

3.3 Material Models and Properties

The constitutive response of brain tissue encompasses a variety of complex mechanisms including nonlinear viscoelasticity, anisotropy, and strain rate dependence [78, 92]. Several investigations have focused on characterizing this response experimentally [15, 29, 46, 56, 55, 58, 71, 92] and on developing a variety of constitutive models to capture the behavior of the brain [10, 22, 54, 78]. Owing to the complexities and inherent variability associated with biological tissue, there is significant uncertainty in quantifying tissue response to material stresses, particularly at high strain rates such as those occurring during blast wave propagation. Computational models have therefore usually favored simpler models with few parameters that can be quantified with less uncertainty, instead of more sophisticated models with many parameters that are harder to estimate with confidence.

In impact TBI modeling work, isotropic elastic models have been used to derive the volumetric response, while linear viscoelastic effects have been considered in the deviatoric response via a time-dependent shear modulus evolving from an instantaneous to a long-term value [8, 97, 103]. We can expect deferred deformation or stress relaxation due to viscoelastic effects to play a secondary role under blast loading, where the characteristic times seldom exceed a few milliseconds. However, potential nonlinear viscoelastic effects may occur with relaxation times that can be much shorter at blast deformation rates. For simplicity and due to the unavailability of high-rate tissue properties, these effects were neglected.

The description of the pressure wave propagating through the brain was parameterized through suitable equations of state. To this end, the volumetric response of the skull was described by the Hugoniot equation of state, which is used to describe the shock response of many solid materials. The volumetric response of the remaining head structures was described by the Tait equation of state, which is commonly used to model fluids under large pressure variations. Since the structures within the cranial cavity are soft tissues embedded in a fluid medium, the Tait equation of state is an appropriate model as a first approximation. The deviatoric response was described

using an elastic model.

3.3.1 Hugoniot Equation of State

The Hugoniot equation of state was used to describe the volumetric response of the skull under high strain rate conditions. The shock response of many solid materials is well described by the Hugoniot relation $U_s = C_0 + sU_p$ between the shock wave velocity U_s and the material velocity U_p [23, 52, 102]. C_0 and s are material parameters that can be obtained from experiments. By considering the equation and conservation of mass and momentum in a control volume at the shock front, the final pressure can be calculated explicitly as a function of the Jacobian behind the shock front J_H and the reference density ahead of the shock ρ_0 [23, 52, 102]:

$$P_H = \frac{\rho_0 C_0^2 (1 - J_H)}{[1 - s(1 - J_H)]^2} \tag{3.26}$$

J_H is related to the density ρ_H, the specific volume V_H, and the deformation gradient F_H, defined behind the shock front, by:

$$J_H = \frac{\rho_0}{\rho_H} = V_H V_0 = \det(F_H) \tag{3.27}$$

The relation Equation 3.26, called the "shock Hugoniot," relates any final state of density to its corresponding pressure. The deformation path taken by the material between the initial state (P_0, V_0) and the final state (P_H, V_H) is then defined by a straight line in the (σ_1, V) plot where σ_1 is the axial stress in the shock direction: the Rayleigh line [23, 52, 102].

3.3.2 Tait Equation of State

The Tait equation of state, which is commonly used to model fluids under large pressure variations, is given by:

$$P = B\left[\left(\frac{\rho}{\rho_0}\right)^{\Gamma_0 + 1} - 1\right] \tag{3.28}$$

where B and Γ_0 are constants [87]. The Tait equation of state provides a reasonable representation of the volumetric response of soft tissues embedded in a fluid medium and was therefore employed to describe the tissue response of all the head structures except the skull. To obtain the necessary parameters, Γ_0 was taken to be the value for water, 6.15. Appropriate bulk modulus values K were selected from the literature, and B was computed for each structure from Γ_0 and K using the relation $K = B(\Gamma_0 + 1)$.

3.3.3 Deviatoric Elasticity

To account for the deviatoric response of the materials, an elastic deviatoric model was combined with the volumetric equation of state using a stress-strain relation of the following form [18, 35, 68]:

$$\sigma = -pI + J^{-1}F^e\left[\mu(\log\sqrt{C^e})^{\text{dev}}\right]F^{eT} \tag{3.29}$$

where $\mathbf{C}^e = \mathbf{F}^{eT}\mathbf{F}^e$ is the elastic right Cauchy-Green deformation tensor, $\log\sqrt{\mathbf{C}^e}$ is the logarithmic elastic strain, μ is the shear modulus, and p is the pressure obtained from the equation of state.

3.3.4 Material Properties

The material properties used in the simulations, which are given in Table 3.1 and Table 3.2, were derived from values provided by Dr. Moore and values found in the literature. The following sections briefly explain how the material properties for each structure were selected.

Material	Density (kg/m^3)	K (Pa)	G (Pa)	C_0	s
Skull	1412	3.86×10^9	2.664×10^9	1850.0	0.94

Table 3.1: Hugoniot Equation of State and Deviatoric Elasticity Parameters

Material	Density (kg/m^3)	K (Pa)	G (Pa)	Γ_0
CSF	1040	2.19×10^9	2.225×10^4	6.15
Eyes	1040	2.19×10^9	2.253×10^4	6.15
Glia	1040	2.19×10^9	2.816×10^4	6.15
Muscle	1040	3.33×10^6	3.793×10^4	6.15
Air Sinus	1040	2.19×10^9	2.225×10^4	6.15
Skin/Fat	1040	3.479×10^7	5.88×10^6	6.15
Venous Sinus	1040	2.19×10^9	2.013×10^4	6.15
Ventricle	1040	2.19×10^9	2.225×10^4	6.15
White Matter	1040	2.19×10^9	2.816×10^4	6.15
Gray Matter	1040	2.19×10^9	2.253×10^4	6.15

Table 3.2: Tait Equation of State and Deviatoric Elasticity Parameters

CSF

Cerebrospinal fluid (CSF), a Newtonian fluid similar to water in density and viscosity, was modeled as a nearly incompressible solid in the simulations. The bulk modulus and density were assumed to be identical to those for water, and the shear modulus was derived from values provided by Dr. Moore. The values selected, $\rho = 1040\,\mathrm{kg/m^3}$, $K = 2.19 \times 10^9$ Pa, and $G = 2.225 \times 10^4$ Pa, fall well within the range of values used for CSF in the literature, some of which are listed in Table 3.3.

Material properties for CSF vary widely in the literature, and in general little explanation is given for how the values were selected. Bulk modulus values in particular span a wide range, from 2.0×10^5 to 2.19×10^{10} Pa, since the bulk modulus, when calculated from the Young's modulus E and Poisson's ratio ν, is extremely sensitive to small variations in ν for virtually incompressible materials with Poisson's ratios near 0.5. In a number of studies in the literature, material property values were selected based on qualitative characteristics of CSF. Gong, for example, used a Poisson's ratio close to 0.5 in order to capture the incompressible fluid behavior of CSF [31], Horgan used the bulk modulus of water and a very low shear modulus due to the fluid nature of CSF [37], and Zhang used the bulk modulus of water and a very low shear modulus to accommodate the pressure gradient and relative movement of the brain [104]. Nishimoto assigned the bulk modulus of the CSF to be $\frac{1}{100}$ that of brain tissue because the dilatation of CSF was considered to be greater than that of brain

tissue [64], and Ruan assigned the CSF lower shear and bulk moduli values than the brain in order to allow the brain to move within the skull [74]. Only Willinger even partially used experimental results, finding the value of E through modal analysis [97]; that value was adopted by Raul [73] and Belingardi [8]. However, even using the same E and ν values, Belingardi calculated a bulk modulus value of 2.0×10^5 Pa [8], while Willinger decided to use a bulk modulus value of 2.19×10^{10} Pa [97]. Thus, we can see that significant variation exists in the material property values reported for CSF in the literature, and the values appear to be largely based on qualitative assessments of the nature of CSF.

Since the CSF resides in the subarachnoid space and the cerebral ventricular system, the material properties for CSF were applied to both the CSF structure in the FHM, which encompasses the subarachnoid space in the head, and the ventricles structure in the FHM. Belingardi similarly applied the material properties of CSF to the ventricles [8], while Zhang used the properties of CSF, but with a lower shear modulus, for the ventricles [103]. Additionally, the air sinuses, which are air-filled cavities within the skull and facial bones, were assigned the material properties of CSF as a first approximation; this approximation was also made by Ho [33] and Kleiven and Hardy [41].

Source	ρ (kg/m^3)	K (Pa)	G (Pa)	E (Pa)	ν
Ruan (1994) [74]	1040	2.19×10^7	5.0×10^5		0.489
Nishimoto (1998) [64]	1040	2.19×10^7	5.2×10^5		
Gilchrist (2001) [30]				1.485×10^5	0.499
Zhang (2001) [104]	1004	2.19×10^9	5.0×10^2		
Kleiven (2002) [41]	1000	2.1×10^9			0.5
Willinger (2003) [97]	1040	2.19×10^{10}		1.2×10^4	0.49
Horgan (2004) [37]	1000			Water	0.5
Belingardi (2005) [8]	1040	2.0×10^5		1.2×10^4	0.49
Raul (2006) [73]	1040			1.2×10^4	0.49
Ho (2007) [33]	1000	2.1×10^9			0.5
El Sayed (2008) [24]	1004	2.19×10^6	5.0×10^2		
Gong (2008) [31]	1040	2.19×10^6			0.489
Taylor (2009) [85]	1000	1.96×10^9			0.50
Chafi (2010) [13]	1000	2.19×10^9			0.50

Table 3.3: CSF Material Properties from the Literature

Gray and White Matter

Material properties for brain tissue also vary widely in the literature, as the properties are extremely sensitive to a number of factors, including species, strain rates, specimen harvesting, testing methods, regional differences, and differences between *in vivo*, *in situ*, and *in vitro* specimens. For example, the mechanical properties of fresh human brain tissue have been reported to be nearly 30% higher than those of porcine and bovine brain tissues, but an order of magnitude lower than properties obtained from human autopsies conducted days after death [13]. Some of the material properties reported in the literature for homogeneous brain tissue are listed in Table 3.4.

The bulk modulus is widely accepted to be 2.19 GPa, since experimental characterization of brain tissue, which is 78% water, suggests that brain tissue exhibits incompressible viscoelastic behavior [103]. Shear modulus values, on the other hand, vary from 1.03×10^4 to 1.68×10^6 Pa. In some studies, the shear modulus values were based on experimental data. For example, Nishimoto [64], Willinger [100], and Gong [31] adopted shear modulus values from *in vitro* experiments conducted by Shuck and Advani in 1972 on specimens of human brain tissue obtained fresh from autopsies [79]. In other studies, the shear modulus values were based on other modeling work. Willinger, for example, later used shear modulus values scaled from a 2D parametric finite element study conducted by Khalil in 1977, and those same values were adopted by Raul [73]. Chafi adopted shear modulus values based on work done by Mendis et al. [13].

In the FHM, gray and white matter are considered distinct structures with differing material properties. The material property values reported in the literature for gray matter, which consists of neuronal cell bodies and is largely isotropic, are shown in Table 3.5. For gray matter, as for homogeneous brain tissue, it is accepted that the bulk modulus is 2.19 GPa. The shear modulus values in the literature range only from 10 to 34 kPa. Initially, Zhang used values one order of magnitude higher than those reported from porcine brain tissue experiments, in order to compensate

Source	ρ (kg/m^3)	K (Pa)	G (Pa)	E (Pa)	ν
Ruan (1994) [74]	1040	2.19×10^9	1.68×10^6		0.4996
Nishimoto (1998) [64]	1040	2.19×10^9	5.28×10^5		
Willinger (1999) [100]	1140	2.19×10^9	5.28×10^5	6.75×10^5	
Gilchrist (2001) [30]	1040			5.58×10^5	0.485
Willinger (2001) [98]	1040	1.125×10^9	4.90×10^4		
Willinger (2003) [97]	1040	1.125×10^9	4.90×10^4		
Takhounts (2003) [83]		5.6×10^8	1.03×10^4		
Belingardi (2005) [8]	1140	5.625×10^6	4.90×10^5		
Raul (2006) [73]	1040	1.125×10^9	4.90×10^4		
Gong (2008) [31]	1040	2.19×10^9	5.28×10^5		
Chafi (2010) [13]		2.19×10^9	4.0744×10^4		

Table 3.4: Brain Material Properties from the Literature

for the effect of vascular structures *in vivo* [103], and these values were adopted by Horgan [37]. Zhang later slightly selected slightly higher shear modulus values [105], which were adopted by Taylor [85]. In the current simulations, the bulk modulus was assumed to be 2.19 GPa, and the shear modulus value, 22.53 kPa, was derived from the values for E and ν provided by Dr. Moore; these values agree well with the material property values reported in the literature for gray matter. These material properties were also used for the eyes in the FHM.

Source	ρ (kg/m^3)	K (Pa)	G (Pa)
Zhang (2001) [103]	1060	2.19×10^9	1.0×10^4
Horgan (2004) [37]	1060	2.19×10^9	1.0×10^4
Zhang (2004) [105]	1040	2.19×10^9	3.4×10^4
Taylor (2009) [85]	1040	2.37×10^9	3.4×10^4

Table 3.5: Gray Matter Material Properties from the Literature

White matter, unlike gray matter, consists of axons surrounded by myelin sheaths. To account for the more fibrous nature of white matter, the shear modulus of white matter was assumed to be higher than the shear modulus of gray matter. In the literature, Zhang [103] and Horgan [37] assumed that the shear modulus of white matter was 25% higher than the shear modulus of gray matter. Later, Zhang assumed that the shear modulus of white matter was only 20% higher than that of gray matter [105], and Taylor adopted that value [85]. In our simulations, the bulk modulus was assumed to be 2.19 GPa, and the shear modulus, 28.16 kPa, was assumed to be 25%

higher than the shear modulus of gray matter; these material properties lie well within the range of values reported in the literature, as shown in Table 3.6. The material properties for the white matter were also used for the glia structure in the FHM.

Source	ρ (kg/m^3)	K (Pa)	G (Pa)
Zhang (2001) [103]	1060	2.19×10^9	1.25×10^4
Horgan (2004) [37]	1060	2.19×10^9	1.25×10^4
Zhang (2004) [105]	1040	2.19×10^9	4.1×10^4
Taylor (2009) [85]	1040	2.37×10^9	4.1×10^4

Table 3.6: White Matter Material Properties from the Literature

Venous Sinus

The venous structures in the FHM correspond to the dural venous sinuses, which are venous channels found between layers of dura mater in the brain. In the simulations, the venous structures were modeled as the blood flowing through the dural venous sinuses. The bulk modulus was the same as that for water, and the shear modulus was derived from the E and ν values provided by Dr. Moore. These properties describe a virtually incompressible fluid similar to the CSF.

Muscle

For the muscle, the bulk modulus was obtained from Kojic [43], and the shear modulus and density were obtained from Dr. Moore.

Skin/Fat

For the skin/fat, the bulk and shear modulus values were obtained from the E and ν values in the literature for scalp, which consists of skin and underlying fat and muscle. The Young's modulus and Poisson's ratio values in the literature were obtained from experimental data from Zhou and were adopted by Willinger, Belingardi, Raul, Ho, and Chafi [97, 8, 73, 33, 13].

Source	Type	ρ (kg/m^3)	E (Pa)	ν
Zhang (2001) [103]	Soft tissue	1100	1×10^6	0.45
Kleiven (2002) [42]	Scalp	1130	16.7×10^6	0.42
Willinger (2003) [97]	Scalp	1000	16.7×10^6	0.42
Belingardi(2005) [8]	Scalp	1200	16.7×10^6	0.42
Raul (2006) [73]	Scalp	1200	16.7×10^6	0.42
Ho (2007) [33]	Scalp	1130	16.7×10^6	0.42
Chafi (2010) [13]	Scalp	1200	16.7×10^6	0.42

Table 3.7: Skin-Related Material Properties from the Literature

Skull

The skull, which is considered a single structure in the FHM, is composed of two types of bone: cortical, or compact bone, and trabecular, or cancellous bone. While cortical bone, which forms the surface of bones, is hard and dense, trabecular bone, which forms the bulk of the interior of most bones, is spongy; Table 3.9, which lists some cortical bone material properties reported in the literature, and Table 3.10, which lists some trabecular bone material properties reported in the literature, demonstrate the differences between the material properties for cortical and trabecular bone. For cortical bone, values for the bulk modulus range from 4 to 8.62 GPa, and values for the shear modulus range from 2.4 to 6.15 GPa. For trabecular bone, values for the bulk modulus range from 0.47 to 3.4 GPa, and values for the shear modulus range from 0.215 to 2.32 GPa. For a skull consisting of both cortical and trabecular bone, some examples of material properties reported in the literature are given in Table 3.8. Values for the bulk modulus range from 3.96 to 7.12 GPa, and values for the shear modulus range from 2.73 to 3.47 GPa. In the FHM, the material properties for the skull, $\rho = 1412\,\text{kg/m}^3$, $K = 3.89 \times 10^9$ Pa, $G = 2.664 \times 10^9$ Pa, which were all obtained from Dr. David Moore, fall between the literature values for cortical and trabecular bone.

Source	ρ (kg/m^3)	K (Pa)	G (Pa)	E (Pa)	ν
Nishimoto (1998) [64]	1456	7.12×10^9	3.47×10^9	8.75×10^9	
Gilchrist (2001) [30]	1410			6.65×10^9	0.22
Taylor (2009) [85]	1412	4.82×10^9			0.22
Chafi (2010) [13]	1800			1.5×10^{10}	0.21

Table 3.8: Skull (Cortical and Trabecular Bone) Material Properties from the Literature

Source	ρ (kg/m^3)	K (Pa)	G (Pa)	E (Pa)	ν
Ruan (1994) [74]	3000	7.3×10^9	5.0×10^9		
Zhang (2001) [103]	2100			6.0×10^9	0.25
Kleiven (2002 [42]	2000			1.5×10^{10}	0.22
Horgan (2003) [36]	2000			1.5×10^{10}	0.22
Willinger (2003) [97]	1900	6.2×10^9		1.5×10^{10}	0.21
Belingardi (2005) [8]	1800			1.5×10^{10}	0.21
Raul (2006) [73]	1800			1.5×10^{10}	0.21
Ho (2007) [33]	2000			1.5×10^{10}	0.22
Gong (2008) [31]	3000	7.3×10^9			0.22

Table 3.9: Cortical Bone Material Properties from the Literature

Source	ρ (kg/m^3)	K (Pa)	G (Pa)	E (Pa)	ν
Ruan (1994) [74]	1750	3.4×10^9	2.32×10^9		0.22
Zhang (2001) [103]	1000			5.6×10^8	0.30
Kleiven (2002) [42]	1300			1.0×10^9	0.24
Horgan (2003) [36]	1300			1.0×10^9	0.24
Willinger (2003) [97]	1500	2.3×10^9		4.6×10^9	0.05
Belingardi (2005) [8]	1500			4.5×10^9	0.01
Raul (2006) [73]	1500			4.5×10^9	0.0
Ho (2007) [33]	1300			1.0×10^9	0.24
Gong (2008) [31]	1744	3.4×10^9			0.22

Table 3.10: Trabecular Bone Material Properties from the Literature

3.4 Summary

The DVBIC/MIT Full Head Model (FHM), a biofidelic model of the human head, was generated from high-resolution medical imaging data. The FHM consists of 11 distinct head structures: CSF, eyes, glia, ventricles, venous sinus, air sinus, muscle, skull, skin/fat, white matter, and gray matter. The material responses of the structures are modeled using the Tait and Hugoniot equations of state and a deviatoric elastic model. The material properties for each structure, which were derived from values provided by Dr. Moore and values found in the literature, all fall within the range of values reported in the literature. The FHM has been optimized for use in finite element simulations, and it can be used in blast simulations conducted in the VTF, a suite of computational solvers that allows simulation of complex fluid-structure interactions by coupling a Lagrangian finite element solid solver with an Eulerian fluid solver. This provides a suitable framework for modeling blast-related TBI.

Chapter 4

Full Head Simulations

4.1 Overview

In order to investigate the mechanical effects of blasts on the human head, simulations were conducted with the DVBIC/MIT FHM under three different conditions: (1) a blast with incident overpressure of 6 atm, equivalent to a free air explosion of 0.0836 kg TNT at 0.6 m standoff distance; (2) a blast with incident overpressure of 30 atm, equivalent to a free air explosion of 0.569 kg TNT at 0.6 m standoff distance; and (3) an impact between a head traveling at 5 m/s and a stationary boundary. The overpressures for the blast simulations were selected based on the Bowen curves, which estimate tolerance to a single blast at sea level for a 70-kg unarmored human oriented perpendicular to the blast [9]. For a blast with a positive overpressure duration of 0.5 ms, the Bowen curves estimate that threshold lung damage occurs at approximately 6 atm and 99% lethality occurs at approximately 30 atm [9]. The impact condition was selected to result in probable concussive injury based on comparable impact studies in the literature [105].

In the blast simulations, the fluid grid used two levels of subdivision with an equivalent resolution of 480x400x200 grid points in order to resolve the blast front and the fluid-solid interface with sufficient fidelity. To prevent the blast from engulfing the bottom of the head, where the neck would ordinarily be attached, the base of the head was constrained in all degrees of freedom. 8 processors were used for the fluid

solver and 22 were used for the solid solver. In the solid-only impact simulation, no constraints were placed on the base of the head, and 20 processors were used.

4.2 6 atm Blast Simulation

In the first simulation, the FHM was subjected to a blast with incident overpressure of 6 atm, the threshold for unarmored blast lung injury. Figure 4-1 illustrates the propagation of the blast wave through mid-coronal sections of the head. Here we adopt the fluid mechanics convention of positive pressure under compression. In the fluid, we consider the overpressure, the pressure above atmospheric pressure, and in the solid, we compute the pressure from the stresses using the relation $p = \frac{1}{3}\sigma_{kk}$. At t=0.1 ms, we can observe the blast wave impinging on the left temporal region of the head and transmitting stresses through the skull to the brain tissue. The snapshot at t=0.151 ms shows the wave propagating through the cranial cavity from left to right, and the snapshot at t=0.201 ms shows negative pressure appearing in the left frontal region as a result of the negative phase of the incident wave beginning to interact with the head. We can also observe at t=0.201 ms negative pressure beginning to build in the skull in the right temporal region. The transmitted stress waves reflect off the skull and into the intracranial cavity, resulting in a multiplicity of heterogeneous waves that interact in a complex manner. These complex interactions are captured by the snapshots at t=0.279, 0.338, 0.402, and 0.599 ms. In certain regions, such as the left temporal region, reflections from stress waves result in negative pressures. By 0.713 ms, the stresses in the intracranial cavity have largely dissipated, with the largest remaining stresses residing in the skull.

To develop a more quantitative understanding of the simulation results, we plot the pressure envelopes for each of the 11 distinct head structures. That is, for each structure, we extract and plot the highest pressure at each time step; the resultant curves are the envelopes of the pressure histories of all points within each structure. In addition to analyzing the pressure or volumetric component of the stress field, which is associated with volume changes in the tissue, we also consider the deviatoric stresses,

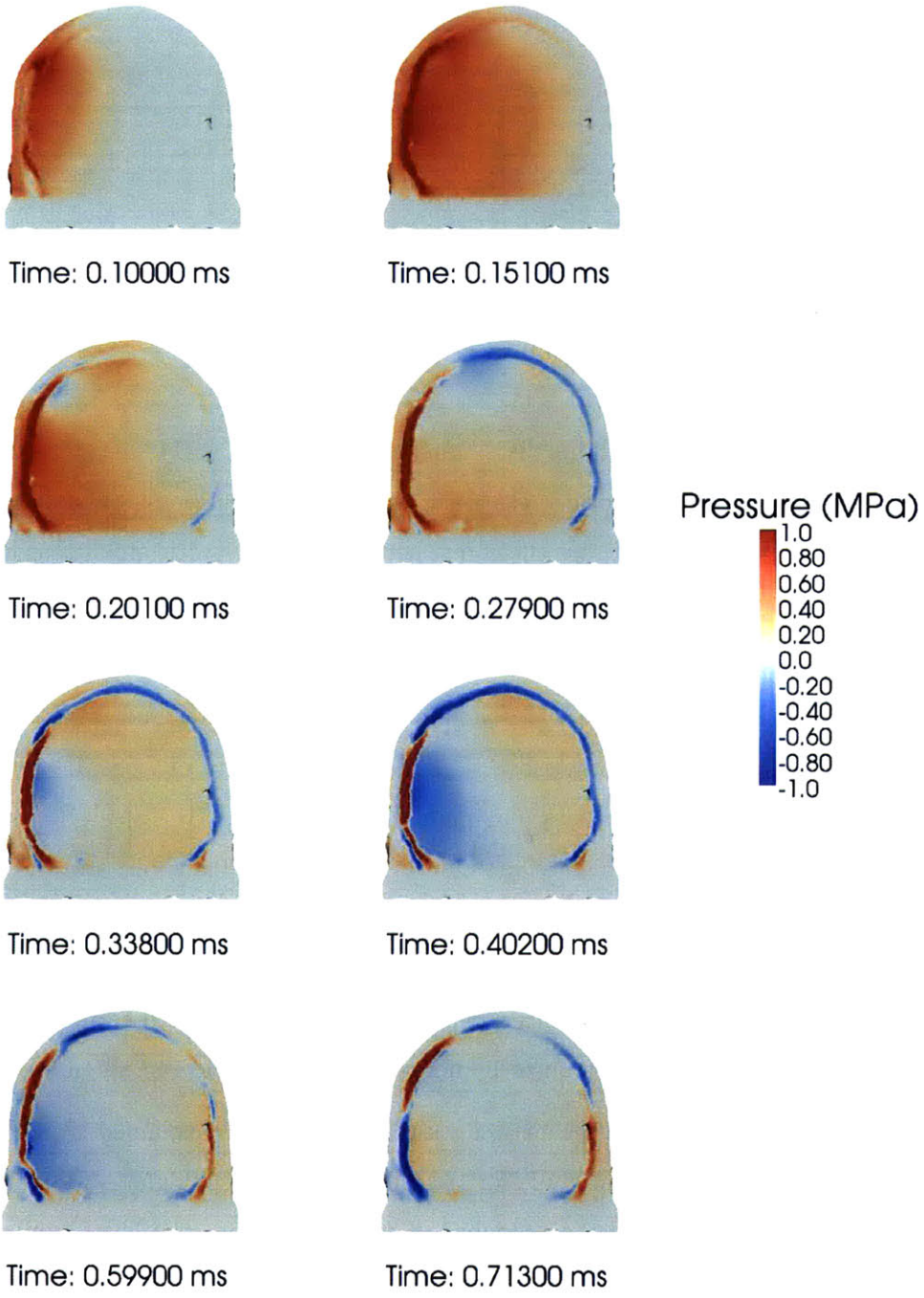

Figure 4-1: Snapshots of pressure from the 6 atm head blast simulation. The scale for the color bar is from -1.0 to 1.0 MPa

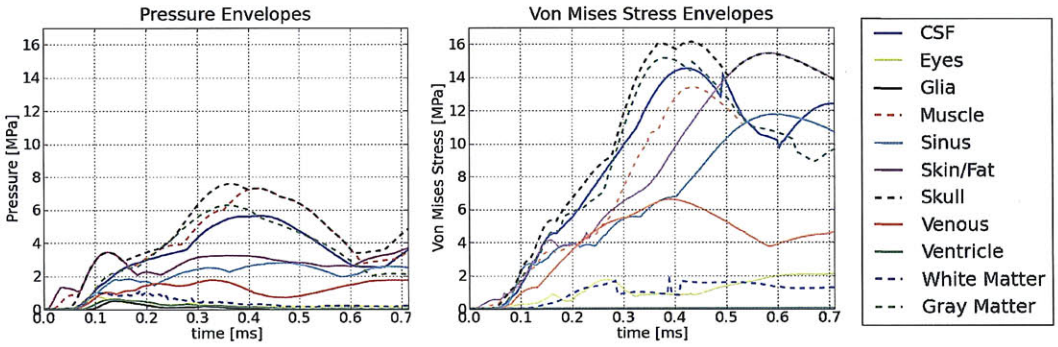

Figure 4-2: Pressure and Von Mises stress envelopes from the 6 atm head blast simulation. The scale is from 0 to 17 MPa.

which are related to isochoric distortions in the tissue. A scalar value representing the magnitude of the deviatoric stress is the Von Mises or equivalent stress $\sigma_e = \sqrt{\frac{3}{2} s_{ij} s_{ij}}$, where $s_{ij} = \sigma_{ij} - \frac{1}{3}\sigma_{kk}\delta_{ij}$ are the components of the deviatoric stress tensor [51]. The pressure and Von Mises stress envelopes for each structure are shown in Fig. 4-2.

From the pressure envelopes, we observe that the highest pressures were experienced by the skull and muscle, followed by the gray matter and subarachnoid CSF. In particular, the skull experienced a maximum pressure of 7.58 MPa at 0.366 ms, and the muscle experienced a maximum pressure of 7.29 MPa at 0.416 ms. The gray matter experienced its highest pressure of 6.26 MPa at 0.366 ms, and the CSF experienced its highest pressure of 5.62 MPa at 0.42 ms. In contrast, the highest pressure experienced by the white matter was 1.15 MPa at 0.187 ms. The eyes, glia, ventricles, and white matter all experienced peak pressures that occurred earlier than the peak pressures of other head structures and were particularly low in magnitude.

Some of the disparities between structures can be explained by differences in material properties; the skull, for example, experienced higher stresses due to its higher stiffness. However, a number of other structures that had similar material properties to each other, such as gray and white matter, experienced widely disparate maximum pressures, highlighting the importance of the complex geometry of the head in producing nonuniform pressure fields that affect each structure in distinct ways. For example, from the snapshots of pressure, we can qualitatively see that

the highest pressures were produced in the left temporal region and that reflection of the stress waves resulted in significant magnification of pressure. From the pressure envelopes, we can determine that the highest pressure experienced by the head was 7.58 MPa, which is 12.6 times greater than the incident overpressure of 0.6 MPa. The pressure envelopes also suggest that for some structures, such as the white matter and ventricles, the highest pressures experienced were due to the initial transmitted wave, while for other structures that experienced much larger peak pressures that occurred later, such as the skull, muscle, and gray matter, the highest pressures experienced were due to reflected waves and interactions between the transmitted and reflected waves. In addition, the pressure envelopes demonstrate that blasts can lead to elevated pressures on very short time scales; peak pressures for the various structures typically occurred around 0.4 ms or earlier.

From the Von Mises stress envelopes, we first observe that the magnitudes of the maximum shear stresses are approximately twice as high as the magnitudes of the maximum pressures. The skull experienced the highest Von Mises stresses, followed by the skin/fat, gray matter, CSF, and muscle. The peak Von Mises stress experienced by the skull was 16.1 MPa at 0.434 ms, the peak Von Mises stress experienced by the skin/fat was 15.4 MPa at 0.581 ms, and the peak Von Mises stress experienced by the gray matter was 15.2 MPa at 0.379 ms. The CSF experienced its highest Von Mises stress of 14.5 MPa at 0.420 ms, and the muscle experienced its highest Von Mises stress of 13.4 MPa at 0.434 ms. The highest Von Mises stress experienced by the white matter, on the other hand, was only 1.73 MPa at 0.388 ms; again, head structures with very similar material properties experienced vastly different maximum shear stresses. The peak Von Mises stresses typically occurred around 0.4 ms, although the skin/fat and air sinuses experienced delayed peak stresses around 0.6 ms.

4.3 30 atm Blast Simulation

In the second simulation, the FHM was subjected to a blast with incident overpressure of 30 atm, the threshold for 99% lethality due to unarmored blast lung injury.

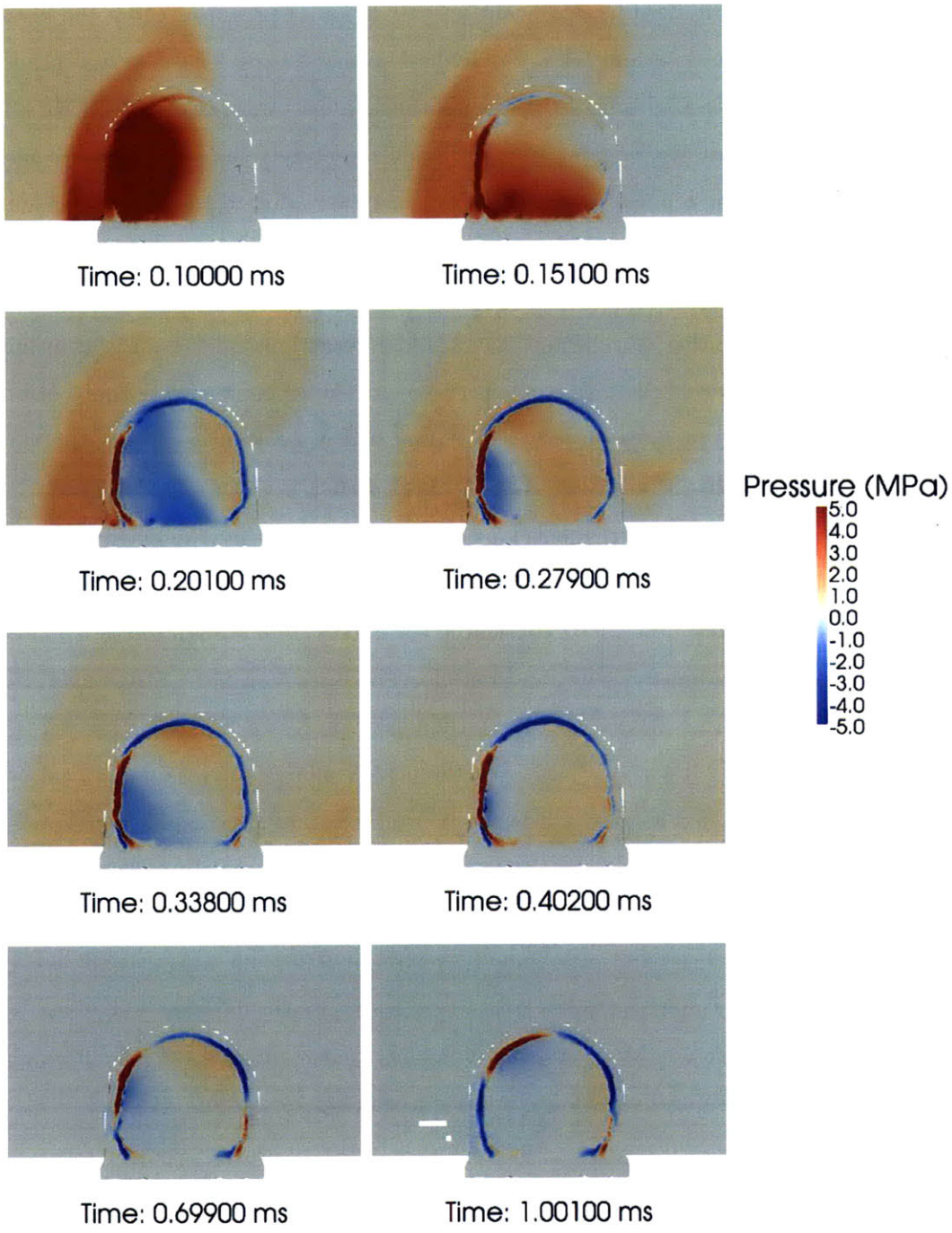

Figure 4-3: Snapshots of pressure from the 30 atm head blast simulation. The scale for the color bar is from -5.0 to 5.0 MPa

Fig. 4-3 illustrates the propagation of the 30 atm blast wave through the head. The magnitudes of the pressures observed in the 30 atm blast simulation are clearly higher than those observed in the 6 atm blast simulation, but the pressure distributions are largely similar, though the 30 atm blast wave does propagate more rapidly through the head. By t=0.1 ms, the blast wave has arrived at the head and propagated halfway through the cranial cavity, and by t=0.151 ms, the blast wave has fully propagated through the cranial cavity. At t=0.151 ms, we begin to see negative pressure, and by t=0.201 ms, substantial regions of negative pressure have formed within the cranial cavity. The transmitted stress waves reflect off the skull, and the snapshots at t=0.279, 0.338, 0.402, and 0.699 ms display fluctuations in the intracranial pressure field due to the multiplicity of waves within the cranial cavity. By 0.4 ms, the blast in the surrounding fluid has largely dissipated, and by 0.699 ms, it has entirely dissipated. By 1.0 ms, although there continue to be regions of positive and negative pressure in the cerebral tissue near the skull, most of the remaining stresses reside in the skull.

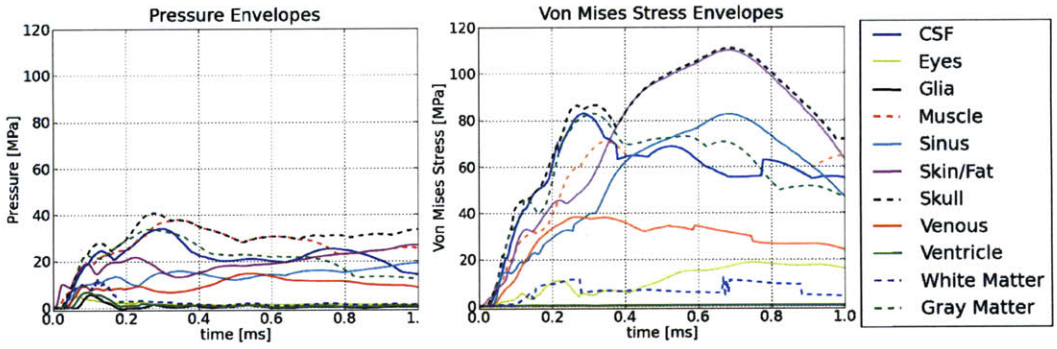

Figure 4-4: Pressure and Von Mises stress envelopes from the 30 atm head blast simulation. The scale is from 0 to 120 MPa.

Fig. 4-4 shows the pressure and Von Mises stress envelopes from the 30 atm blast simulation. As in the 6 atm blast simulation, the skull experienced the highest pressure, this time with a pressure of 40.7 MPa at 0.279 ms. The skull was closely followed by muscle, which experienced a peak pressure of 37.7 MPa at 0.343 ms, gray matter, which experienced a peak pressure of 33.5 MPa at 0.26 ms, and CSF, which experi-

enced a peak pressure of 33.9 MPa at 0.292 ms. The skin/fat experienced its highest pressure of 26.6 MPa at 1.01 ms, and the air sinuses experienced their highest pressure of 18.8 MPa also at 1.01 ms. In contrast, the maximum pressure experienced by the white matter was 12.7 MPa at 0.119 ms. We again observe significant amplification of the original blast wave, with pressures in the head reaching 40.7 MPa, or 13.6 times the original 3 MPa incident overpressure. We also again observe that for some structures, such as the white matter, effects from the initial blast wave predominate, while for other structures such as the skull and gray matter, effects from the reflected waves and the complex interactions between the reflected and transmitted waves predominate, resulting in markedly higher peak pressures that occur at later times. As in the 6 atm blast simulation, the nodes that experienced the highest pressures were located in the left temporal region of the head. The maximum pressures experienced by each structure in the 30 atm blast simulation were typically 5-6 times higher than the maximum pressures experienced in the 6 atm blast simulation, suggesting that for most structures, the pressure magnitudes scale in a predominantly linear fashion. The pressure time course for most of the structures appears to have been slightly shifted compared to the 6 atm blast simulation, with peak pressures occurring about 0.1 ms earlier in the 30 atm simulation than in the 6 atm simulation.

As in the 6 atm simulation, the magnitudes of the maximum Von Mises stresses are approximately 2-3 times higher than the magnitudes of the maximum pressures. Here the highest Von Mises stresses were experienced by the skull, skin/fat, CSF, gray matter, air sinuses, and muscle. The skull experienced a peak Von Mises stress of 110.7 MPa at 0.685 ms, the skin/fat experienced a peak Von Mises stress of 109.7 MPa at 0.681 ms, and the CSF experienced a peak Von Mises stress of 82.8 MPa at 0.288 ms. The maximum Von Mises stress experienced by the gray matter was 82.6 MPa at 0.311 ms, and the maximum Von Mises stress experienced by the air sinuses and muscle was 82.3 MPa at 0.681 ms. The peak Von Mises stress experienced by the white matter, meanwhile, was 11.4 MPa at 0.274 ms. The peak Von Mises stress experienced by each structure was typically 6-7 times greater than the peak Von Mises stress experienced in the 6 atm blast simulation. Unlike the pressure peaks, which

occurred earlier in the 30 atm blast simulation than in the 6 atm blast simulation, the peak Von Mises stresses for the skull and skin/fat, which experienced the highest overall Von Mises stresses, occurred 0.1-0.2 ms later in the 30 atm simulation than in the 6 atm simulation.

4.4 5 m/s Impact Simulation

In the third simulation, the FHM was subjected to a 5 m/s lateral impact. The site of impact was the left temporal region of the head. Fig. 4-5 illustrates the propagation of stress waves through mid-coronal sections of the head in the 5 m/s impact simulation. Starting at t=0.102 ms, we can see stress waves propagating from left to right. The snapshots at t=0.150, 0.201, and 0.279 ms show the wave propagation and the buildup of positive pressure at the coup site, in the left temporal region. At t=0.337 and 0.402, we observe the concentration of pressure in the skull and muscle along the left temporal and inferior surfaces of the skull. By t=0.599 and 0.807 ms, we can see the increasing concentration of positive pressure in the skull and muscle and also the the growth of a negative pressure region on the right side of the cranial cavity at the contrecoup site. These snapshots illustrate classic coup and contrecoup behavior, which has been suggested as a mechanism for cerebral contusion [105].

Fig. 4-6 shows the pressure and Von Mises stress envelopes for the head impact simulation. In contrast to the pressure envelopes from the 6 atm and 30 atm blast simulations, which feature distinct peaks early in the simulations, the pressure envelopes from the impact simulation increase monotonically. In the impact simulation, the maximum pressure of 20.98 MPa was experienced by the skull and gray matter, and the muscle, CSF, skin/fat, and air sinuses experienced peak pressures of 20.66 MPa, 16.22 MPa, 15.37 MPa, and 12.4 MPa respectively, all at 0.807 ms. The maximum pressure experienced by the white matter was 1.045 MPa at 0.296 ms. As in the blast simulations, the nodes that experienced the highest pressures were located in the left temporal region of the head. In general, the maximum pressure experienced

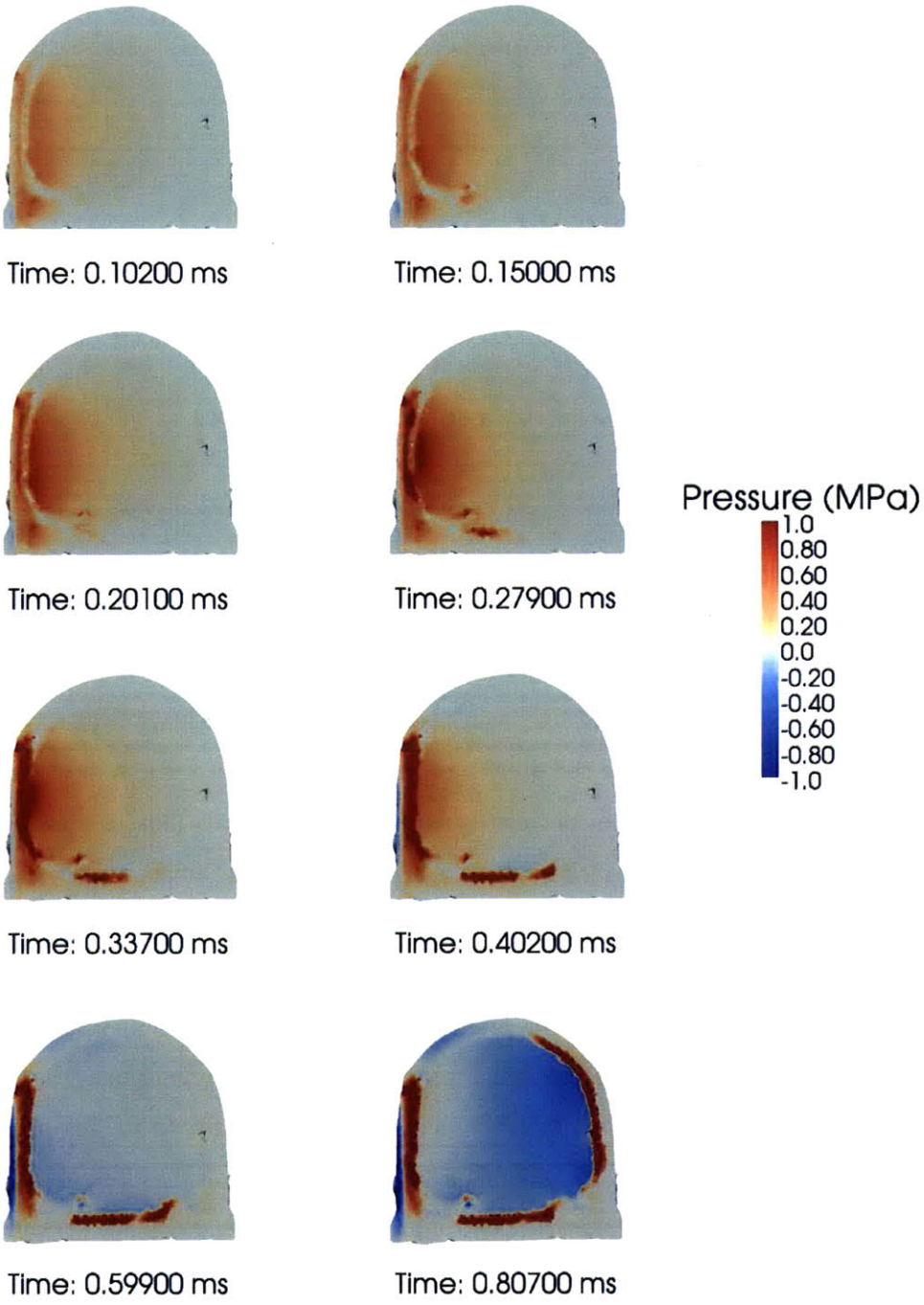

Figure 4-5: Snapshots of pressure from the 5 m/s head impact simulation. The scale for the color bar is from -1.0 to 1.0 MPa.

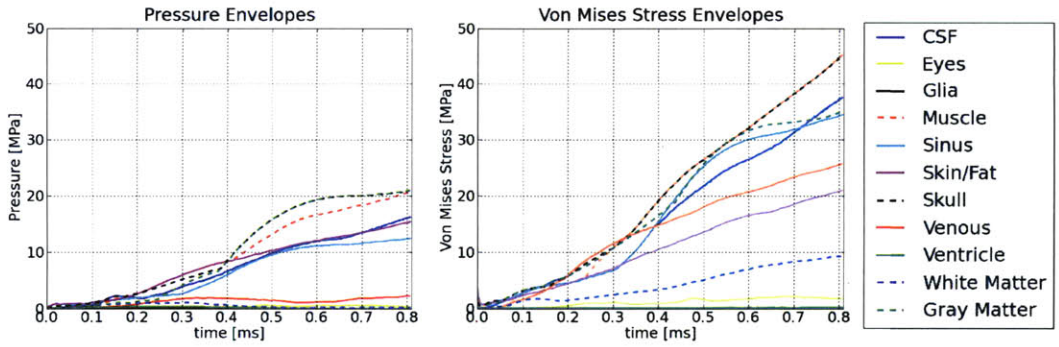

Figure 4-6: Pressure and Von Mises stress envelopes from the 5 m/s head impact simulation. The scale is from 0 to 50 MPa.

by each structure was 2-3 times greater than the maximum pressure experienced by the same structure in the 6 atm blast simulation, but 1.5-2 times smaller than the maximum pressure experienced by the same structure in the 30 atm blast simulation. This suggests that a blast with an incident overpressure of 30 atm could plausibly cause brain injury.

The Von Mises stress envelopes, like the pressure envelopes, also show monotonic growth, with the highest Von Mises stresses occurring at 0.807 ms. The highest Von Mises stress, 45.28 MPa, was experienced by the skull and muscle. The CSF, gray matter, air sinuses, venous sinuses, and skin/fat experienced peak Von Mises stresses of 37.49 MPa, 35.1 MPa, 34.45 MPa, 25.57 MPa, and 20.97 MPa respectively. While the venous sinuses experienced low peak Von Mises stresses in the blast simulations compared to other head structures, they experienced relatively high peak Von Mises stresses in the impact simulation. The maximum Von Mises stress experienced by the white matter was 9.36 MPa at 0.807 ms. Like the maximum pressures, the maximum Von Mises stresses were typically 2-3 times greater than the stresses in the 6 atm blast simulation and 2-3 times lower than the stresses in the 30 atm blast simulation, again supporting the plausibility of blast-induced brain injury.

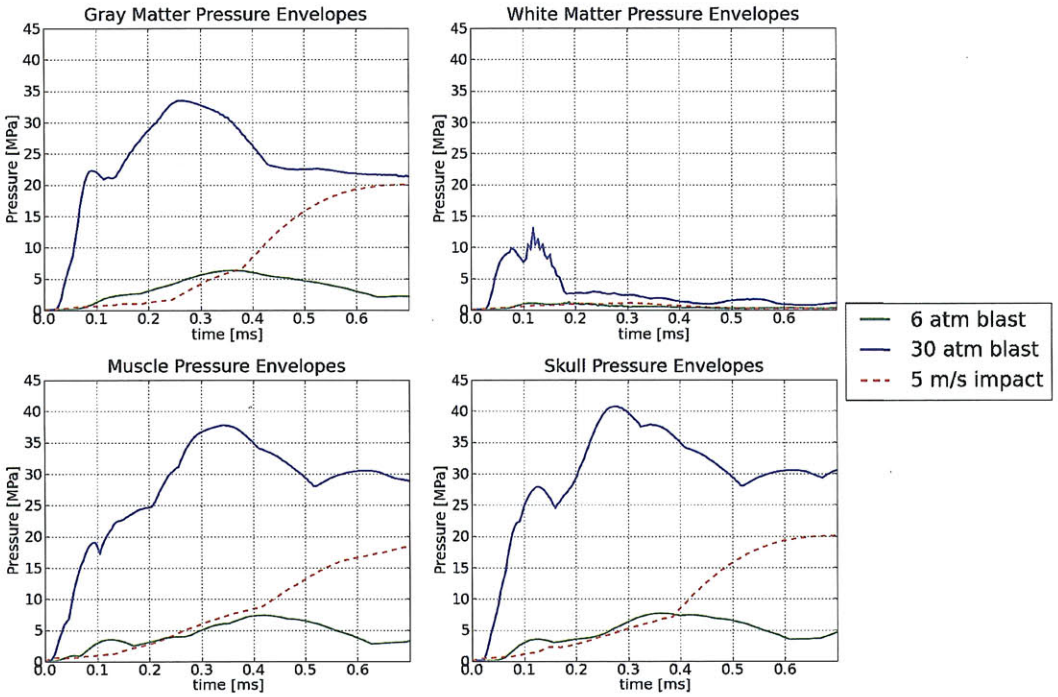

Figure 4-7: Comparison of pressure envelopes from the 6 atm, 30 atm, and 5 m/s impact head simulations for gray matter, white matter, muscle, and skull.

4.5 Comparison of Blast and Impact Simulations

To more directly compare the results from the blast and impact simulations, Fig. 4-7 compares pressure envelopes from the 6 atm, 30 atm, and impact simulations for four materials of interest: gray matter, white matter, muscle, and skull. From Fig. 4-7, we observe that of the three simulations, the 30 atm blast simulation produces by far the highest pressures at the earliest times. We also observe that the pressure envelopes for white matter are of much lower magnitude than the pressure envelopes for the other structures, likely because it does not share boundaries with structures such as the CSF or skull.

To gain understanding of the pressures being experienced by individual points within the head, pressure histories were extracted at selected points in the mid-coronal plane for each of the three simulations. Fig. 4-8 compares the pressure histories from the 6 atm, 30 atm, and head impact simulations for each of the seven locations labeled as points A, B, C, D, E, F, and G in the figure. Points A, B, and C are located in the left side of the cranial cavity; point A is in the gray matter, point B is in the white matter, and point C is in the skull. Point D is located in the center of the cranial cavity in the white matter. Points E, F, and G are located in the right side of the cranial cavity; point E is in the skull, point F is in the white matter, and point G is in the gray matter.

At all the points, the pressure histories demonstrate even more dramatically than the pressure envelopes that the 30 atm blast simulation results in peak pressures that occur earlier and are significantly greater in magnitude than the peak pressures from the 6 atm blast and head impact simulations. For example, at point A, located in the gray matter, the peak pressure produced in the 30 atm simulation was 5.76 MPa and occurred at 0.105 ms, compared to a peak pressure of 0.538 MPa at 0.169 ms in the 6 atm simulation and a peak pressure of 0.333 MPa at 0.243 ms in the head impact simulation. At this point, the peak pressure produced in the 30 atm simulation was 10.7 times greater than the peak pressure from the 6 atm simulation and 17.3 times greater than the peak pressure from the impact simulation. The peak pressure also

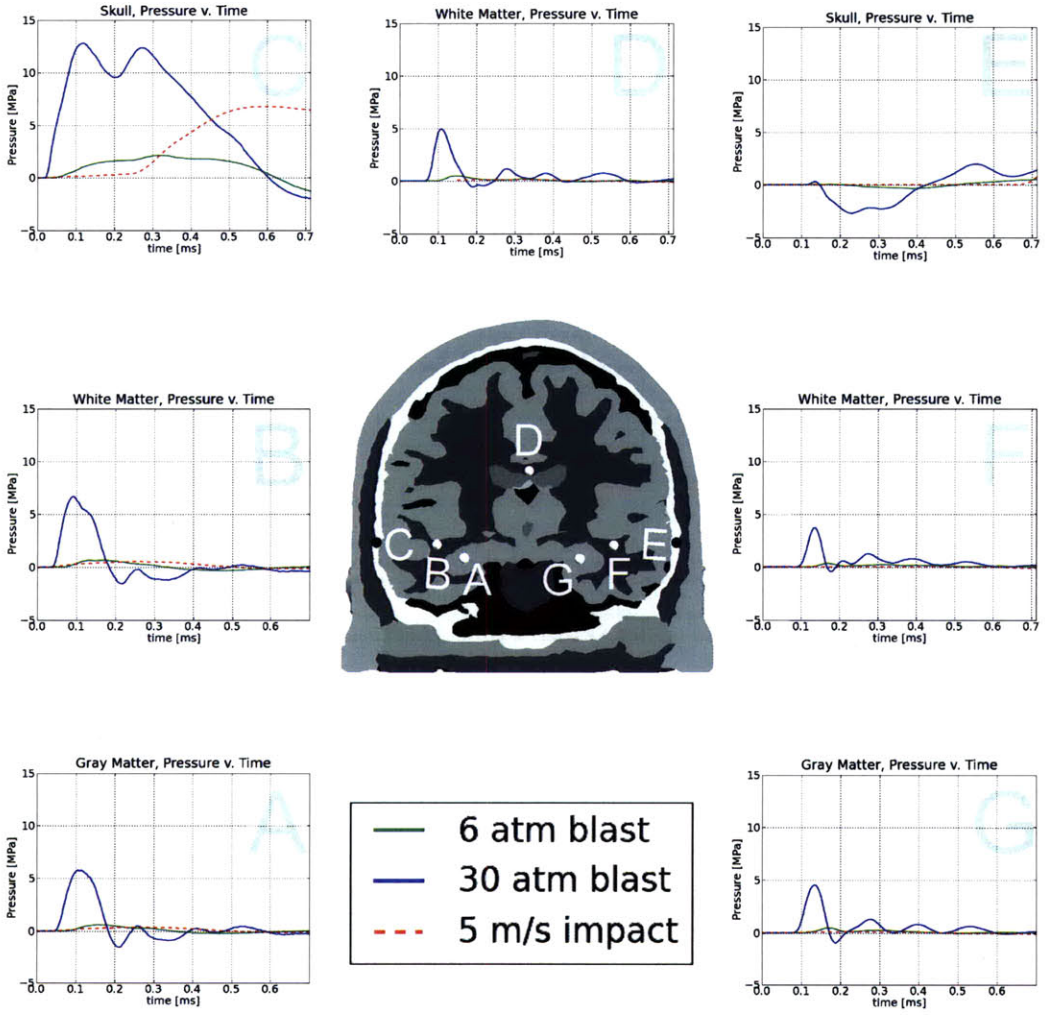

Figure 4-8: Pressure histories from the 6 atm, 30 atm, and 5 m/s impact head simulations at points located in the mid-coronal plane.

occurred 0.064 ms earlier in the 30 atm simulation than in the 6 atm simulation and 0.138 ms earlier than in the impact simulation.

At point C, located in the skull, the 30 atm simulation produced a peak pressure of 12.78 MPa at 0.119 ms, whereas the 6 atm simulation produced a peak pressure of 2.1 MPa at 0.315 ms and the impact simulation produced a peak pressure of 6.79 MPa at 0.601 ms. This time, the disparities are less dramatic; the peak pressure in the 30 atm simulation is 1.88 times greater than the pressure in the impact simulation and 6.09 times greater than the pressure in the 6 atm simulation. The impulse in the 30 atm simulation is also substantially greater than the impulse in the 6 atm and impact simulations.

At point F, located in the white matter, the 30 atm simulation produced a peak pressure of 3.68 MPa at 0.137 ms, while the 6 atm simulation produced a peak pressure of 0.30 MPa at 0.169 ms and the impact simulation produced a peak pressure of 0.053 MPa at 0.205 ms. Again, the differences in peak pressure magnitude are staggering; the 30 atm peak pressure is 12.27 times greater than the 6 atm peak pressure and 69 times greater than the impact peak pressure.

These results illustrate that in all three simulations, points within the skull experienced pressures that were much higher than the pressures experienced by the gray and white matter; this is expected due to the skull's higher stiffness. Within the cranial cavity, pressures are slightly higher for points in the left side, closer to the site of blast arrival or impact, than for points in the right side. For those points located near each other in gray and white matter, the pressure histories appear to be very similar. Comparing the three simulations, we see that the pressures produced by the 30 atm blast simulation are substantially higher — in some cases, even 69 times higher — than the pressures produced by the 6 atm blast and impact simulations. The pressure peaks also occur somewhat earlier in the 30 atm blast simulation than in the 6 atm and impact simulations; the 30 atm simulation tends to produce a positive pressure peak around 0.1 ms, followed by slight negative pressure and often some oscillations, while the 6 atm simulation tends to result in peaks around 0.2 ms, and the impact simulation tends to result in peaks around 0.2-0.3 ms. One interesting observation

is that for points in the gray and white matter, the pressures from the 6 atm blast simulation exceed the pressures from the impact simulation by up to 5.66 times. This has important implications, since TBI generally results from injury to the gray and white matter; these results suggest that even a 6 atm blast can cause pressures in the gray and white matter that exceed the pressures caused by an impact known to result in concussive injury. In sum, these results support the plausibility of 30 atm and even 6 atm blasts resulting in brain injury.

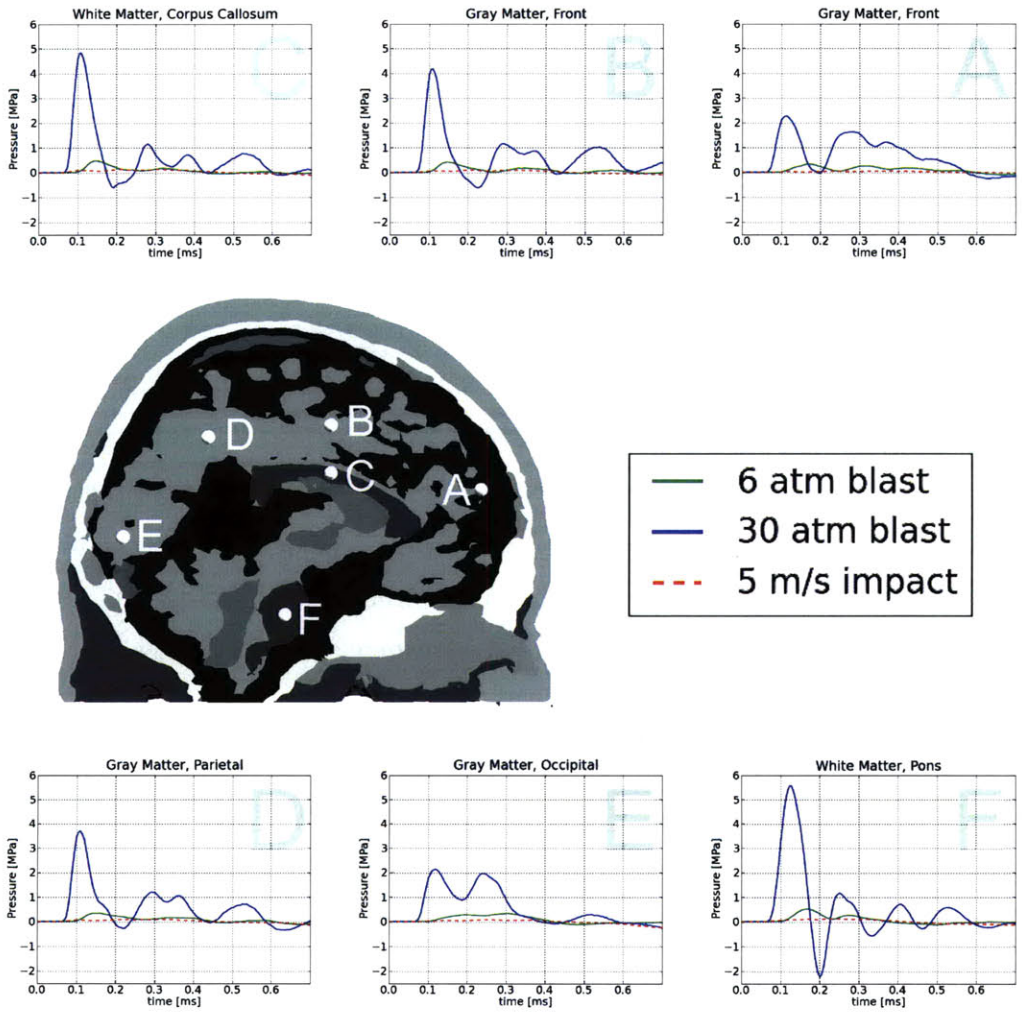

Figure 4-9: Pressure histories from the 6 atm, 30 atm, and 5 m/s impact head simulations at points located in the mid-sagittal plane.

For further comparison, pressure histories were extracted at selected points in the

mid-sagittal plane for each of the three simulations. Fig. 4-9 compares the pressure histories from the 6 atm, 30 atm, and impact simulations for each of the six locations labeled as A, B, C, D, E, and F in the figure. Points A and B are located in the frontal lobe, point C is in the corpus callosum, point D is in the parietal lobe, point E is in the occipital lobe, and point F is in the pons. Points A, B, D, and E are in the gray matter, while points C and F are in the white matter.

We again observe much higher pressures in the 30 atm simulation than in the 6 atm and impact simulations. For example, while point B in the frontal lobe experienced an initial peak pressure of 4.18 MPa at 0.109 ms in the 30 atm simulation, it experienced an initial peak pressure of only 0.407 MPa at 0.146 ms in the 6 atm simulation and an initial peak pressure of 0.086 MPa at 0.206 ms in the impact simulation. Similarly, point F in the pons experienced an initial peak pressure of 5.57 MPa at 0.123 ms in the 30 atm simulation, 0.499 MPa at 0.169 ms in the 6 atm simulation, and 0.115 MPa at 0.238 ms in the impact simulation. At the remaining points, too, the pressures in the 30 atm simulation dwarf those from the 6 atm and impact simulations, and further, the pressures generated in the 6 atm simulation are higher than those generated in the impact simulation. These results suggest that in critical locations in the brain, such as the prefrontal cortex, corpus callosum, and brainstem, blasts — even 6 atm blasts — may produce higher pressures than impacts at shorter time scales. This strongly suggests that blasts may lead to traumatic brain injury.

4.6 Discussion

The results presented in this chapter suggest that blasts may lead to traumatic brain injury. Snapshots of pressure contours from the blast simulations demonstrate that blast waves can transmit stress waves that propagate through the skull and into the intracranial cavity, resulting in elevated pressures in the brain tissue. The snapshots also show that the highest pressures are generated in the left temporal region, near the site of blast arrival, and that reflection of the stress waves and interaction between the various transmitted and reflected waves result in significant magnification of pressure.

Pressure envelopes from the blast simulations suggest that for some structures, such as the white matter, the peak pressures experienced were primarily due to the initial transmitted waves, while for other structures that experienced much larger peak pressures that occurred later, such as the skull, muscle, and gray matter, the peak pressures experienced were due to wave reflections and interactions between the various transmitted and reflected waves. In addition, the pressure and Von Mises stress envelopes demonstrate that blasts lead to elevated intracranial pressures and shear stresses on very short time scales, with peak pressures and stresses often occurring at or before 0.4 ms.

Comparison of pressure envelopes from the three simulations shows that the 30 atm blast simulation produced peak pressures that are significantly higher than the peak pressures produced by the impact simulation; this suggests, if peak intracranial pressure is an important indicator of traumatic brain injury, that a 30 atm blast could plausibly lead to brain injury. Plots of pressure histories at selected points in the mid-coronal and mid-sagittal planes of the head demonstrate even more clearly that the 30 atm blast simulation results in peak pressures that occur earlier and are significantly greater in magnitude than the peak pressures generated by the 6 atm blast and head impact simulations. Intriguingly, the pressure histories also demonstrate that at critical locations in the brain, such as the corpus callosum, frontal lobe, and brainstem, the 6 atm blast can result in higher pressures than the 5 m/s impact, suggesting that even a 6 atm blast could cause significant brain injury. In sum, these results suggest that blasts, even with overpressures as low as 6 atm, could plausibly cause traumatic brain injury.

Chapter 5

Helmet Simulations

5.1 Overview

In order to investigate the effect of the Advanced Combat Helmet (ACH) on the mechanical response of the human head to blast waves, the DVBIC/MIT Full Head Model (FHM) was extended to include the ACH, and two simulations were conducted with the extended FHM. In the first simulation, the extended FHM was subjected to a blast with incident overpressure of 30 atm, which is equivalent to a free air explosion of 0.569 kg TNT at 0.6 m standoff distance. As mentioned in Chapter 4, the Bowen curves estimate that an overpressure of 30 atm results in 99% lethality due to unarmored lung injury [9]. In the second simulation, the extended FHM was subjected to a 5 m/s lateral impact with a stationary boundary; the impact velocity was selected to result in probable concussive injury [105]. Results from these simulations were compared with results from identical simulations conducted with the original FHM that were described in the previous chapter. In the blast simulation, the fluid grid used two levels of subdivision with an equivalent resolution of 480x400x200 grid points, and the base of the head was constrained in all directions. 8 processors for the fluid and 22 processors for the solid were used. In the solid-only impact simulation, the base of the head remained unconstrained, and 20 processors were used.

5.2 Head-Helmet Model

A computational model of the ACH was developed from a CAD model of the actual shell, which was provided by the Natick Soldier Research, Development, and Engineering Center [16]. The CAD model was imported into Ansys ICEM CFD, and geometries of pads in the standard configuration were constructed and added to the model of the shell. An unstructured finite element mesh of the helmet and padding was then constructed using the Delaunay tetrahedral mesh generation algorithm, and the meshes of the helmet and padding were added to the DVBIC/MIT FHM to create a computational mesh of the head-helmet system. The head-helmet mesh, which consists of 922,852 tetrahedral elements, is shown in Fig. 5-1.

(a) FHM with ACH padding (b) FHM with ACH shell

Figure 5-1: Computational head-helmet mesh.

5.2.1 Material Model and Properties

To model the elastic response of the helmet and padding, we used the neo-Hookean model extended to the compressible range, in which the strain energy density is given by:

$$W(\mathbf{C}) = \frac{\lambda}{2}\log^2 J - \mu \log J + \frac{\mu}{2}(I_1 - 3) \tag{5.1}$$

where μ and λ are Lamé constants and I_1 is the first invariant of the right Cauchy-Green deformation tensor $\mathbf{C}$.

Standard material properties for Kevlar, which are shown in Table 5.1, were used

Material	Density (kg/m^3)	E (Pa)	ν
Helmet/Padding	1440	1.24e9	0.36

Table 5.1: Material Properties for Helmet and Padding

for both the helmet and the padding. Ideally an energy-absorbing material model and less stiff material properties would be used to model the foam padding, but as a first approximation, simulations using the neo-Hookean model and Kevlar material properties for the foam padding demonstrate the upper limit for stresses imparted to the head through the padding.

5.3 30 atm Blast Simulation

The extended FHM was first subjected to a blast with incident overpressure of 30 atm, the threshold for 99% lethality due to unarmored blast lung injury. Fig. 5-2 shows the propagation of the 30 atm blast wave through the fluid and solid domains. To better illustrate the propagation of the blast wave through the helmet and skull into the cranial cavity, Fig. 5-3 shows mid-coronal sections of the head-helmet model. At t=0.05 ms, we observe the blast wave impinging on the helmet. Due to the open nature of the helmet, the helmet slightly delays but does not prevent the blast wave from arriving at the head and directly transmitting stresses to the left temporal region of the head. At t=0.100, 0.123, and 0.151 ms, we observe the pressure wave propagating laterally from left to right through the cranial cavity and also through the padding. At t=0.196 and 0.279 ms, we see the wave continuing to propagate. We also observe fluctuations in pressure as waves reflect off the skull and interact with each other, as well as concentrations of pressure building in the skull. By t=0.320, a negative pressure region has started forming on the left side of the cranial cavity, and by t=0.379 ms, the largest remaining stresses are located in the skull.

To compare results from this helmet simulation with the results from the corresponding head simulation, Fig. 5-4 shows the pressure envelopes for the various structures from the head and helmet 30 atm blast simulations; for each structure, the maximum pressure at each time step is plotted. From Fig. 5-4, we can see that

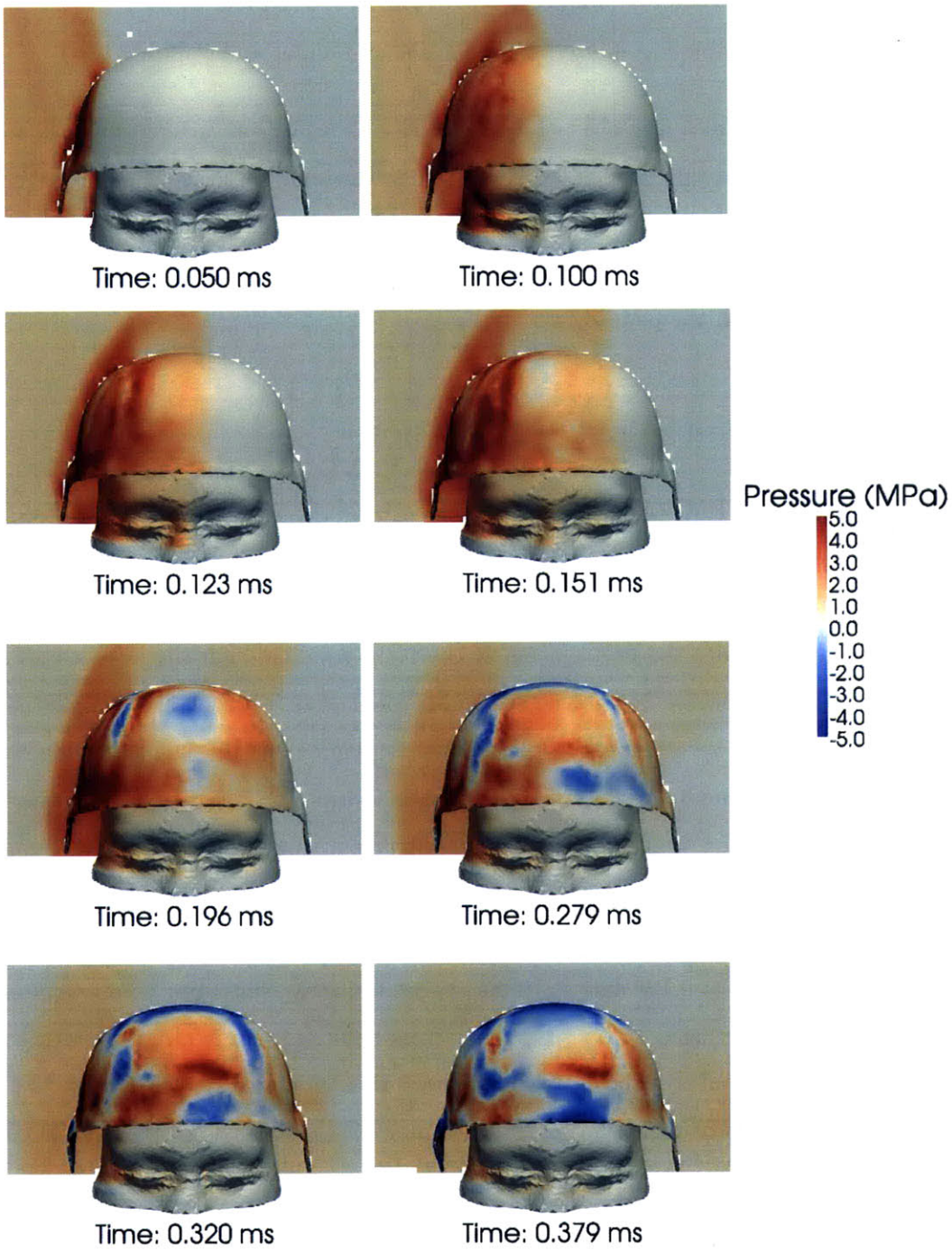

Figure 5-2: Snapshots of pressure from the 30 atm helmet blast simulation. The scale for the color bar is from -5.0 to 5.0 MPa.

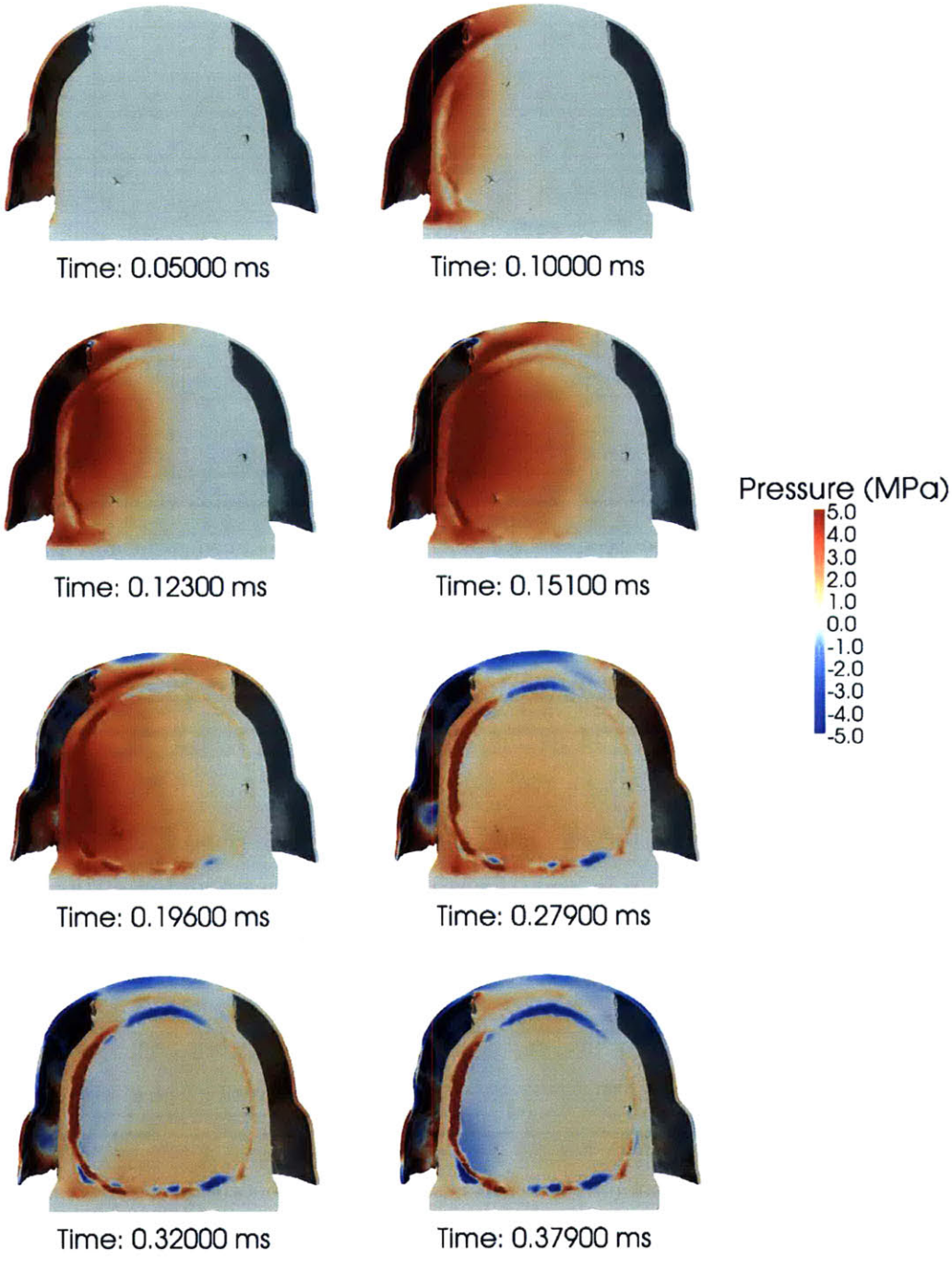

Figure 5-3: Pressure contours from the 30 atm helmet blast simulation in mid-coronal sections of the head. The scale for the color bar is from -5.0 to 5.0 MPa.

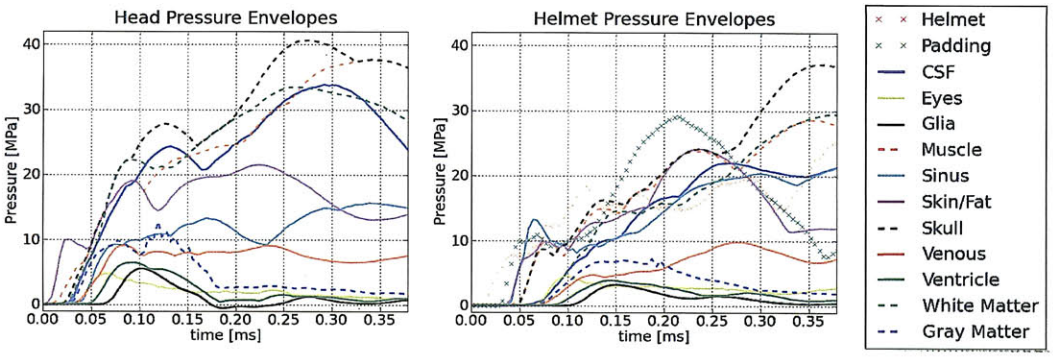

Figure 5-4: Pressure envelopes from the head and helmet 30 atm blast simulations. The scale is from -1 to 41 MPa.

the helmet slightly mitigates the effects of blast waves on the head, briefly delaying and slightly reducing the magnitude of peak pressures experienced. For example, the maximum pressure experienced by the skull was reduced from 40.7 MPa in the head simulation to 37.2 MPa in the helmet simulation and delayed from 0.279 ms in the head simulation to 0.361 ms in the helmet simulation. Similarly, the maximum pressure experiened by the muscle was reduced from 37.7 to 28.6 MPa and delayed from 0.343 to 0.356 ms, and the maximum pressure experienced by the gray matter was reduced from 33.5 to 29.4 MPa and delayed from 0.26 to 0.375 ms. For the white matter, the maximum pressure experienced was reduced from 12.7 to 7.2 MPa and delayed from 0.119 to 0.187 ms. Thus, we can see that addition of the ACH and padding to the FHM results in modest reductions in peak pressure magnitude and slight delays in peak pressure arrival time.

We next evaluate the effect of the helmet on the deviatoric response of the head; Fig. 5-5 shows the Von Mises stress envelopes for the various head structures from the head and helmet blast simulations. From Fig. 5-5, we can see that the effect of the helmet on the maximum Von Mises stresses experienced by the head in the time frame of the helmet simulation is ambiguous. For some structures, such as the gray matter, the peak Von Mises stresses were significantly reduced from 82.6 MPa in the head simulation to 62 MPa in the helmet simulation and delayed from 0.311 to 0.379 ms. For other structures, the effect was much less dramatic; for example, the peak

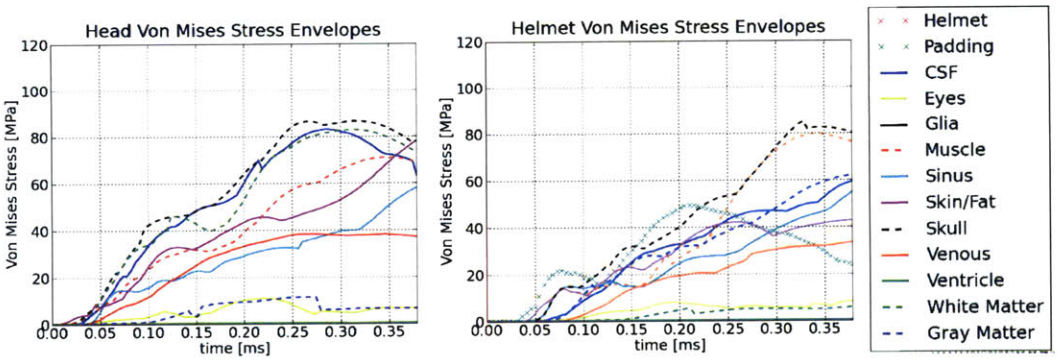

Figure 5-5: Von Mises stress envelopes from the head and helmet 30 atm blast simulations. The scale is from 0 to 120 MPa.

Von Mises stress experienced by the skull was reduced from 86.37 to 84.9 MPa and delayed from 0.320 to 0.329 ms. For still other structures, the peak Von Mises stress increased in the helmet simulation. For the muscle, for example, the peak Von Mises stress increased from 70.8 MPa in the head simulation to 79.43 MPa in the helmet simulation and arrived earlier in the helmet simulation, at 0.343 ms, than in the head simulation, at 0.347 ms. Thus, it is not clear that addition of the ACH mitigates shear stresses resulting from blast waves.

To more clearly observe the effect of the helmet on pressures within the head, we compare the pressure histories at selected points located in the mid-coronal plane. Fig. 5-6 shows pressure histories from the head and helmet simulations at each of the seven locations labeled as points A, B, C, D, E, F, and G in the figure. Points A, B, and C are located in the left side of the cranial cavity; point A is in the gray matter, point B is in the white matter, and point C is in the skull. Point D is located in the center of the cranial cavity in the white matter. Points E, F, and G are located in the right side of the cranial cavity; point E is in the skull, point F is in the white matter, and point G is in the gray matter.

It is clear from Fig. 5-6 that at each of the points, the pressure peaks experienced in the helmet simulations are somewhat lower in magnitude and delayed in time compared to the pressure peaks experienced in the head simulations. For example, at point A, which is located in the gray matter on the left side of the cranial cavity, the

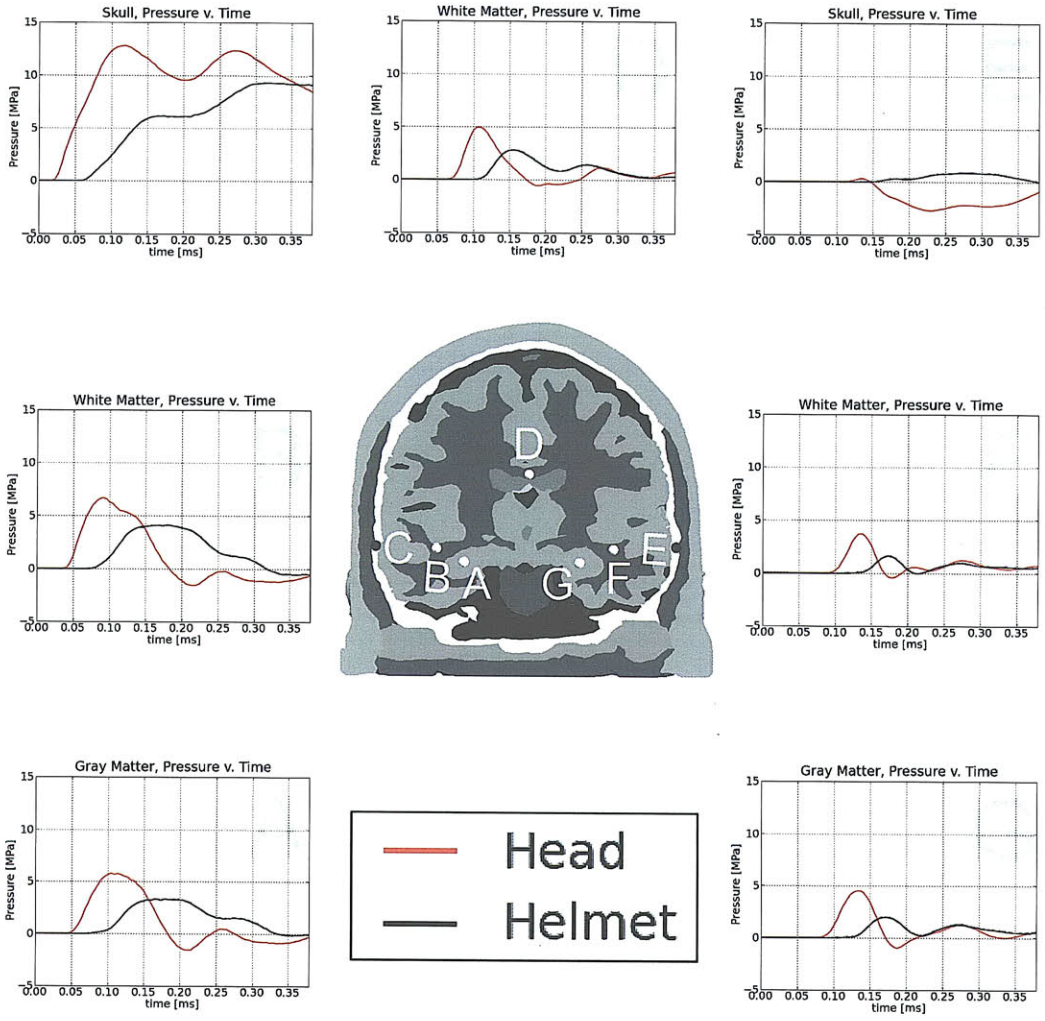

Figure 5-6: Pressure histories from the head and helmet 30 atm blast simulations at points in the mid-coronal plane. The scale is from -5 to 15 MPa.

peak pressure in the head simulation was 5.79 MPa and occurred at 0.105 ms, while the peak pressure in the helmet simulation was 3.3 MPa and occurred at 0.178 ms. Similarly, at point C in the skull on the left side of the head, the peak pressure in the head simulation was 12.78 MPa at 0.119 ms, while the peak pressure in the helmet simulation was 9.36 MPa at 0.315 ms. And at point F, located in the white matter on the right side of the cranial cavity, the peak pressure reached in the head simulation was 3.68 MPa at 0.137 ms, while the peak pressure reached in the helmet simulation was 1.64 MPa at 0.173 ms. Thus, from Fig. 5-6, we can see that the helmet does slightly aid in delaying and reducing the magnitude of pressure peaks experienced by points within the head.

We similarly extract and plot pressure histories for points located in the mid-sagittal plane. Fig. 5-7 compares the pressure histories from the head and helmet simulations for each of the six locations labeled as points A, B, C, D, E, and F in the figure. Points A and B are located in the frontal lobe, point C is in the corpus callosum, point D is in the parietal lobe, point E is in the occipital lobe, and point F is in the pons. Points A, B, D, and E are in the gray matter, while points C and F are in the white matter.

We again observe that at each point, the pressure peaks are delayed in time and reduced in magnitude in the helmet simulation compared to the head simulation. At point B in the frontal lobe, for example, the peak pressure reached 4.18 MPa at 0.109 ms in the head simulation, but only 2.41 MPa at 0.155 ms in the helmet simulation. Similarly, for point F in the brainstem, while the peak pressure reached 5.57 MPa at 0.123 ms in the head simulation, it only reached 2.45 MPa at 0.173 ms in the helmet simulation. These results suggest that at individual points in areas of the brain with critical functionality, the ACH is somewhat effective in delaying and reducing the magnitude of pressure peaks caused by blast waves.

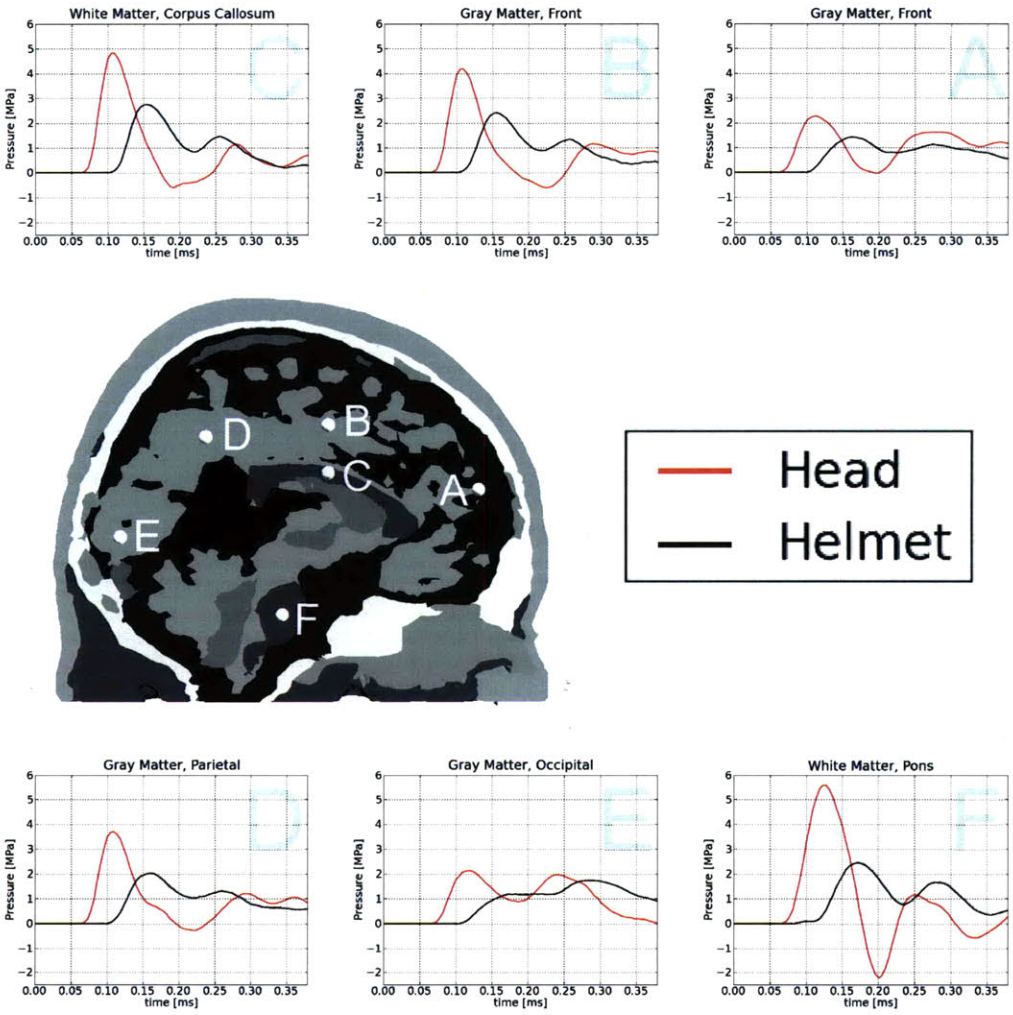

Figure 5-7: Pressure histories from the head and helmet 30 atm blast simulations at points in the mid-sagittal plane. The scale is from -2.5 to 6 MPa.

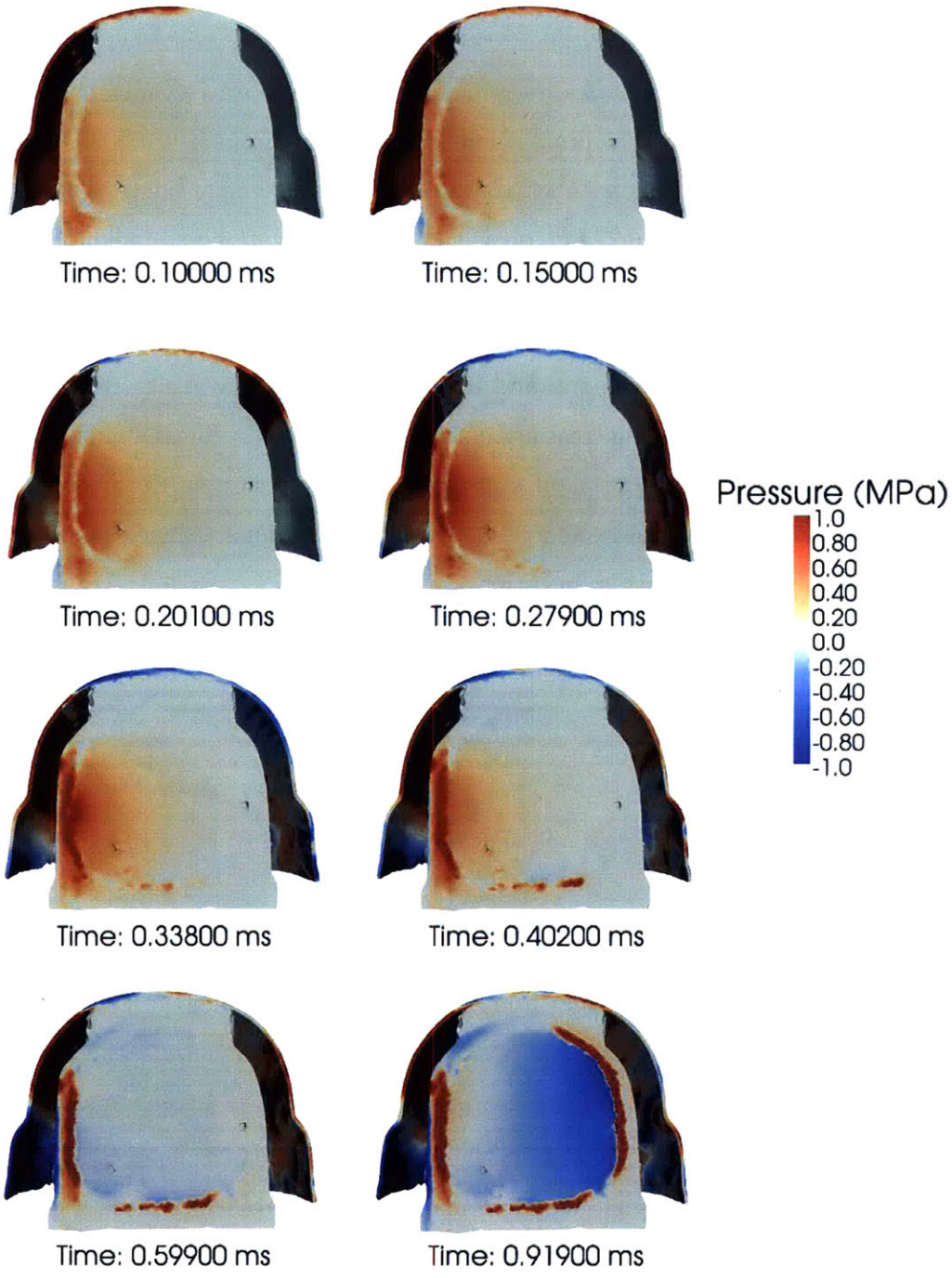

Figure 5-8: Snapshots of pressure from the helmet impact simulation. The scale for the color bar is from -1.0 to 1.0 MPa.

5.4 5 m/s Impact Simulation

The extended FHM was next subjected to a 5 m/s lateral impact with a stationary boundary. Fig. 5-8 illustrates the propagation of stress waves through mid-coronal sections of the head in the 5 m/s impact simulation. From t=0.100 ms, we can see stress waves propagating from left to right through the cranial cavity. The snapshots at t=0.150, 0.201, and 0.279 ms show the wave propagation and buildup of positive pressure in the left temporal region around the coup site, the site of impact. At t=0.338 and 0.402 ms, we observe the concentration of pressure in the skull and muscle along the left temporal and inferior surfaces of the skull. By t=0.599 and 0.919 ms, we can see the increasing concentration of positive pressure in the skull and muscle, as well as the growth of a negative pressure region on the right side of the cranial cavity, at the contrecoup site. As in the head impact simulation, we observe classic coup and contrecoup behavior.

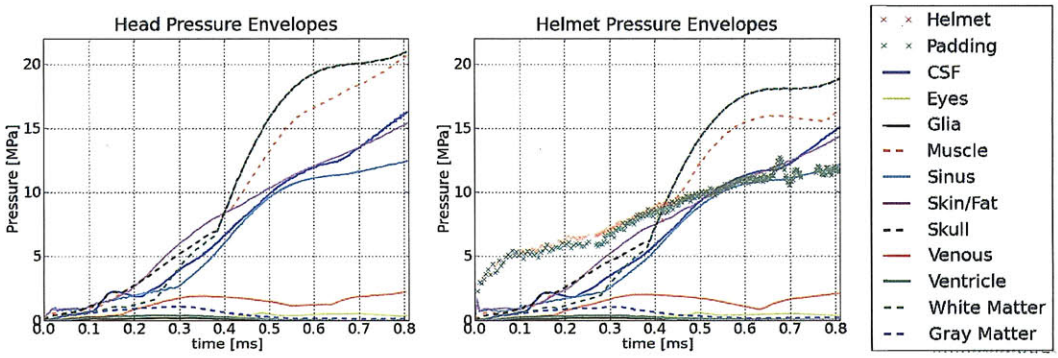

Figure 5-9: Pressure envelopes from the head and helmet impact simulations. The scale is from 0 to 22 MPa

Fig. 5-9 compares the pressure envelopes for the various head structures from the head and helmet impact simulations. From Fig. 5-9, we can again see that the helmet slightly reduces the magnitudes of the maximum pressures experienced. For example, the maximum pressure experienced by the skull and gray matter was reduced from 20.98 MPa in the head simulation to 18.79 MPa in the helmet simulation. Similarly, the maximum pressure experienced by the muscle was reduced from 20.66 MPa to 16.30 MPa, and the maximum pressure experienced by the CSF was reduced from

16.22 MPa to 14.97 MPa.

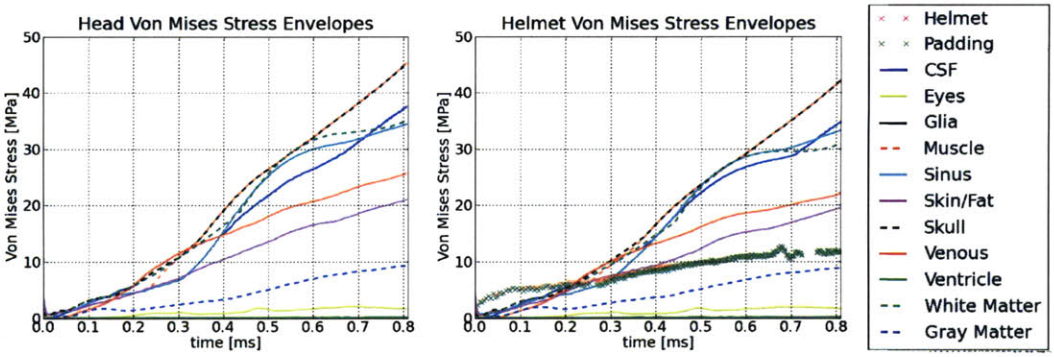

Figure 5-10: Von Mises stress envelopes from the head and helmet impact simulations. The scale is from 0 to 50 MPa.

Comparison of the Von Mises stress envelopes in Fig. 5-10 also demonstrates slight reductions in the maximum Von Mises stresses experienced. For example, the maximum Von Mises stress experienced by the skull reached a peak of 45.28 MPa in the head simulation, but only 41.9 MPa in the helmet simulation. Similarly, the maximum Von Mises stress experienced by the CSF reached a peak of 37.49 MPa in the head simulation, but only 34.57 MPa in the helmet simulation. Thus, we see that in an impact scenario the helmet can reduce the peak Von Mises stresses experienced by head structures to a small degree.

5.5 Discussion

The results presented in this chapter suggest that the ACH can slightly delay and reduce the pressures and shear stresses experienced by the human head following exposure to a blast wave or lateral impact. However, the benefits afforded by the helmet are minimal. In the blast scenario, the open design of the helmet slightly delays, but does not prevent, the arrival of the blast wave at the head. The helmet does protect the top of the head from direct exposure to the blast wave, but the advantage is minimal since the top of the head is not a major pathway of load transmission into the intracranial cavity. Since the ACH fails to protect major load transmission pathways, it does not significantly contribute to mitigating the stress waves transmitted to the

brain tissue. However, no deleterious wave-focusing effects, which have been reported by others, were observed either [59]. The results suggest that a more effective blast mitigation strategy would be to add a device, such as a face shield, that would more completely surround the head and protect it from direct exposure to blast waves.

Chapter 6

Conclusions

Blast-related TBI has gained prominence in recent years due to the conflicts in Iraq and Afghanistan, emerging as a leading injury among U.S. service members serving in Operation Iraqi Freedom and Operation Enduring Freedom. Despite the importance of understanding blast-related TBI, little is known about the mechanical effects of blasts on the human head; no injury thresholds have been established for blast effects on the head, and even direct transmission of the shock wave to the intracranial cavity has been disputed. Even less is known about how personal protective equipment such as the Advanced Combat Helmet (ACH) affect the brain's response to blasts.

In our effort to investigate the mechanical response of the head to blasts, we developed a sophisticated, biofidelic computational model from high-resolution medical imaging data. The model, known as the DVBIC/MIT Full Head Model (FHM), consisted of 11 distinct structures and was optimized for use in finite element simulations. The FHM was then used in blast simulations conducted in an extension of the Virtual Test Facility (VTF), a suite of computational solid and fluid dynamics solvers that allow for accurate simulation of fluid-structure interaction. In the VTF, the FHM was subjected to: (1) a blast with an incident overpressure of 6 atm, estimated by the standardized Bowen curves to be the threshold for unarmored blast lung injury; (2) a blast with an incident overpressure of 30 atm, estimated by the Bowen curves to result in 99% lethality due to unarmored blast lung injury; and (3) a 5 m/s lateral impact [9]. Snapshots from the blast simulations illustrate the propagation of the blast wave

through the skull and into the intracranial cavity, where the transmitted and reflected waves interact to generate complex pressure fields. Plots of the pressure envelopes for each of the 11 distinct structures show the disparate, heterogeneous responses of the head structures to the blast wave and highlight the importance of the geometry of the head in producing nonuniform pressure fields that affect each structure in distinct ways. The snapshots and pressure envelopes from the blast simulations also demonstrate that reflection of stress waves results in magnification of pressure, with peak pressures reaching up to 13-15 times the incident overpressure. Results from the blast simulations were then compared with results from the impact simulation, which had resulted in the expected coup-contrecoup behavior. When pressure envelopes from the blast and impact simulations were compared, it was observed that the peak pressures experienced in the 30 atm blast simulation were significantly higher than the peak pressures experienced in the impact simulation. When pressure histories from the blast and impact simulations were compared at points in the mid-coronal and mid-sagittal planes, it became even more clear that pressures from the blast simulations could exceed those from the impact simulation; pressures from even the 6 atm blast simulation were higher than pressures from the impact simulation at a number of critical locations, including the corpus callosum and brainstem. These results from the blast and impact simulations suggest that blasts can penetrate the cranial cavity and plausibly cause traumatic brain injury.

Subsequent investigation of the effect of the ACH on the blast response of the head found that the ACH provided minimal mitigation of blast effects. The ACH and padding in the standard configuration were added to the DVBIC/MIT FHM to create an extended FHM, and the extended FHM was subjected to a 30 atm blast and a 5 m/s lateral impact. Snapshots of pressure from the 30 atm helmet simulation show the blast wave penetrating the cranial cavity; the helmet slightly delayed, but did not prevent, direct transmission of stresses from the blast wave to the left temporal region of the head. Comparison of pressure envelopes and pressure histories from the head and helmet 30 atm blast simulations shows that the ACH reduced peak pressure magnitudes and delayed peak pressure arrival times to a small degree and had an

ambiguous effect on shear stress response. No deleterious wave-focusing effects were observed. The results suggest that the ACH provided only minimal protection against blasts because it failed to block major pathways of load transmission from the blast to the brain. A more effective blast mitigation strategy might be to alter the design of the helmet or add a device to more completely surround the head and protect it from direct exposure to blast waves.

6.1 Future Work

The simulations described in this thesis represent a preliminary effort to model blast-related TBI. The use of a detailed, biofidelic human head model with sophisticated CFD and CSD solvers is a significant improvement over existing computational studies in the literature, but a number of additional steps could be taken to further enhance our model. First, additional work is needed to improve the material models. In particular, our model could be substantially improved by incorporating advanced tissue constitutive models based on experimental results and material models that capture the anisotropy of white matter. In addition, a constitutive model that captures the inelastic response of the foam padding would allow us to better examine the effects of the ACH on the blast response of the head. Second, it would be advantageous to improve the material properties used in the simulations by using properties obtained from high strain rate dynamic testing of mammalian brain tissue. The material properties used in the current simulations were obtained from the literature, and they were often originally obtained from decades-old, low strain rate experiments. Third, we could build confidence in our model by conducting validation studies; while experimental intracranial stress data for humans exposed to blasts are not available, we could validate simulations against lab-scale and field blast tests for animal and physical surrogate models. By incorporating these improvements, we could obtain a significantly more accurate computational model of the human head. We then could further enhance our understanding of blast-related TBI by subjecting the model to blasts of different intensities and directions and could investigate alternative designs

for protective equipment. Much work remains to more fully understand blast-related TBI and develop prevention and mitigation strategies; this thesis represents simply a first step in that endeavor.

Bibliography

[1] D.V. Agoston, A. Gyorgy, O. Eidelman, and H.B. Pollard. Proteomic biomarkers for blast neurotrauma: targeting cerebral edema, inflammation, and neuronal death cascades. *Journal of Neurotrauma*, 26:901–911, 2009.

[2] M.P. Alexander. Mild traumatic brain injury: Pathophysiology, natural history, and clinical management. *Neurology*, 45:1253–1260, 1995.

[3] R.J. Anderson. Shell shock: An old injury with new weapons. *Molecular Interventions*, 8(5):204–218, 2008.

[4] K.B. Arbogast and S.S. Margulies. Material characterization of the brainstem from oscillatory shear tests. *Journal of Biomechanics*, 31:801–807, 1998.

[5] Srikanti Rupa Avasarala. Blast overpressure relief using air vacated buffer medium. Master's thesis, Massachusetts institute of Technology, 2009.

[6] W. E. Baker. *Explosions In Air.* University of Texas Press, Texas, 1973.

[7] K. Beauchamp, H. Mutlak, W.R. Smith, E. Shohami, and P.F. Stahel. Pharmacology of traumatic brain injury: Where is the "golden bullet"? *Molecular Medicine*, 14(11-12):731–740, 2008.

[8] G. Belingardi, G. Chiandussi, and I. Gaviglio. Development and validation of a new finite element model of human head. In *Proceedings of the 19th International Technical Conference on the Enhanced Safety of Vehicles*, 2005.

[9] I. Bowen, E.R. Fletcher, D.R. Richmond, F.G. Hirsch, and C.S. White. Biophysical mechanisms and scaling procedures applicable in assessing responses of the thorax energized by air-blast overpressures or by nonpenetrating missiles. *Ann. N.Y. Acad. Sci*, 152:122–146, 1968.

[10] D.W.A. Brands, G.W.M. Peters, and P.H.M. Bovendeerd. Design and numerical implementation of a 3-d non-linear viscoelastic constitutive model for brain tissue during impact. *Journal of Biomechanics*, 37(1):127–134, 2004.

[11] Centers for Disease Control and Prevention. *Explosions and Blast Injuries: A Primer for Clinicians.* CDC, Atlanta, GA, 2003.

[12] I. Cernak, J. Savic, Z. Malicevic, G. Zunic, P. Radosevic, I. Ivanovic, and L. Davidovic. Involvement of the central nervous system in the general response to pulmonary blast injury. *The Journal of Trauma: Injury, Infection, and Critical Care*, 40(3S):100S–104S, 1996.

[13] M.S. Chafi, G. Karami, and M. Ziejewski. Biomechanical assessment of brain dynamic responses due to blast pressure waves. *Annals of Biomedical Engineering*, 38(2):490–504, 2010.

[14] M.E. Clark, M.J. Bair, C.C. Buckenmaier, R.J. Gironda, and R.L. Walker. Pain and combat injuries in soldiers returning from operations enduring freedom and iraqi freedom: Implications for research and practice. *Journal of Rehabilitation Research and Development*, 44(2):179–194, 2007.

[15] B. Coats and S.S. Margulies. Material properties of porcine parietal cortex. *Journal of Biomechanics*, 39(13):2521–2525, 2006.

[16] B. Corner. A cad model of the advanced combat helmet. Personal Communication, 2008.

[17] A.C. Courtney and M.W. Courtney. A thoracic mechanism of mild traumatic brain injury due to blast pressure waves. *Medical Hypotheses*, 72:76–83, 2009.

[18] A. Cuitiño and M. Ortiz. A material-independent method for extending stress update algorithms from small-strain plasticity to finite plasticity with multiplicative kinematics. *Eng. Comput.*, 9:437–451, 1992.

[19] J. Cummings, M. Aivazis, R. Samtaney, R. Radovitzky, S. Mauch, and D. Meiron. A virtual test facility for the simulation of dynamic response in materials. *Journal of Supercomputing*, 23:39–50, 2002.

[20] R. Deiterding, R. Radovitzky, S.P. Mauch, L. Noels, J.C. Cummings, and D. Meiron. A virtual test facility for the efficient simulation of solid material response under strong shock and detonation wave loading. *Engineering with Computers*, 22:325–347, 2006.

[21] A.M. Dennis and P.M. Kochanek. Pathobiology of blast injury. In *Intensive Care Medicine*, pages 1011–1022. Springer Berlin Heidelberg, 2007.

[22] C.S. Drapaca, G. Tenti, K. Rohlf, and S. Sivaloganathan. A quasi-linear viscoelastic constitutive equation for the brain: Application to hydrocephalus. *Journal of Elasticity*, 85(1):65–83, 2006.

[23] D.S. Drumheller. *Introduction to wave propagation in nonlinear fluids and solids.* Cambridge University Press, 1998.

[24] T. El Sayed, A. Mota, F. Fraternali, and M. Ortiz. Biomechanics of traumatic brain injury. *Comput. Methods Appl. Mech. Engrg.*, 197:4692–4701, 2008.

[25] N.M. Elsayed. Toxicology of blast overpressure. *Toxicology*, 121:1–15, 1997.

[26] A.I. Faden, P. Demediuk, S.S. Panter, and R. Vink. The role of excitatory amino acids and nmda receptors in traumatic brain injury. *Science*, 244(4906):798–800, 1989.

[27] M.R. Galarneau, S.I. Woodruff, J.I. Dye, C.R. Mohrle, and A.L. Wade. Traumatic brain injury during Operation Iraqi Freedom: findings from the United States Navy-Marine Corps combat trauma registry. *Journal of Neurosurgery*, 108:950–957, 2008.

[28] A. Gawande. Casualties of war - military care for the wounded from iraq and afghanistan. *New England Journal of Medicine*, 351:2471–2475, 2004.

[29] A. Gefen and S.S. Margulies. Are in vivo and in situ brain tissues mechanically similar? *Journal of Biomechanics*, 37(4):1339–1352, 2004.

[30] M.D. Gilchrist, D. O'Donoghue, and T.J. Horgan. A two-dimensional analysis of the biomechanics of frontal and occipital head impact injuries. *International Journal of Crashworthiness*, 6(2):253–262, 2001.

[31] S.W. Gong, H.P. Lee, and C. Lu. Computational simulation of the human head response to non-contact impact. *Computers and Structures*, 86:758–770, 2008.

[32] M.H. Heitger, R.D. Jones, A.D. Macleod, D.L. Snell, C.M. Frampton, and T.J. Anderson. Impaired eye movements in post-concussion syndrome indicate suboptimal brain function beyond the influence of depression, malingering or intellectual ability. *Brain*, 132(10):2850–2870, 2009.

[33] J. Ho and S. Kleiven. Dynamic response of the brain with vasculature: A three-dimensional computational study. *Journal of Biomechanics*, 40:3006–3012, 2007.

[34] C. W. Hoge, D. McGurk, J. L. Thomas, A. L. Cox, C. C. Engel, and C. A. Castro. Mild traumatic brain injury in u.s. soldiers returning from iraq. *New England Journal of Medicine*, 358:453–463, 2008.

[35] G.A. Holzapfel. *Nonlinear Solid Mechanics: A Continuum Approach for Engineering.* John Wiley & Sons Ltd., 2001.

[36] T.J. Horgan and M.D. Gilchrist. The creation of three-dimensional finite element models for simulating head impact biomechanics. *International Journal of Crashworthiness*, 8(4):353–366, 2003.

[37] T.J. Horgan and M.D. Gilchrist. Influence of fe model variability in predicting brain motion and intracranial pressure changes in head impact simulations. *International Journal of Crashworthiness*, 9(4):401–418, 2004.

[38] H.S. Kang, R. Willinger, B.M. Diaw, and B. Chinn. Validation of a 3d anatomic human head model and replication of head impact in motorcycle accident by finite element modeling. *Stapp Car Crash Conference Proceedings*, 41:329–338, 1997.

[39] K. Kato, M. Fujimura, A. Nakagawa, A. Saito, T. Ohki, K. Takayama, and T. Tominaga. Pressure-dependent effect of shock waves on rat brain: induction of neuronal apoptosis mediated by a caspase-dependent pathway. *Journal of Neurosurgery*, 106:667–676, 2007.

[40] J.E. Kennedy, M.S. Jaffee, G.A. Leskin, J.W. Stokes, F.O. Leal, and P.J. Fitzpatric. Posttraumatic stress disorder and posttraumatic stress disorder-like symptoms and mild traumatic brain injury. *Journal of Rehabilitation Research and Development*, 44(7):895–920, 2007.

[41] S. Kleiven and W.N. Hardy. Correlation of an fe model of the human head with local brain motion – consequences for injury prediction. *Stapp Car Crash Journal*, 46:123–144, 2002.

[42] S. Kleiven and H. von Holst. Consequences of head size following trauma to the human head. *Journal of Biomechanics*, 35:153–160, 2002.

[43] M. Kojic, S. Mijailovic, and N. Zdravkovic. Modelling of muscle behavior by the finite element method using hill's three-element model. *International Journal for Numerical Methods in Engineering*, 43:941–953, 1998.

[44] M.F. Kraus, T. Susmaras, B.P. Caughlin, C.J. Walker, J.A. Sweeney, and D.M. Little. White matter integrity and cognition in chronic traumatic brain injury: a diffusion tensor imaging study. *Brain*, 130:2508–2519, 2007.

[45] J.A. Langlois, W. Rutland-Brown, and K.E Thomas. *Traumatic brain injury in the United States: Emergency department visits, hospitalizations, and deaths.* Centers for Disease Control and Prevention, National Center for Injury Protection, Atlanta,GA, 2006.

[46] M.C. LaPlaca, D.K. Cullen, J.J. McLoughlin, and R.S. Cargill. High rate shear strain of three-dimensional neural cell cultures: A new in vitro traumatic brain injury model. *Journal of Biomechanics*, 38(5):1093–1105, 2005.

[47] L.Y. Leung, P.J. VandeVord, A.L. Dal Cegnio, C. Bir, K.H. Yang, and A.I. King. Blast related neurotrauma: A review of cellular injury. *Molecular and cellular biomechanics*, 5(3):155–168, 2008.

[48] A. Lew, R. Radovitzky, and M. Ortiz. An artificial-viscosity method for the lagrangian analysis of shocks in solids with strength on unstructured, arbitrary-order tetrahedral meshes. *Journal of Computer-Aided Materials Design*, 8:213–231, 2001.

[49] G. Ling, F. Bandak, R. Armonda, G. Grant, and J. Ecklund. Explosive blast neurotrauma. *Journal of Neurotrauma*, 28:815–825, 2009.

[50] J.B. Long, T.L. Bentley, K.A. Wessner, C. Cerone, S. Sweeney, and R.A. Bauman. Blast overpressure in rats: recreating a battlefield injury in the laboratory. *Journal of Neurotrauma*, 26:827–840, 2009.

[51] L.E Malvern. *Introduction to the mechanics of a continuous medium.* Prentice-Hall, Englewood Cliffs, N.J., 1969.

[52] M.A. Meyers. *Dynamic behavior of materials.* Wiley Interscience, 1994.

[53] Mild Traumatic Brain Injury Committee of the Head Injury Interdisciplinary Special Interest Group of the American Congress of Rehabilitation Medicine. The definition of traumatic brain injury. *Journal of Head Trauma and Rehabilitation*, 8(3):86–87, 1993.

[54] K. Miller. Constitutive model of brain tissue suitable for finite element analysis of surgical procedures. *Journal of Biomechanics*, 32(5):531–537, 1999.

[55] K. Miller. Method of testing very soft biological tissues in compression. *Journal of Biomechanics*, 38(1):153–158, 2005.

[56] K. Miller and K. Chinzei. Mechanical properties of brain tissue in tension. *Journal of Biomechanics*, 35(4):483–490, 2002.

[57] S.M. Moochhala, S. Md, J. Lu, C.-H. Teng, and C. Greengrass. Neuroprotective role of aminoguanidine in behavioral changes after blast injury. *The Journal of Trauma: Injury, Infection, and Critical Care*, 56(2):393–403, 2004.

[58] B. Morrison, H.L. Cater, C.D. Benham, and L.E. Sundstrom. An in vitro model of traumatic brain injury utilising two-dimensional stretch of organotypic hippocampal slice cultures. *Journal of Neuroscience Methods*, 150(2):192–201, 2006.

[59] W.C. Moss, M.J. King, and E.G. Blackman. Skull flexure from blast waves: A mechanism for brain injury with implications for helmet designs. *The Journal of the Acoustical Society of America*, 125(4):2650–2667, 2009.

[60] C.K. Murray, J.C. Reynolds, J.M. Schroeder, M.B. Harrison, O.M. Evans, and D.R. Hospenthal. Spectrum of care provided at an echelon ii medical unit during operation iraqi freedom. *Military Medicine*, 170:516, 2005.

[61] A.M. Nahum, R. Smith, and C.C. Ward. Intracranial pressure dynamics during head impact. *Stapp Car Crash Conference*, 221:339–366, 1977.

[62] D.E. Nampiaparampil. Prevalence of chronic pain after traumatic brain injury: A systematic review. *Journal of the American Medical Association*, 300(6):711–719, 2009.

[63] S.J. Neuhaus, P.F. Sharwood, and J.V. Rosenfeld. Terrorism and blast explosions: lessons for the Australian surgical community. *ANZ Journal of Surgery*, 76:637–644, 2006.

[64] T. Nishimoto and S. Murakami. Relation between diffuse axonal injury and internal head structures on blunt impact. *Journal of Biomechanical Engineering – Transactions of the ASME*, 120(1):140–147, 1998.

[65] "U.S. Government Accountability Office". Mild traumatic brain injury screening and evaluation implemented for oef/oif veterans, but challenges remain, 2008.

[66] D.E. Okhotsimskii, I.A. Kondrasheva, Z.P. Vlasova, and R.K. Kozakova. Calculation of a point explosion taking into account counter pressure. *Tr. Mat. Inst. Steklova*, 50:1–65, 1957.

[67] S. Okie. Traumatic brain injury in the war zone. *New England Journal of Medicine*, 352(20):2043–2047, 2005.

[68] M. Ortiz and L. Stainier. The variational formulation of viscoplastic updates. *Computer Methods in Applied Mechanics and Engineering*, 171:419–444, 1999.

[69] E. Park, J.D. Bell, and A.J. Baker. Traumatic brain injury: Can the consequences be stopped? *Canadian Medical Association Journal*, 178(9):1163–1170, 2008.

[70] J.T. Povlishock and D.I. Katz. Update of neuropathology and neurological recovery after traumatic brain injury. *Journal of Head Trauma Rehabilitation*, 20(1):76–94, 2005.

[71] M.T. Prange and S.S. Margulies. Regional, directional, and age-dependent properties of the brain undergoing large deformation. *Journal of Biomechanical Engineering – Transactions of the ASME*, 124(2):244–252, 2002.

[72] V. Rao and C. Lyketsos. Neuropsychiatric sequelae of traumatic brain injury. *Psychosomatics*, 45:95–103, 2000.

[73] J.-S. Raul, D. Baumgartner, R. Willinger, and B. Ludes. Finite element modelling of human head injuries caused by a fall. *International Journal of Legal Medicine*, 120(4):212–218, 2006.

[74] J.S. Ruan, T. Khalil, and A.I. King. Dynamic response of the human head to impact by three-dimensional finite element analysis. *Journal of Biomechanical Engineering*, 116(1):44–50, 1994.

[75] R.L. Ruff, S.S. Ruff, and X.-F. Wang. Headaches among Operation Iraqi Freedom / Operation Enduring Freedom veterans with mild traumatic brain injury associated with exposures to explosions. *Journal of Rehabilitation Research and Development*, 45(7):941–952, 2008.

[76] K.E. Saatman, A.-C. Duhaime, R. Bullock, A.I.R. Maas, A. Valadka, and G.T. Manley. Classification of traumatic brain injury for targeted therapies. *Journal of Neurotrauma*, 25:719–738, 2008.

[77] A.I. Schneiderman, E.R. Braver, and H.K. Kang. Understanding sequelae of injury mechanisms and mild traumatic brain injury incurred during the conflicts in Iraq and Afghanistan: Persistent postconcussive symptoms and posttraumatic stress disorder. *American Journal of Epidemiology*, 167(12):1446–1452, 2008.

[78] F. Shen, T.E. Tay, J.Z. Li, S. Nigen, P.V.S. Lee, and H.K. Chan. Modified bilston nonlinear viscoelastic model for finite element head injury studies. *Journal of Biomechanical Engineering – Transactions of the ASME*, 128(5):797–801, 2006.

[79] L.Z. Shuck and S.H. Advani. Rheological Response of Human Brain Tissue in Shear. *Journal of Basic Engineering*, pages 905–911, 1972.

[80] A. Suneson, H. Axelsson, H. Hjelmqvist, A. Medin, and J.K.E. Persson. Physiological changes in pigs exposed to a blast wave from a detonating high-explosive charge. *Military Medicine*, 165(2):119–126, 2000.

[81] S.I. Svetlov, S.F. Larner, D.R. Kirk, J. Atkinson, R.L. Hayes, and K.K.W. Wang. Biomarkers of blast-induced neurotrauma profiling molecular and cellular mechanisms of blast brain injury. *Journal of Neurotrauma*, 26:913–921, 2009.

[82] K.H. Taber, D.L. Warden, and R.A. Hurley. Blast-related traumatic brain injury: What is known? *Journal of Neuropsychiatry and Clinical Neuroscience*, 18:141–145, 2006.

[83] E.G. Takhounts and R.H. Eppinger. On the development of the SIMon finite element head model. *Stapp Car Crash Journal*, 47:107–133, 2003.

[84] T. Tanielian. *Invisible Wounds of War: Psychological and Cognitive Injuries, Their Consequences, and Services to Assist Recovery.* RAND Corporation, Center for Military Health Policy Research, Santa Monica, CA, 2008.

[85] P.A. Taylor and C.C. Ford. Simulation of blast-induced early-time intracranial wave physics leading to traumatic brain injury. *Journal of Biomechanical Engineering*, 131(6):061007, 2009.

[86] H. Terrio, L.A. Brenner, B.J. Ivins, J.M. Cho, K. Helmick, K. Schwab, K. Scally, R. Bretthauer, and D. Warden. Traumatic brain injury screening: preliminary findings in a u.s. army brigade combat team. *Journal of Head Trauma Rehabilitation*, 24:14–23, 2009.

[87] P. Thompson. *Compressible-Fluid Dynamics.* McGraw-Hill, New York, 1972.

[88] D.J. Thurman, C. Alverson, K.A. Dunn, J. Guerrero, and J. Sniezek. Traumatic brain injury in the United States: A public health perspective. *Journal of Head Trauma Rehabilitation*, 14(6):602–615, 1999.

[89] D.J. Thurman, J.E. Sniezek, and D. Johnson. *Guidelines for Surveillance of Central Nerous System Injury.* Centers for Disease Control and Prevention, Atlanta, 1995.

[90] X. Trosseille, C. Tarriere, F. Lavaste, F. Guillon, and A. Domont. Development of a f.e.m. of the human head according to a specific test protocol. *Stapp Car Crash Conference Proceedings*, 36:235–253, 1992.

[91] T. Veenith, S.S.H. Goon, and R.M. Burnstein. Molecular mechanisms of traumatic brain injury: the missing link in management. *World Journal of Emergency Surgery*, 4(7), 2009.

[92] F. Velardi, F. Fraternali, and M. Angelillo. Anisotropic constitutive equations and experimental tensile behavior. *Biomechanics and Modeling in Mechanobiology*, 5(1):1617–7959, 2006.

[93] K.K.W Wang. *Calpain and caspase in ischemic and traumatic brain injury*, pages 181–200. CRC press, 2002.

[94] D. Warden. Military tbi during the iraq and afghanistan wars. *Journal of Head Trauma Rehabilitation*, 21:398–402, 2006.

[95] D.L. Warden, L.M Ryan, K. Schwab, L. French, W. Lu, W. Lux, G. Ling, and J. Ecklund. War neurotrauma: the defense and veterans brain injury center(dvbic) experience at walter reed army medical center (wramc). *Journal of Neurotrauma*, 22:1178, 2005.

[96] C. Werner and K. Engelhard. Pathophysiology of traumatic brain injury. *British Journal of Anaesthesia*, 99(1):4–9, 2007.

[97] R. Willinger and D. Baumgartner. Human head tolerance limits to specific injury mechanisms. *International Journal of Crashworthiness*, 8(6):605–617, 2003.

[98] R. Willinger, D. Baumgartner, B. Chinn, and E. Schuller. New dummy head prototype: Development, validation and injury criteria. *International Journal of Crashworthiness*, 6(3):281–293, 2001.

[99] R. Willinger, B.M. Diaw, D. Baumgartner, and B. Chinn. Full face protective helmet modelling and coupling with a human head model. *International Journal of Crashworthiness*, 7(2):167–178, 2002.

[100] R. Willinger, H. Kang, and B. Diaw. Three-dimensional human head finite-element model validation against two experimental impacts. *Annals of Biomedical Engineering*, 27:403–410, 1999.

[101] Y. Xiong, A. Mahmood, and M. Chopp. Emerging treatments for traumatic brain injury. *Expert Opinion on Emerging Drugs*, 14(1):67–84, 2009.

[102] Y.B. Zel'dovich and Y.P. Raizer. *Physics of shock waves and high-temperature hydrodynamic phenomena*, volume 2. Academic press, New York and London, 1967.

[103] L. Zhang, K.H. Yang, R. Dwarampudi, K. Omori, T. Li, K. Chang, W. Hardy, T. Khalil, and A.I. King. Recent advances in brain injury research. *Stapp Car Crash Journal*, 45:369–394, 2001.

[104] L. Zhang, K.H. Yang, and A.I. King. Comparison of brain responses between frontal and lateral impact by finite element modeling. *Journal of Neurotrauma*, 18:21–30, 2001.

[105] L. Zhang, K.H. Yang, and A.I. King. A proposed injury threshold for mild traumatic brain injury. *Journal of Biomechanical Engineering - Transactions of the ASME*, 126(2):226–236, 2004.